Politecnico di Torino

Politecnico di Torino

Master's degree in Quantum Engineering

A.a. 2024/2025

Graduation Session December 2025

Design, fabrication and characterization of ultrathin superconducting Aluminum lumped element resonators for spin ensemble quantum memories application

Supervisors:

Prof. Matteo Cocuzza

Dr. Emanuele Enrico

Candidate:

Riccardo Ghianni

A Sebastiano

In fondo è solo un trucco. Sì, è solo un trucco.
Jep Gambardella

Abstract

The realization of a fault-tolerant quantum computer remains one of the most significant challenges in modern physics and computer science. The physical qubits used in the Quantum Processing Units (QPUs) should be at the same time strongly coupled to controls while being well isolated from environmental noise. Hybrid systems, combining different quantum technologies, represent a promising approach to overcome the limitations of individual platforms. By performing different tasks on the most suitable physical systems, hybrid architectures can enhance the overall performance of quantum devices, with applications ranging from quantum computing to communication.

In this thesis, we explore the potential of superconducting circuits as a versatile platform to implement spin ensemble quantum memories. These devices show the potential to be used to store quantum information for long times, while being easily integrated with superconducting qubits and resonators.

This work is mainly focused on superconducting lumped element resonators: their design with methodologies for a more efficient development process, the fabrication procedure performed in the PiQueT cleanroom, and characterization methodologies inside a dilution refrigerator. Moreover, the use of ultrathin Aluminum films is investigated as a high critical field superconductor, as an alternative to Niobium-based alloys.

Results on simulation success, two-level systems (TLS) loss mechanisms and kinetic inductance impact are reported, and performance of the Aluminum devices are compared to their copies in Niobium.

With further spin resonance experiments, device compatibility with Aluminum-based qubit platforms can be assessed and the development cycle of a fully operational quantum memory can be closed.

Table of Contents

Chapter 1

Introduction

1.1 Quantum Memories

The final application of this thesis work are quantum memories. In this section the main research framework of this topic is illustrated, with particular attention to their requirements and motivation of their development.

1.1.1 Quantum information

Quantum information science(QIS) [1] is an emerging research field, it studies the possibility of representing information by means of properties of quantum mechanics. This approach includes the study of abstract representation of the information by means of the so-called qubits, as alternative of classical bits, and the possible interactions with and between them. From a technological perspective this abstraction can be reached by means of quantum hardware: devices which contain a physical quantum system and provide the possibility to interact with it in a efficient and reliable manner.

The classical bit represents a number as 1 or 0, this quantity is measured in the physical implementation as the result of a classical measurement such as a voltage or the presence or not of a sensible amount of photons traveling in an optical fiber. The quantum bits are, instead, mathematically represented in a two-dimensional Hilbert space, with basis states commonly denoted as $|0\rangle$ and $|1\rangle$, in this way the quantum information present inside the qubit is represented by a superposition of the basis states $|\psi\rangle = \alpha\,|0\rangle + \beta\,|1\rangle$, it is important to note that here α and β are complex quantities, this takes into account for an imaginary part of the overall information which is proper of quantum systems. Here, the hardware is based on the use of a two level system commonly found in atoms, ions, or electrons tunnelling

between electric potential islands.

Quantum information takes into account all the relevant properties of a quantum system: superposition and entanglement. For this reason quantum technologies applied to computing and communication have very different working principles with respect to their classical counterparts, they are studied for their potentially disruptive application on several open problems.

One of the most studied topic of QIS is error detection and correction applied to quantum information. Quantum systems, in fact, are inherently very fragile, it is very difficult to get rid of noise sources and interactions with environment. Even though this devices work in very controlled and low temperature environments, the problem of building an effective fault-tolerant quantum computer (or quantum channel) is still open. The amount of reliability of a quantum system or device is quantified by several parameters defined in QIS, they are strictly related to physical phenomenons and defined by their experimental characterization. Heresome of these properties are listed.

Coherence times T_1 and T_2

Quantum systems tends to lose coherence due to their interaction with other two level systems (TLS) or the external environment. In particular two different parameters represent the coherence of a device, as stated previously quantum information is not only encoded in the amplitude of the states in the superposition but also in their phase. So, the these time parameters take into account the decoherence on both degrees of freedom. T_1 is called relaxation time, it refers to the tendency of the quantum systems to relax to the least energy eigenstate, usually labeled as $|0\rangle$. The time evolution of states amplitudes is modeled as an exponential decay: if we take a generic state $|\psi\rangle = \alpha\,|0\rangle + \beta\,|1\rangle$, due to relaxation phenomenon their amplitude is time dependant, β is then substituted by an exponential function which is decaying with a characteristic time T_1:

$$\beta(t) = \beta(0)e^{-\frac{t}{T_1}} \tag{1.1}$$

T_2 is instead measuring the characteristic time of phase coherence, which is modeled similarly to the relaxation phenomenon with an exponential decaying function.

Gate fidelity

Interaction with qubits is performed through gates, which change the amplitude and phase of the qubit. For example the X gate switches the coefficients, given $|\psi\rangle = \alpha |0\rangle + \beta |1\rangle$:

$$X |\psi\rangle = \beta |0\rangle + \alpha |1\rangle \tag{1.2}$$

Due different phenomena, it happens that the gate applied transforms the state in a non-exact manner. This possible mismatch are described by the fidelity, which quantifies how much two states are similar. This concept can be applied to gates or to channels, in the case of gates the comparison is made between the expected state after gate application, say $|\Phi\rangle$, and the actual one $|\Psi\rangle$:

$$F = |\langle \Phi | \Psi \rangle|^2 \tag{1.3}$$

Fidelity can take values between 0 and 1, representing the probability of success of the gate.

Quantum channel fidelity

Quantum channels are an abstractions of a carrier of quantum information from a point to another in the space or time. This concept is needed mostly in quantum communications since, also here, these objects are not defect free and tend to transform the input state while it should be left untouched. The bit flip channel,for example, accounts for a probability p that the X gate is applied to the state while it is traveling through an identity channel, the channel is then represented by the gate $U_c = (1-p)I + pX$. The fidelity is calculated analogously to the gate case, between the input and output state of the channel.

Measurement fidelity

At the end of a computation or communication process, the state of qubits needs to be measured in order to extract useful information. Measurement fidelity describes how accurately the experimental apparatus can distinguish between the possible outcomes, for example between the logical states “0” and “1.” In practice, detectors are not perfect: noise, technical imperfections, and crosstalk between qubits can lead to incorrect readout results. If a qubit in state “0” is sometimes mistaken for “1,” or vice versa, then measurement fidelity is reduced.

1.1.2 Quantum memories principles

As quantum computing and communication has been developed, several classical devices have to be substituted by their quantum analog capable of dealing with

physical quantum information carrier.

Among them one of the most important is the quantum memory[2]. In classical computers, the memory corresponds to a device which is storing information to be probably used later, in this way the registers of the computational unit are occupied by information needed just at the moment of execution. So, the memory is required to overwrite and store information for a greater amount of time with respect to CPU registers, and should be able to release this information on-demand on the data-bus when it is needed for computation. In any case it is unnecessary that a memory is able to change the information it is containing. In summary, quantum memories have to work as an analog of their classical counterparts.

As stated in the previous chapter quantum information is very fragile, in classical memories in fact, although error correction techniques are generally applied, errors such as bit flipping are extremely rare, moreover in a capacitor based memory(e.g. RAM) information is stored as far as the devices receives electrical power, in solid state drives instead the information can remain unchanged without power for decades. In classical computers the amount of time a device can store an information is never a concern. But, when we come to quantum technologies instead, it becomes a dominant factor. This is much more important in quantum memories which, since they have to store information in a reliable manner, need a characteristic coherence time much higher with respect to other devices. For this reason the physical system studied for applications as quantum memories are very different with respect to the qubits' ones.

The following list states the relevant figures of merit of a quantum memory system:

- **Memory time τ:** it represents the time over which the quantum information remains faithfully stored inside the memory. This parameter is of fundamental importance, in fact a quantum system very resilient to decoherence must be chosen. For communications applications this parameter should range from hundreds of milliseconds to few seconds.
- **Fidelity:** the fidelity here refers to the same concept of channel fidelity explained before. The state retrieved from the memory should be equal to the input state of the memory.
- **Efficiency η:** refers to the success probability of retrieving an input state. In fact, it is not sure that the memory acquisition process is always successfull.
- **Wavelength λ:** each memory has a specific wavelength which must be compatible with the system in which they are inserted and the applications

for which they are used. For example in communications it is necessary to work in telecom wavelength.

- **Multimode capacity:** this represents a sort of dimension of the memory. If the amount of wavelengths a memory can receive is higher it can store several qubits.

1.1.3 Applications and requirements

Quantum memories have applications in the fields of quantum communications and quantum computing. Before diving in their hardware implementation, in this section it is explained why they can be used in these fields and what are the different requirements for the specific application.

Quantum communication

The main objective of quantum communications is to allow transfer of quantum information between agents in a larger distance [3]. The only feasible physical carrier of information is light, traveling through a fiber or in free space. Even though light is very resilient to decoherence, both transmission systems are prone to losses. Since the information is encoded using at most few decades of photons, the loss of some of them could lead to errors or to an unsuccessful transport. This factor limits the possibility of increasing the dimensions of the single links. In classical communication it is possible to use repeaters to fully restore the attenuated signal. It is demonstrated by quantum no-cloning theorem[1] that it is impossible to clone a qubit into a new one, this forbids the possibility of engineering a quantum repeater with the same working principle of its classical analog. The main idea behind quantum repeaters is the concept of quantum teleportation[4]: it is possible to transfer information using an entangled pair of qubits, without directly sending a qubit through the fiber, in this scheme, Alice will perform transformation on her entangled qubit and the "message" qubit, then they will measure their qubits and by sharing informations on the measurements, Bob can retrieve the "message" qubit by applying a predefined set of gates. It must be noted that it is not possible to "build" an entangled pair of distant qubits, so, this solution is not eliminating the problem of transmission losses, since the qubits will have to be produced by an entanglement source and distributed to the peers. But, at least, the qubits will have to travel half the distance with respect to the simple sent-received protocol. It is also showed that it is possible to combine multiple repeaters and multiple layers of entangled pairs to repeat the very same quantum teleportation protocol. This allows for an even larger extension of the single link, using entanglement sources repeaters.

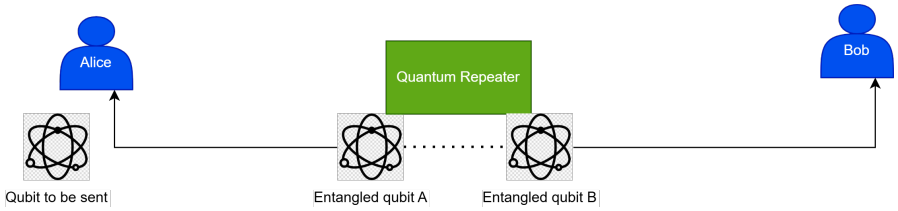

Figure 1.1: Quantum repeater scheme: entangled pairs are generated by sources and distributed to the peers, then quantum teleportation is used to transfer the information from Alice to Bob.

In this scenario, quantum memories are needed to store the entangled qubits until the teleportation protocol is completed [5]. In fact, since the entanglement sources are probabilistic, it is not sure that an entangled pair is available when needed. The memory will have to store the qubit until the other peer has received his half of the entangled pair. For this reason, in communications applications, the memory time τ must be at least comparable with the time needed for a signal to travel through the link. As an example, the velocity of the signal can be estimated as $5\mu s/km$, this means that for a 100km link, a memory time of at least $0.5ms$ is needed.

Another important characteristic of memories is trasduction. In fact, except for some new experimental approaches[6], it is unfeasible to store a single photon in a small space for too long. In this scenario the photon must interact with a solid state system capable of storing the information. This interaction is usually possible only if the photon wavelength matches the absorption spectrum of the solid state system. In communications applications, it is necessary to work in telecom wavelength (around $1550nm$) since this is the wavelength at which optical fibers have the lowest losses. For this reason, if the memory system does not work at this wavelength, a transducer is needed to convert the photon to a compatible wavelength before storage and then convert it back to telecom wavelength after retrieval. This process must be efficient and faithful, otherwise it will introduce losses and errors in the communication protocol.

Quantum computing

Quantum computing is another field of application of quantum memories. In this case, the memory is used to store intermediate results of a computation or to provide additional qubits for the computational unit.

During a computation, it is possible that some qubits are not needed for a certain amount of time, in this case they can be stored in the memory to free up space in

the computational unit. Moreover common trasmon qubits have coherence times in the order of some hundreds of microseconds, this is not enough to perform complex algorithms which require a large number of gates and qubits. Qubits stored in a quantum memory are less prone to decoherence with respect to superconductor qubits used in computation, due to different physical systems used in both solutions. This is especially useful in algorithms that require a large number of qubits and a large amount of time.

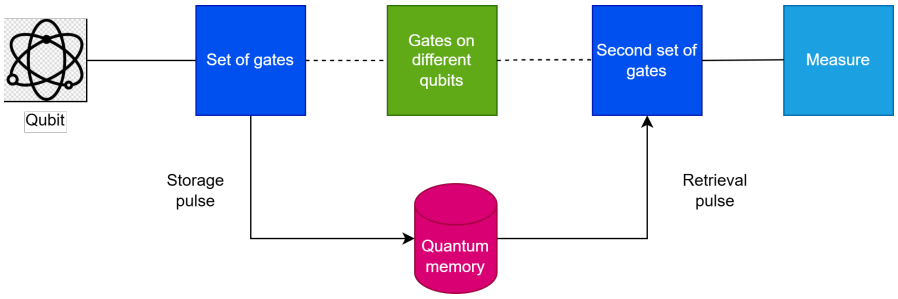

Figure 1.2: Implementation scheme of the QRAM protocol.

In this scenario, the requirements for the memory are different from those in communications. Since the memory is used to store intermediate results, the memory time τ, remains an important factor, it must be at least comparable with the time needed to perform a computation. Moreover, the efficiency η and fidelity becomes more and more important, if the transduction of the qubits is too much sensitive to errors, there is no advantage in storing the qubit in a memory to protect it from decoherence. For this reasons QRAMs [7] are not yet implemented in current quantum computers, since the state of the art of quantum memories is not enough advanced to provide a reliable service.

1.2 Different implementations

Keeping in mind the requirements stated in the previous section, several physical systems have been studied for applications as quantum memories. In this section a short overview of quantum memory implementations is provided [2], while in the next section a more detailed description of the specific implementation studied in this thesis is given.

In general the physical systems have to be very resilient to external environments, this feature has an higher impact with respect to the others. Such systems include:

- **Cold atomic gases:** these cold atoms are trapped in a magneto-optical trap. They are cooled down to microkelvin temperatures using laser cooling techniques, this allows to reduce the thermal motion of the atoms and increase their coherence time. The information is stored in the hyperfine levels of the atoms, which are very resilient to decoherence. The interaction between light and atoms is usually mediated by a strong control field, which allows to transfer the information from the light to the atoms and vice versa. These systems have shown very good performance in terms of memory time and fidelity, but they are not very practical for real-world applications due to their complexity and size.

- **Rare-earth doped crystals:** the ions have very narrow optical transitions, which allows for high-fidelity storage and retrieval of quantum states. The information is usually stored in the hyperfine levels of the ions, they are very resilient to decoherence. These systems have shown very good performance in terms of memory time and fidelity, but they require cryogenic temperatures to operate, which limits their practicality.

- **NV centers in diamond:** these types of solid state systems are used for very different applications, also at room temperature. The NV centers have very long coherence times at room temperature, which makes them very attractive for quantum memory applications. The information is usually stored in the spin states of the NV centers, which can be manipulated using microwave and optical fields. These systems have shown good performance in terms of memory time and fidelity, but they are still limited by the efficiency of the light-matter interaction.

- **Spin ensembles in semiconductors:** the main topic of this thesis, largely explained in the next section.

1.3 Spin ensemble quantum memories

Superconducting quantum devices are one of the most promising platforms for quantum computing [8], they have shown great potential in terms of scalability and integration with existing technologies. However, they suffer from relatively short coherence times, which limits their performance in complex algorithms. Research is focused nowadays towards improvements of performance parameters for theses devices, taking into account the capability of integration in larger and larger

Quantum Processing Units(QPUs).

An alternative possible approach to overcome this limitation is the use of hybrid systems, which combine superconducting circuits with other quantum systems that have longer coherence times. In this way, it is possible to use the superconducting circuits for fast operations and the other systems for long-term storage of quantum information. A good approach for this type of hybridization is the use of macroscopic systems such as spin ensembles. Due to their collective behaviour, the resilience to decoherence is very large in devices built with this technology. Moreover they showed satisfying coupling with superconducting devices in the microwaves regime, and they can be engineered to work at compatible frequencies with superconducting qubits.

Several works [9] show that it is possible to satisfy the needed requirements to implement a quantum memory: such as initialization, storage of an arbitrary state $|\psi_j\rangle$, and readout. Moreover some of these systsems can also act as a quantum register storing multiple qubits in the same ensemble system by using the different degree of freedom of the spins. Protocols for the trigger and readout of the memory have been proposed and demonstrated, inspired by the previous works in this field, in the optical regime.

Implementation

Here a short overview of the main components of a superconducting quantum processor is provided, in order to understand how the spin ensemble quantum memory can be integrated in a larger system.

Usually a superconducting QPU [10] is composed of three main elements:

- **Superconducting qubits:** these are the main computational units of the QPU, they are usually implemented using Josephson junctions and can be manipulated using microwave pulses.
- **Superconducting resonators:** they are implemented using coplanar waveguides, in order to provide a high-quality factor and low loss. They are used to couple the qubits to each other and to the transmission lines.
- **Transmission lines or quantum buses:** these are used to connect the different elements of the QPU and allow for the transfer of quantum information between them. They can be implemented using superconducting coplanar waveguides, and can be designed to have low loss and high coupling. In two qubits gates, they are used to mediate the interaction between the qubits.

Spin ensemble quantum memories can be integrated in this architecture by interaction with superconducting resonators. In this way, it is possible to transfer quantum information between the qubits and the memory using the resonators as intermediaries and the transmission lines as quantum buses, allowing for the interaction also with qubits. In the overall scenario, now we have superconducting qubits electrically coupled to the resonators, a transmission line in between and other resonators which are magnetically coupled to the spin ensemble. Analogously to the two qubit gates implementation [11], the quantum information can be transferred from the qubit to the memory by tuning the frequencies of the resonators and qubits in order to allow for a resonant interaction. Then, by means of specific signals, the ensemble can be initialized, store, and retrieve on-demand the qubit states.

1.3.1 Spin ensembles in semiconductors

A spin ensemble refers to a large collection of quantum spins [12], typically associated with systems such as electrons, nuclei, or other particles that possess intrinsic angular momentum. When considered individually, a spin is a two-level quantum system with a magnetic moment that can align with or against an external magnetic field [13]. However, the behavior of an ensemble of many such spins cannot simply be reduced to that of an isolated particle, because collective properties emerge once the spins are treated as a statistical or coherent group.

In the presence of an external magnetic field, the magnetic moments of the spins experience a torque that drives them into precession around the field axis. On a microscopic level, each spin undergoes this precessional motion with a frequency set by the Zeeman interaction between its magnetic moment and the field strength. In a macroscopic ensemble, however, the superposition of many such individual dynamics leads to a collective magnetization, which can be thought of as a vector quantity representing the average alignment of the spins. This magnetization is the observable that interacts with the field and produces measurable signals, as in magnetic resonance experiments.

At low temperatures or high fields, more spins occupy the lower-energy state aligned with the field, and the ensemble exhibits a measurable polarization. When interactions among the spins are included, such as dipole-dipole couplings or exchange interactions, the dynamics become richer. The spins can no longer be treated as independent, and cooperative effects emerge. These interactions can give rise to decoherence, spin diffusion, and collective modes such as spin waves, where the ensemble behaves more like a correlated many-body system than a collection of independent qubits.

Spin ensembles quantum memories can be based on different physical systems, such as NV centers in diamond, rare-earth ions in crystals, or dopants in semiconductors. In this work, the focus is on the latter, more specifically on dopants in Silicon.

Dopants in Silicon

When dopants such as phosphorous or bismuth are introduced into silicon, their spin degrees of freedom can be studied not only at the level of individual donors but also as ensembles, where the collective behavior of many identical impurities interacting with an external magnetic field gives rise to characteristic transition frequencies and coherence properties. These ensembles form the basis for electron spin resonance (ESR), and they play a crucial role in hybrid quantum devices where many spins couple collectively to microwave cavities or resonators.

For phosphorous-doped silicon [14], the donor electron bound to each phosphorous atom interacts with its nuclear spin (I = 1/2) through the hyperfine interaction. In an ensemble, this leads to two distinct electron spin resonance lines split by the hyperfine constant, approximately 117 MHz. When an external magnetic field is applied, the Zeeman splitting of the electron spin dominates, producing transition frequencies in the gigahertz range, it is then possible to target specific transitions frequency in the microwave domain. The ensemble response is then a pair of resonance lines separated by the hyperfine splitting, reflecting the two nuclear spin projections. The strength of phosphorous ensembles lies in their relative simplicity: two sharp, well-resolved transitions with long ensemble coherence times, especially in isotopically purified ^{28}Si. Their limitation is the modest hyperfine splitting, which constrains spectral selectivity and makes them more susceptible to inhomogeneous broadening compared to larger-spin dopants.

For bismuth-doped silicon, the ensemble dynamics are richer [15]. Each donor has a nuclear spin of I = 9/2, coupled to the electron spin via a hyperfine interaction of about 1.475 GHz. In the ensemble spectrum, this produces twenty possible electron spin resonance transitions between the various hyperfine levels. These transitions span a broad frequency range from hundreds of megahertz to several gigahertz, depending on the applied magnetic field. Notably, at particular "clock transitions" the ensemble exhibits transition frequencies that are first-order insensitive to magnetic field noise, examples occur around fields of a few hundred millitesla, yielding transition frequencies in the interesting 7-8 GHz range. In an ensemble measurement, these transitions stand out as exceptionally narrow and coherent, leading to collective responses with coherence times orders of magnitude longer than

at generic field points. The ensemble of bismuth spins thus provides a spectrum of addressable lines, with the potential to exploit multiple transitions or encode higher-dimensional quantum information across the ensemble. Its drawback is spectral crowding: the many transitions can overlap, and controlling them selectively in an ensemble requires high-resolution techniques and often sophisticated pulse shaping.

1.3.2 Superconducting lumped resonators

In the cavity quantum electrodynamics (cQED) architecture [16], superconducting resonators play a crucial role as the physical implementation of the cavity. These resonators are typically made from superconducting materials and are designed to confine microwave photons in a small volume, allowing for strong coupling between the photons and the superconducting qubits placed inside the cavity. Resonators or cavities can be 3D structures or 2D planar devices, for the purpose of this thesis work, the focus is on planar implementation. The important features of superconducting resonators are the resonance frequency at which photons remain trapped inside the cavity, which has to match the qubit transition frequency, and the quality factor Q, which quantifies how long photons can remain in the cavity before being lost due to dissipation or leakage. A high Q factor is essential for achieving strong coupling and coherent interactions between the qubits and the cavity mode.

CPW resonators

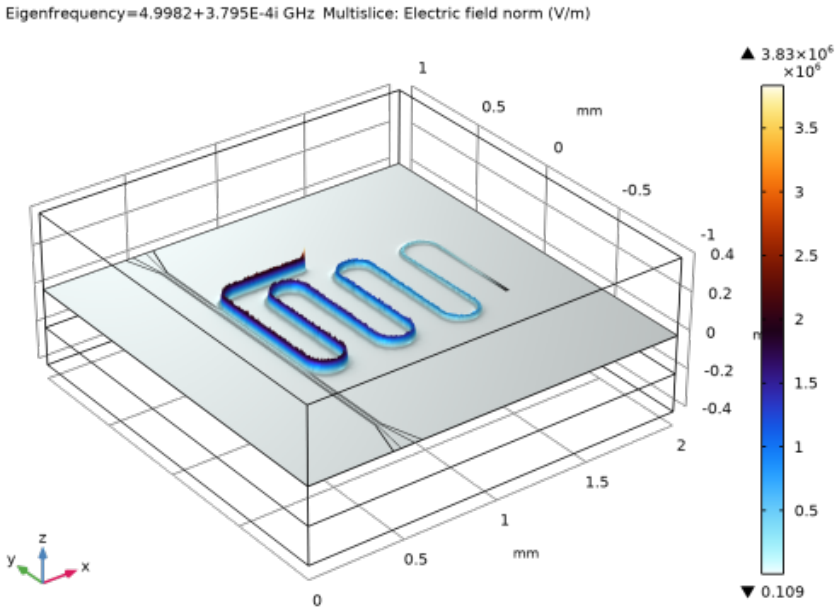

Figure 1.3: Example of a simulation of a coplanar waveguide superconducting $\frac{\lambda}{2}$ resonator for qubits application. Taken from [17].

Usually, when working with qubits in the microwave regime, the resonators are implemented using coplanar waveguides (CPWs) [18]. A CPW consists of a central conductor strip separated by gaps from two ground planes on either side, all fabricated on a dielectric substrate, usually simply Silicon. Waveguides are modeled as transmission lines with a characteristic impedance Z_0, which depends on the geometry of the conductors and the dielectric properties of the substrate. Transmission lines are described as a distributed circuit, with a long series of infinitesimal inductors and capacitors, which account for the magnetic and electric energy stored in the electromagnetic field propagating along the line. From electronics theory, it is known that a transmission line of length l, terminated with an open circuit, can be modeled as a resonator with resonance frequencies given by:

$$f_n = \frac{nv}{2l} \tag{1.4}$$

where n is a positive integer, and v is the phase velocity of the electromagnetic wave in the transmission line, which depends on the effective dielectric constant of the substrate and the geometry of the CPW.

Even though the CPW resonator can support multiple resonance modes, in practice, only the fundamental mode (n=1) is used for coupling with qubits, since it has the lowest frequency and the highest quality factor. By knowing the desired resonance frequency and the phase velocity, it is possible to design a CPW resonator with a specific length to achieve the target frequency. But geometrical factors and effects like kinetic inductance must be taken into account, so the design process usually involves electromagnetic simulations to optimize the geometry and achieve the desired resonance frequency and quality factor.

Finally, the CPW resonators are the first choice for qubits implementation due to their ease in design process and the possibility of obtain an high quality factor in 2D planar devices.

Lumped element resonators

LC circuits are the simplest type of resonators, they consist of an inductor (L) and a capacitor (C) connected in parallel or series.

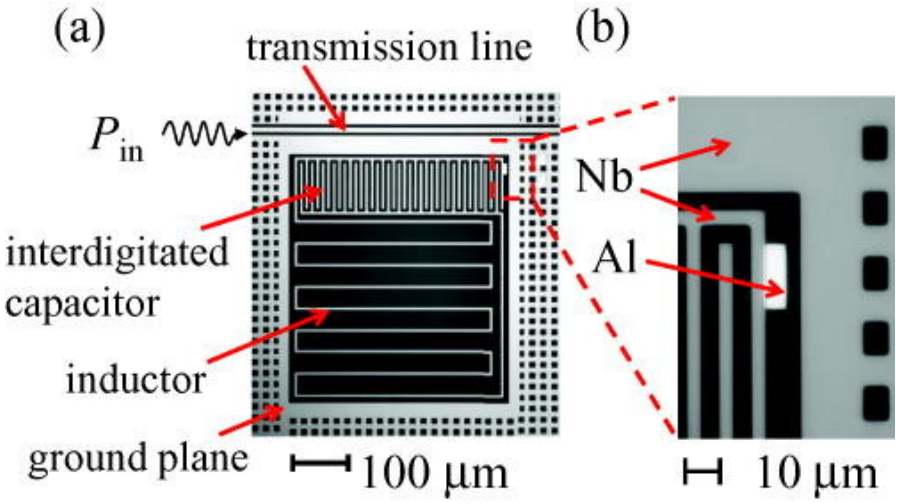

Figure 1.4: Example of a lumped element superconducting resonator, taken from [19].

The resonance frequency of an LC circuit is given by:

$$f_0 = \frac{1}{2\pi\sqrt{LC}} \tag{1.5}$$

While the impedance can be quantified as:

$$Z = \sqrt{\frac{L}{C}} \tag{1.6}$$

Choosing appropriately the L and C values it is possible to design a resonator with a specific resonance frequency, impedance, and quality factor [20]. The lumped element resonator, in fact, is a miniaturized version of the LC circuit, where the inductor and capacitor are implemented as discrete components on a chip. Inductors can be realized as meandered lines or spiral structures, while capacitors can be implemented as interdigitated fingers or parallel plates, with a gap of semiconductor between the metal layers.

As we will see in the next section the lumped element resonators are the common choice for coupling with spin ensembles, since they allow to concentrate the magnetic field in a small volume, increasing the coupling strength with the spins. The general formula to express the collective coupling strength [21] between a spin ensemble and a resonator is:

$$g_0 = \frac{b_1 g \mu_B \omega_{res}}{\sqrt{8\hbar Z}} \tag{1.7}$$

where $b_1 = \frac{B_1}{I}$ is the normalized, position dependent magnetic field, g is the Landé g-factor of the spin, μ_B is the Bohr magneton, ω_{res} the angular resonance frequency of the resonator, and Z its characteristic impedance. The main reason lies in the fact that the coupling strength beteen spins and microwaves in the resonator is inversely proportional to the characteristic impedance of the resonator. While in 2D CPW superconducting resonators for qubits interaction it is not easy to lower the impedance below some tens of ohms, since it would imply a huge loss in the quality factor. By designing lumped element resonators with interdigitated capacitors it is possible to increase sensibly the characteristic capacitance, allowing for a lower impedance and as consequence a stronger coupling with the spins.

We will see in the next section how this is the choice for the resonators in the state of the art solutions. In this implementation the spins are placed directly in the region below the inductor where we expect the maximum concentration of the magnetic field. It can be also possible using some flip-chip techniques to place the spin ensemble directly on top of the inductor.

1.4 State of the art

Inspiration for this work comes from the different state of the art solutions present in literature for this devices. In this section a short overview of the most relevant works is provided, in order to understand the current status of the research in this field, and what kind of problems are tackled in the thesis.

Eichler et al. 2017[21]

This is the first work designing a superconducting lumped resonator with low impedance to be coupled to a spin ensemble. In detail, here a phosphorous doped silicon sample is used as spin ensemble, with a concentration of dopants $5 \times 10^{15} cm^{-3}$, in a layer of $800 ppm$ of residual ^{29}Si. The resonator is designed to have a resonance frequency of $\omega_{res} = 4.96 GHz$, with a characteristic impedance $Z = 8\Omega$, and the loaded quality factor as $Q = 3100$. The superconducting material used is Niobium, which has a high transition temperature of $T_c = 9.25K$, and also a high critical magnetic field, which allows to work with external fields up to some hundreds of millitesla. In fact to allow the spins to interact with the resonator, an external magnetic field $B_0 = 180mT$ is applied in-plane of the resonator, this is used as the external pumping of activation of the Zeeman splitting.

This work measured an ESR detection of $2 \times 10^4 spins$ with $SNR = 1$, they also showed the measurements of coherence times T_1 of the single spins dependent on the detuning of the resonator. This improved the amount of detected spins of two orders of magnitude with respect to previous works. The key feature to achieve these results are shown as the improved geometry of the resonator, which allowed to increase the coupling strength and the use of a parametric amplifier during measurements.

Ranjan et al. 2020[9]

A differet type of resonator is designed, the objective is to interact with Bismuth dopants in Silicon. As explained in the previous section, Bismuth has a larger hyperfine splitting with respect to Phosphorous, this allows to work at higher frequencies without rising the magnitude of the static magnetic field. In any case if the frequencies of the resonator and the spins are not matching, it is possible to tune the transition frequencies of the spins by increasing the field. In the experiments, in fact the authors still used a $27mT$ in-plane field in order to work at $\omega_{res} = 7.338 GHz$. The material used here is a thin film of Aluminum, which has a lower critical field with respect to Niobium, but it is easier to be deposited and patterned.

The measured here where performed to show a full quantum memory protocol using a two pulse echo sequence, in oreder to store quantum state arriving from transmons. Coherence times have been measured as long as $100ms$, demonstrating the feasibility of using clock transitions of Bismuth for hybrid devices. Also here possible improvements consists in increasing the coupling factor, improving the geometry and using a magnetic field resistive superconductor.

Chang et al. 2024[22]

This example, instead, shows a different approach for the implementation of a hybrid quantum memory. It is reported in order to have a larger view of the different implementations possible, in these quantum devices. The work reported in Chang's paper is at the frontier of the technology, it needs extensive simulations and design processes, but mostly requires state of the art fabrication techniques.

This hybrid approach instead of focusing on ensembles is based on single spin donors in Silicon, coupled using the oscillating fields in superconducting flux qubits. The circuit here is very different, it does not use lumped resonators, but a normal CPW resonator used to couple the flux qubits inside the cavity. Superconducting metal is still Aluminum, and the single spins are Bismuth dopants in Silicon, with the idea of using an absent magnetic field. Here the objective is to show that also quantum devices can be a valuable alternative to resonators, and they can still carry the quantum information to be stored in the spins.

Overall, satisfactory interaction between the flux qubits and the spins is shown, with a coupling strength of $g/2\pi = 1.8MHz$. With a spin-echo protocol coherent oscillations are seen between the flux and spin precession frequencies.

1.5 Thesis objectives and structure

After this overview to the field of hybrid quantum memories and the existing solutions, the objective of this thesis work is to provide an alternative superconducting platform for interaction with spin ensembles. In this section an overview of the objectives and the structure of the thesis is provided, but also what kind of problems are adressed.

1.5.1 Adressed problem

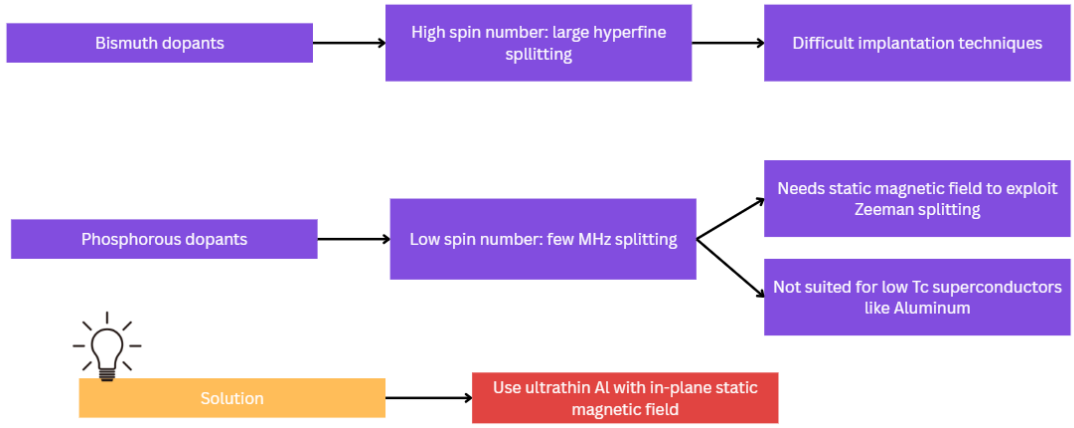

Figure 1.5: Decision process behind the thesis.

As explained in the previous sections, the magnetic field introduces some problems in the superconducting devices. In fact, the presence of an external magnetic field can lead to the formation of vortices in the superconductor, which can cause dissipation and loss of coherence in the resonator. This is especially problematic in planar resonators, where the magnetic field can penetrate the thin film and create vortices. To mitigate this problem, the resonators are usually designed to have a high critical field, but this limits the choice of materials and geometries. In particular Phosphorous dopants in Silicon require a magnetic field of at least $180mT$ to work at a frequency compatible with superconducting qubits, but the critical field of Aluminum, the most popular metal in superconducting circuits, is around $H_c = 100mT$ at $0K$. The alternative is the use of high field superconductors such as Niobium or Niobium Titanium Nitride, but these materials cannot be evaporated and they require plasma sputtering techniques. On the other hand, the alternative dopant is Bismuth, which has a larger hyperfine splitting, allowing to work at higher frequencies with lower magnetic fields. Unfortunately Bismuth implantation in Silicon is not a well established technique and obtaining a high quality doping is challenging, while Phosphorous is easier. So, we wanted to explore the possibility of using the most popular superconductor in quantum circuits, Aluminum, and try to design a resonator which can work at higher fields with respect to the state of the art, in order to make it compatible with Phosphorous donors for quantum memories applications.

1.5.2 Objectives

The main objective of this thesis work is to design, fabricate, and measure a superconducting lumped element resonator capable of operating in the presence of an in-plane magnetic field for the activation of Phosphorous donors. During the developement of the project, several sub-tasks had been accomplished. Firstly, two designs have been developed, one for the Phosphorous donors and the other for the Bismuth donors, in which two different resonance frequencies are targeted. Moreover, the target material of application is not only Aluminum but also Niobium. During the simulations it is also discovered that the characteristic parameters of the resonator do not change with the superconducting material used.

1.5.3 Structure

The thesis is structured as follows:

- In **Chapter 2** the design process is explained, together with the tools used. And the FEM simulation method, using COMSOL, is described to give an idea of the validation process.
- In **Chapter 3** is illustrated the implemented fabrication recipe and a description of the process inside PiQuET cleanroom. The different steps of the process are explained, with the details of the cleanroom techniques used.
- In **Chapter 4** the measurement setup is explained, giving particular attention to dilution refrigerators, together with the different electronical components used to perform the measurements. A side task of the thesis was the design and building of a cold finger used for support of the devices during magnetic field measurements, this is also explained in detail.
- In **Chapter 5** the results of the measurements are presented, with the analysis of the data and the comparison with the simulations.
- In **Chapter 6** the conclusions are drawn, with the discussion of the results and the future perspectives of the work.

Chapter 2

Device design

2.1 Requirements

This section outlines the design requirements for the device, including performance specifications, physical dimensions, and operational conditions. These requirements has been defined based on the considerations and preliminary analysis performed in chapter 1. In this section the requiremets are intended for the lumped resonator, not for the whole memory itself, even though, clearly, their compatibility must be considered.

The design process targeted two types of resonators: one that interacts with Phosphorus donors and the other with Bismuth ones. The requirements for both types of resonators are similar, with the main difference being the resonance frequency.

P-donors resonance frequency

The hyperfine splitting of Phosphorus donors in Silicon is 117 MHz. This makes the hyperfine levels incompatible with applications in the microwave regime. To overcome this limitation, it is possible to use the Zeeman effect to split the energy levels further. The application of a static magnetic field B_0 causes the energy levels to split, allowing for transitions that fall within the microwave frequency range. In literature we found that in the aforementioned paper from Eichler et al. [21], the authors used a magnetic field of $B_0 = 180\,\mathrm{mT}$ to achieve a resonance frequency of $\omega_0 = 4.96\,\mathrm{GHz}$. The use of a magnetic field of few hudreads of mT was compatible with the possible experimental capabilities, and for this reason it has been decided to target a resonance frequency around $\omega_0 = 5\,\mathrm{GHz}$. With the possibility of tuning the Zeeman splitting and consequently the transition frequency of the spins using a magnetic field, it is possible to cover a range of frequencies around the target

one, allowing for small errors in the simulation process.

Bi-donors resonance frequency

On the opposite side, Bismuth donors in Silicon have a much larger hyperfine splitting of $A_{Bi}/h = 7.375\,\text{GHz}$. This makes them highly suitable for applications in the microwave regime without the need for an external magnetic field. Moreover having a very high spin number $S = 9/2$ allows for a large number of hyperfine levels [23], and consequently a large number of possible transitions called Clock Transitions(CT). The amount of targeted frequencies is thus very large and it is possible to choose the one that best fits the experimental capabilities, also without using the external magnetic field. The base transition frequency poses a lower limit to the resonance frequency of the resonator, as it is not possible to tune the donors below it. Considering the possibility of unwanted parasitic inductances that can arise during fabrication or due to heavier kinetic inductance effects, it has been decided to target a resonance frequency of around 7.5 GHz.

Quality factor

The quality factor Q is a measure of the energy loss relative to the energy stored in the resonator, when at resonance [24]. A high quality factor indicates low energy loss and a narrow bandwidth($\Delta_{3dB}f$), while a low quality factor indicates higher energy loss and a broader bandwidth.

$$Q = \frac{f}{\Delta_{3dB}f} \tag{2.1}$$

The quality factor is related to the photon lifetime τ in the resonator by the following equation:

$$Q = 2\pi f\tau \tag{2.2}$$

Losses in the resonator can arise from various sources, the most dominant are feedline and dielectric losses of the substrate. An high Q is usually targeted to maximize the photon lifetime and the interactions of the resonator. In this case it is sacrified to increase their impedance, but it is still important to keep it as high as possible. In Eichler's work enlarging the quality factor is stated as a possible improvement to their device. We tried to maintain its value as high as possible, with a minimum target of the value yet present in literature $Q_{min} = 3000$.

Impedance

From equation 1.7 it is possible to see that the coupling strength is maximized for a very low value of the resonator characteristic impedance Z. This justifies the

choice of a lumped element resonator, as they can achieve very low characteristic impedances, in the order of few Ohms. The main point of these resonator is the use of interdigitated capacitors, these device can have very high capacitances by using long and thin fingers interleaved with small gaps. As the capacitance increases, to target the same resonance frequency, the inductance has to decrease, and so also the characteristic impedance. The inductance is usually implemented using a meandered wire, by shortening and narrowing the wire the inductance can be increased, while by widening and lengthening it the inductance can be decreased.

In general, we wanted the impedance to be very low with a maximum value $Z_{max} = 10\,\Omega$.

Superconducting material

The resonator has to be fabricated using superconducting materials acting as perfect conductors at cryogenic temperatures. The experimental setup consists of a dilution refrigerator, which can reach temperatures in the order of few tens of mK. This allows the use of basically every superconducting metal, but the main limitation here is the presence of a static magnetic field. A magnetic field, higher then the critical field H_c, can cause the superconductor to enter in the normal state, thus losing its superconducting properties and destroying the operativity of the resonators.

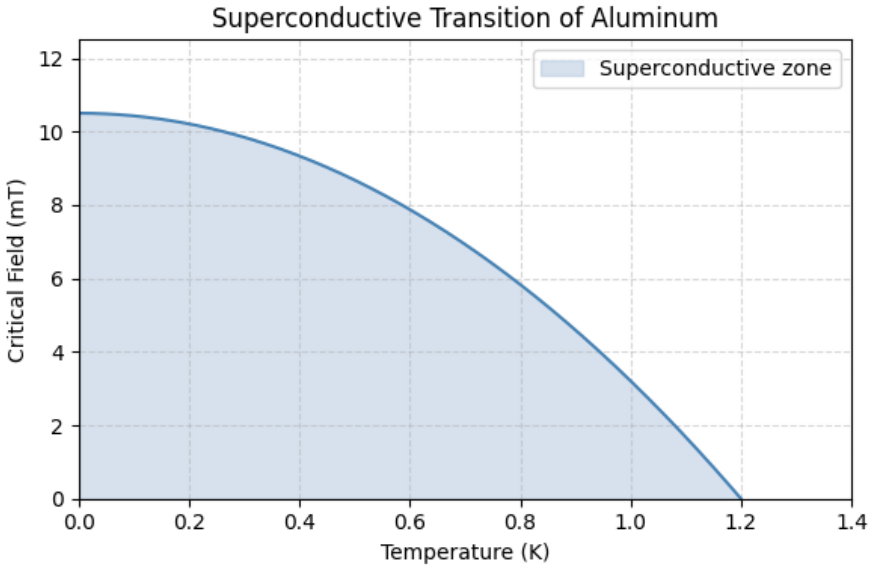

Figure 2.1: Superconductivity transition diagram for Aluminum.

The critical field is a property of the superconductor material [25], and it depends

on the temperature of the metal:

$$H_c(T) = H_c(0)\left[1 - \left(\frac{T}{T_c}\right)^2\right] \tag{2.3}$$

Where $H_c(0)$ is the critical field at absolute zero and T_c is the critical temperature of the superconductor. For this reason, the choice of the superconductor has to be made considering the critical field at the operating temperature.

In this specific application the presence of a static magnetic field is required to tune the resonance frequency of the P-donors, thus it must be allowed the operativity of the resonator at 200 mT. This requirement is quite challenging, as most common superconductors have a critical field lower than this value. Usually in applications requiring high magnetic fields, Nobium and some of its leagues, Niobium Nitride (NbN) or Niobium Titanium Nitride (NbTiN) , are used as they have a very high critical field reaching also 15 T. For this application Niobium has an high enough critical field of up to 400 mT.

Unfortunately Niobium cannot be evaporated with e-beam lithography, this makes its fabrication unfeasible with the available instrumentations. So, the main idea behind this thesis was to use a superconducting thin film of Aluminum which has been demonstrated to be able to withstand magnetic fields up to 1 T when granular [26] or with an in-plane magnetic field [27]. In this way we could avoid the need of a sputtering system for Niobium, and we could use the e-beam evaporation system available in the cleanroom, even though the deposition of thin films requires several further considerations. Aluminum is one of the most used and studied metals for superconductors, the demonstration of its operativity at high magnetic fields and in this application can enhance the possibility of usage also in the field of high transitions superconductors.

Substrate material

The substrate material has to be a good insulator, with low dielectric losses at microwave frequencies and cryogenic temperatures. The most common material used in superconducting resonators and qubits applications is high resistivity intrinsic Silicon. The initial test phase of the resonators does not require the presence of Phosphorous donors in the lattice, so it is possible to use this available low loss substrate. For the target application instead, it will be necessary to use a Silicon substrate doped with Phosphorus or Bismuth donors implanted in an epitaxially grown layer of few micrometers with very low residual ^{28}Si.

To summarize the materials used for the fabrication of the resonators are:

- Superconductor: Aluminum thin film of thickness $t \approx 10\,\text{nm}$
- Substrate: High resistivity intrinsic Silicon for testing or ^{29}Si doped with P or Bi donors in the final application

Fabrication

The fabrication of the resonators has to be compatible with the available cleanroom facilities and materials, but also the final chip has to be compatible with the experimental setup in the dilution refrigerator. The standard chip size used in the lab is $10 \times 10\,\text{mm}^2$, this is compatible with the sample holder and the PCB used to connect the chip to the external electronics. To allow for an easier fabrication the design had to comply with a critical dimension limit of $CD \approx 1\,\text{um}$, to allow us the use of the UV laser writer machine, this does not look to be a problem as the resonators do not require very small features. In PiQuET lab two different e-beam evaporator machines are available and both are equipped with Aluminum crucibles, and although fine control is needed it is possible to reach few nanometers of thin film depositions as needed. Regarding the sputtering system, for Niobium depositions, the cleanroom facility is still mounting the new machine, and so it is not yet operational. This deposition task has been performed in collaboration with CNR division of Naples. The available substrates were high resistivity intrinsic Silicon wafers of dimension 2" and thickness 275 um, with the available area is possible to accommodate 12 dies of the aforementioned size.

2.2 Layout definition

The layout of the resonators has been designed to meet the requirements outlined in the previous section. The design process involved several iterations and optimizations to achieve the desired performance while considering fabrication constraints and material properties.

The resonators are designed as lumped element resonators, consisting of an interdigitated capacitor and a meandered inductor. The interdigitated capacitor is formed by multiple fingers of metallic strips interleaved with gaps, allowing for a high capacitance in a compact area. The meandered inductor is designed to provide the required inductance while minimizing parasitic capacitances and losses.

The resonators are coupled to a coplanar waveguide (CPW) feedline for transmission and reflection measurements. The coupling strength is controlled by adjusting the distance between the resonator and the feedline, as well as the geometry of the coupling capacitor. The feedline is designed to have a characteristic impedance of

$Z_0 = 50\,\Omega$ to match standard microwave equipment.

The overall layout is designed to fit within the constraints of the chip size, while ensuring that the resonators are sufficiently spaced to minimize crosstalk and interference. Ground planes and shielding structures are incorporated to reduce electromagnetic interference and improve the quality factor of the resonators.

The design process also involved simulations using electromagnetic simulation software to optimize the resonator parameters and predict their performance [28]. These simulations helped in refining the dimensions and geometries of the resonator components to achieve the desired resonance frequencies and quality factors.

The final layout is prepared for fabrication, with all necessary design files and documentation to ensure a smooth transition to the fabrication process.

2.2.1 Device parameters and geometrical considerations

Eichler's resonators

To start with a known point, the design of the resonators has been based on the parameters reported in Eichler's paper [21], as they have been demonstrated to work properly. These resonators have a metal strip width of $w = 2\,\mu\text{m}$, a length of $l = 100\,\mu\text{m}$. The interdigitated capacitor has 60 fingers per side of variable length following a triangular-like shape, with each finger having width and gap of few micrometers. This results in resonators with a resonance frequency of $\omega_0 = 4.96\,\text{GHz}$, a quality factor of $Q = 3100$ and a characteristic impedance of $Z = 8\,\Omega$.

Geometrically, the resonator spans over a rectangle with an area of around $1\,\text{mm}^2$. On one side it is capacitively coupled to the CPW feedline, while on the two adjacent sides it is present an alternation of fingers for the interdigitated capacitance. They form a triangular like shape, with length of the fingers decreasing as they get closer to the center of the resonator. Here a meandered inductor is present, with the characteristic dimensions mentioned before. The resonator is surrounded by a ground plane, with a gap of few micrometers from the resonator itself.

These types of resonator can be considered in lumped elements as a central inductor L in parallel with two equal capacitors each with half the characteristic capacitance $C/2$. Losses and kinetic inductance effects are considered as a parasitic inductor L_p in series with the central inductor L. The resonator is coupled to the feedline with a coupling capacitor C_c. The overall resonance frequency and

impedance of the resonator is then given by:

$$\omega_0 = \frac{1}{\sqrt{(L + L_p)C}} \tag{2.4}$$

$$Z = \sqrt{\frac{L + L_p}{C}} \tag{2.5}$$

Circuit structure

After understanding the structure of the resonators, the next step is to understand how to geometrically modify them to reach the target parameters. The resonance frequency can be tuned by changing the inductance or the capacitance of the resonator. At the initial stage it is possible to target a specific frequency using some analytical formulas, unfortunately being the resonator a distributed element, these formulas can only give a rough estimate of the parameters. After this first estimation, it is necessary to use electromagnetic simulation software to fine tune the parameters and reach the desired frequency. In any case these analytic formulas can give an idea of how to change the geometry to reach the target frequency, and the amount of impact a specific change will have on the frequency can be estimated.

A detailed description of these resonator from the analytical point of view can be found in the paper by McKenzie et al. [29]. For the sake of completeness, the analysis performed during the workflow is reported here.

Inductance

The inductance consist of a stripline, which is a very simple element to analyze In fact the stripline have only 3 free parameters: width w, length l and thickness t. Regarding the thickness, it is usually fixed by the fabrication process, and so it is not a free parameter, moreover it is shown as it has not significant impact on the classical inductance. The inductance of a stripline can be approximated using the following empirical formula:

$$L = 0.002l \left[\ln\left(\frac{2l}{w+t}\right) + 0.5 + \frac{w+t}{3l} \right] \quad \text{[nH]} \tag{2.6}$$

where l, w and t are in micrometers. As stated previously, being the thickness not larger than few hundreads of micrometers its term is not actually relevant compared to a width of few micrometers. The inductance can be tuned by changing the width or the length of the stripline, with a larger impact given by its length. For practical considerations, regarding limitations in the critical dimensions, the width

of the stripline was imposed to be not smaller than 2 µm. The most important free parameter is thus the length, which can be changed by changing the geometry of the meandered wire. Also for uniformity during the verification and validation stage the shape of the meandered wire has been imposed as straight, and only its length value has been changed.

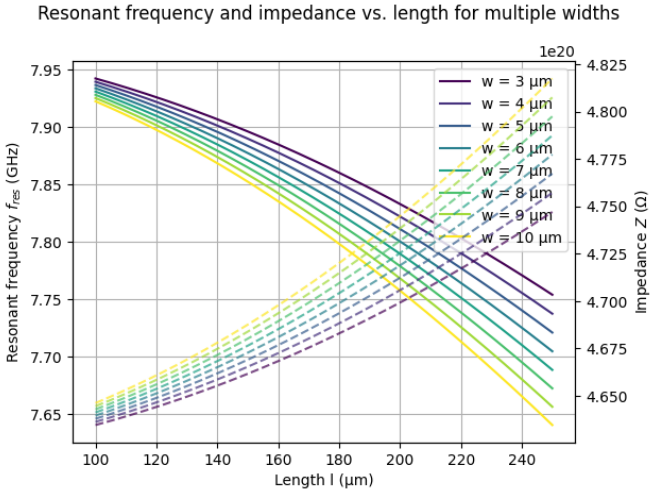

Figure 2.2: Variation of the resonance frequency for given capacitive structure by changing its inductor meandered wire length and width.

Actually the effects of kinetic inductance must be taken into account, but due to the complexity of the phenomenon this effect is simulated using FEM analysis, a more detailed treatment is present in the next section.

Capacitance

The capacitance is given by the interdigitated capacitor, which is a more complex structure to analyze. The interdigitated capacitor has several free parameters, the most important are the number of fingers N_f, the length of the fingers l_f, the width of the fingers w_f and the gap between fingers g_f. In this particular configuration instead of having a rectangular shape, the fingers are arranged in a triangular-like shape, this makes the analysis more complex and requires an adjustment to common approaches used in literature

A complete analytical treatment is performed by Igreja and Dias [30], the authors here derive formulas considering iterative structures of fins with the same width and spacing. The considered parameters are: the length of the fingers l_f, the metalization rate $\nu = \dfrac{w_f}{w_f + g_f}$, using respectively the width of the fingers w_f

and the gap between fingers g_f, the number of fingers N_f and the dielectric coefficients of vacuum $\epsilon_0 = 8.854 \times 10^{-12}\,\mathrm{F/m}$ and the substrate (for Silicon $\epsilon_r = 11.45$).

Regarding the issue with the triangular shape, the approach is suggested by McKenzie et al. [29] in the supplementary materials. It basically consists in considering the two half interdigitated capacitors of each side, with n fingers each and a maximum l_{max} and minimum l_{min} lengths of the finger, as a single capacitor with n electrodes and an effective length $l_{eff} = l_{max} + l_{min}$.

Handling the capacitance is not an easy task as it is not possible to change all the parameters freely. Changing the length of the fingers and the metalization rate, although possible, would have implied a great change in the layout of the resonator considering the way it has been practically drawed. For this reason, the design process involved starting from a quite big capacitance with definite length and metalization rate, and then the fine tuning can be performed moving the only free parameters left: the number of fins.

2.3 Drawing with Qiskit metal

The layout of the resonators and full circuits has been designed using Qiskit Metal [31]. Qiskit Metal is an open-source framework designed for the design, simulation, and optimization of superconducting quantum devices. It provides a parametric and object-oriented approach to device design, where components such as transmon qubits, coplanar waveguide resonators, and coupling elements can be defined as modular objects with adjustable geometric and electrical parameters. Each component can be instantiated multiple times with different parameters, enabling systematic studies of design variations and scalability. The framework supports the creation of complete quantum chip layouts, including routing of control and readout lines, and can export these layouts in standard fabrication formats such as GDSII, ensuring compatibility with microfabrication processes. A central feature of Qiskit Metal is its integration with full-wave electromagnetic (EM) solvers, including commercial software like Ansys HFSS, allowing detailed simulation of device properties such as resonant frequencies, mode shapes, coupling strengths, quality factors, and potential loss channels. The parametric definition of components allows automated sweeps over design parameters, facilitating optimization routines that minimize undesired crosstalk or frequency crowding between qubits. Qiskit Metal also provides visualization and verification tools for inspecting component placement, connectivity, and symmetry, helping to ensure that the designed layout meets both physical and fabrication constraints. Its modular architecture, combined with parametric control and EM simulation support, makes it a versatile tool for

the iterative development of high-coherence superconducting quantum circuits.

2.3.1 Component definition

In Qiskit Metal, components are defined using a combination of geometric primitives and parametric properties. Each component is represented as a Python object, which can be customized by setting its attributes. For example, a transmon qubit can be defined by specifying its Josephson junction parameters, capacitance values, and geometric dimensions. This object-oriented approach allows for easy manipulation and reuse of components across different designs. In this work, the use of Qiskit Metal was limited to the design of superconducting resonators, which did not need a quantum description like qubits or SQUIDs usually designed with it.

2D plane and components

With Qiskit Metal you can draw the layout of your circuit directly on a 2D plane, by defining the regions of the plane which are not grounded, like CPW feedlines, resonators and qubits. The other regions can be subtracted to metalization, meaning that they represent the substrate, while all the missing space is considered as a ground plane. It comes with a library composed by a set of standard components like CPW feedlines, transmon qubits, resonators and so on, which can be instantiated and customized by changing their parameters. If a component is not available in the standard library, it is possible to define a custom component by creating a new class that inherits from the base component class. This custom class takes in input the necessary parameters and implements a method to generate the geometric layout using Qiskit Metal's drawing primitives. Drawing primitives are based on the Shapely library, which provides a set of geometric objects and operations for creating and manipulating 2D shapes.

Lumped resonator component

Not being a standard component, the lumped resonator has been defined as a custom component, with its proper class. The goal is to create a parametric component that can be easily instantiated with different parameters to create resonators with different frequencies, impedances and quality factors. This class in fact has been used to create both resonators for P-donors and Bi-donors, which have different target frequencies. Moreover the class has been designed to allow the easy modification of the resonator parameters, to create different versions of the resonator for the verification and validation step.

The component takes in input the geometrical parameters, this allows for a complete control of the resonator geometry and the possibility to change its parameters to reach the target frequency and impedance.

Ones instantiated the class calls its .make() method, which draws the resonator on the 2D plane using Qiskit Metal's drawing primitives. The drawing process involves the addition and subtraction of several rectangles of different sizes for each of the needed geometric features. The interdigitated capacitor is drawn using an iterative approach that increased the dimensions of the fingers by subtracting the gaps to the small box metallic layer. It is possible to give the component the parameters of number of electrodes per side and equivalent length of the fingers, while the minimum length is given by the width of the inductor box. By defining width and gap of the fingers, the control on metalization ratio is also possible. This allows for further control of the capacitance, by controlling its crucial parameters.

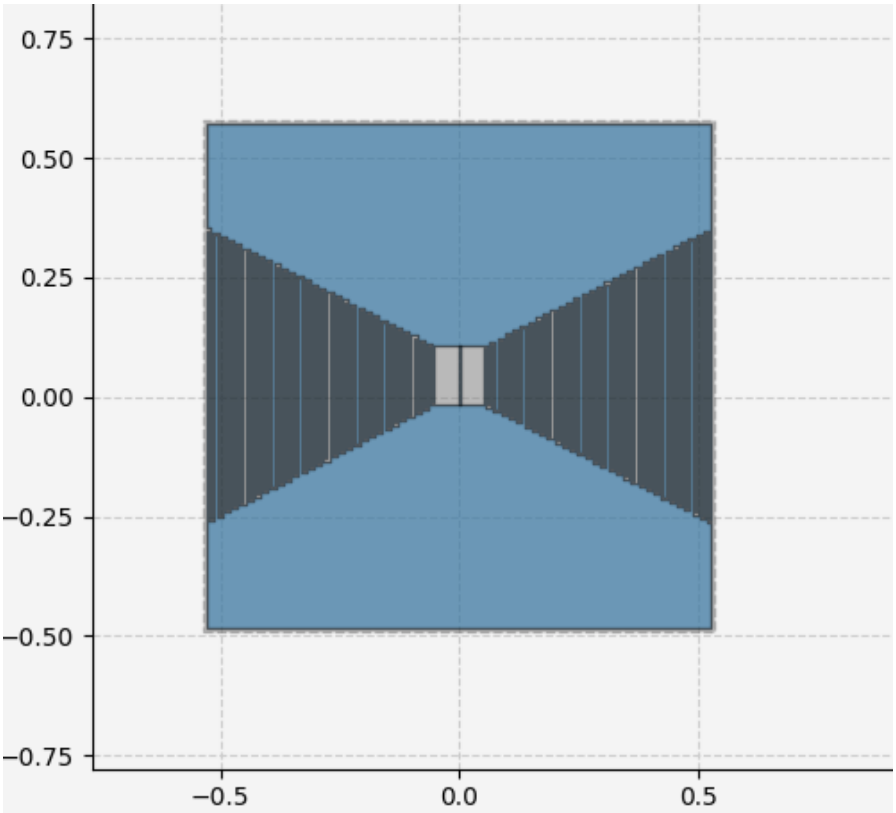

Figure 2.3: Lumped resonator layout on qiskit metal.

Coupling to feedline

To simulate the behaviour of the resonator in a realistic scenario, it is necessary to couple it to a feedline. As like as in the fabricated devices, the feedline is composed as a coplanar waveguide (CPW) with a characteristic impedance of $Z_0 = 50\,\Omega$, with one launchpad per side of dimensions compatible with the bonding process. The components used are both contained in the standard library of Qiskit Metal. It is possible to define the feedline as a straight CPW, with a defined width and gap to the ground plane, the standard value of width is $W = 10\,\mu m$ and the gap is $G = 6\,\mu m$, corresponding to a characteristic impedance of $Z_0 = 50\,\Omega$. The launchpads instead have several parameters which allow to define its geometry and its connection to the CPW.

The coupling between the resonator and the feedline is achieved using a coupling capacitor, which is implemented as a small section of CPW with a defined length and gap to the ground plane. The coupling capacitor is drawn using the same drawing primitives as the resonator, and it is positioned at a defined distance from the resonator. The coupling strength can be adjusted by changing the length of the coupling capacitor or the distance between the resonator and the feedline. This is also a parameter which must be tuned in the verification and validation step. A strong coupling to the feedline can cause a decrease in the quality factor of the resonator, a small coupling instead does not allow for efficient photons transfer, so it is important to find a balance between coupling strength and quality factor.

From the design to the simulator: SQDMetal

To simulate the behaviour of the resonator, it is necessary to export the design from Qiskit Metal to a format compatible with the electromagnetic simulator. In our case the available simulator was COMSOL Multiphysics. Unfortunately Qiskit Metal does not have a direct export to COMSOL, which in turn does not accept CAD files import without a specific license. In order to allow the simulation, we had to find a workaround to convert the design files into a compatible format. This was achieved using the open-source software called SQDMetal [32]. This software works as a bridge between Qiskit Metal and COMSOL, by taking the design objects from Qiskit Metal it draws automatically, by means of JAVA APIs the same geometry into COMSOL. It defines also the materials and the boundary conditions, to allow for a smooth transition from the design to the simulation. This allows for a seamless workflow from the design to the simulation, without the need for manual conversion of the design files.

2.4 Verification and validation

The verification and validation step is crucial to ensure that the designed resonators meet the target specifications and perform as expected. This process involves simulating the resonators using finite element method (FEM) analysis to evaluate their electromagnetic properties, including resonance frequency, quality factor, and impedance. The simulations are performed using COMSOL Multiphysics, a powerful tool for solving complex physical problems using FEM.

The workflow involves several steps:

- Importing the resonator design from Qiskit Metal using SQDMetal to ensure accurate representation of the layout.
- Setting up the simulation environment in COMSOL, including defining the geometry, materials, and boundary conditions.
- Performing FEM analysis to calculate the resonant frequencies, quality factors, and impedance of the resonators.
- Analyzing the simulation results to verify that the resonators meet the target specifications.
- Iterating on the design geometrical parameters as necessary based on simulation results to optimize performance.

This iterative process continues until the resonators achieve the desired performance metrics.

All of these steps are detailed in the following subsections.

2.4.1 FEM analysis for superconducting circuits

Finite Element Method (FEM) analysis is a numerical technique used to solve complex physical problems by discretizing the problem domain into smaller, simpler elements. In the context of superconducting circuits, FEM analysis is particularly useful for simulating the electromagnetic properties of devices such as resonators, qubits, and waveguides.

FEM analysis allows for accurate modeling of the intricate geometries and material properties present in superconducting circuits, enabling the prediction of their behavior under various operating conditions. By solving Maxwell's equations within the FEM framework, we can obtain valuable insights into the electromagnetic fields,

currents, and potentials within the devices.

In this work, FEM analysis is employed to simulate the designed lumped element resonators, allowing for the evaluation of key performance metrics such as resonance frequency, quality factor, and impedance. In particular the analysis is performed in the frequency domain, which is suitable for studying steady-state responses of the resonators to harmonic excitations. This approach enables the identification of resonant modes and the assessment of their characteristics, providing a comprehensive understanding of the resonator's performance.

Frequency domain EM simulation

The principle behind frequency domain EM simulation is to solve a particular set of Maxwell's equations in the frequency domain. The main objective is to find the electric field $\mathbf{E}$ and magnetic field $\mathbf{H}$ distributions within the simulation domain, given a set of boundary conditions and material properties.

Recall Maxwell's equations in the time domain:

$$\nabla \cdot \mathbf{D} = \rho \tag{2.7}$$

$$\nabla \cdot \mathbf{B} = 0 \tag{2.8}$$

$$\nabla \times \mathbf{E} = -\frac{\partial \mathbf{B}}{\partial t} \tag{2.9}$$

$$\nabla \times \mathbf{H} = \mathbf{J} + \frac{\partial \mathbf{D}}{\partial t} \tag{2.10}$$

We are looking for time-harmonic solutions, where the fields vary sinusoidally with time at a specific angular frequency ω. This allows us to express the fields as:

$$\mathbf{E}(\mathbf{r}, t) = \mathbf{E}(0)e^{j\omega t - k\mathbf{r}} \tag{2.11}$$

$$\mathbf{H}(\mathbf{r}, t) = \mathbf{H}(0)e^{j\omega t - k\mathbf{r}} \tag{2.12}$$

Substituting these expressions into Maxwell's equations and applying the phasor representation, we obtain the frequency domain form of Ampere's and Faraday's laws:

$$\nabla \times \mathbf{E} = -j\omega\mathbf{B} \tag{2.13}$$

$$\nabla \times \mathbf{H} = \mathbf{J} + j\omega\mathbf{D} \tag{2.14}$$

Considering the relations for current, displacement, and magnetic flux densities:

$$\mathbf{J} = \sigma\mathbf{E} \tag{2.15}$$

$$\mathbf{D} = \epsilon\mathbf{E} \tag{2.16}$$

$$\mathbf{B} = \mu\mathbf{H} \tag{2.17}$$

We can rewrite the frequency domain Maxwell's equations as:

$$\nabla \times \mathbf{E} = -j\omega\mu\mathbf{H} \tag{2.18}$$

$$\nabla \times \mathbf{H} = (\sigma + j\omega\epsilon)\mathbf{E} \tag{2.19}$$

Finally we can combine these equations to obtain the wave equation for the electric field:

$$\nabla \times \left(\frac{1}{\mu_r}\nabla \times \mathbf{E}\right) - k_0^2(\epsilon_r - \frac{j\sigma}{\omega\epsilon_0})\mathbf{E} = 0 \tag{2.20}$$

This equation describes the behavior of the electric field in a medium with relative permittivity ϵ_r, relative permeability μ_r, and conductivity σ at a given angular frequency ω. By imposing this equation on the simulation domain, along with appropriate boundary conditions and material properties, we can solve for the electric field distribution using FEM analysis.

2.4.2 Superconductors modeling

Superconductors are materials that exhibit zero electrical resistance and the expulsion of magnetic fields below a certain critical temperature. In the context of FEM analysis, modeling superconductors requires special attention to their unique electromagnetic properties, particularly the nonlinear response of the superconducting order parameter. The behavior of superconductors can be described by the London equations, which relate the supercurrent density to the electromagnetic field. In the frequency domain, we can express the supercurrent density as:

$$\mathbf{J}_s = -\frac{n_s e^2}{m}\mathbf{A} \tag{2.21}$$

where n_s is the superfluid density, e is the elementary charge, m is the effective mass of the Cooper pairs, and $\mathbf{A}$ is the vector potential.

Incorporating the effects of superconductivity into our FEM simulations involves modifying the material properties to account for the nonlinear response of the supercurrent density to the applied electromagnetic fields. In FEM analysis it is necessary to define some boundary conditions and laws to properly model the physical behaviour of the system that is being simulated. In RF simulations you can define some boundaries as perfect electric conductors (PEC), which impose that the tangential component of the electric field is zero on the surface of the conductor,

$$\mathbf{E} \cdot \mathbf{n} = 0$$

. This basically models the behaviour of a superconductor, as it approximates an infinite conductivity and does not allow for magnetic fields to penetrate its surface.

Kinetic inductance

The simulation has to take into account for the effect of kinetic inductance. Kinetic inductance arises from the inertia of charge carriers, particularly Cooper pairs in superconductors, which store energy in their motion when the current changes. Unlike geometric inductance, which depends on magnetic field energy around a conductor, kinetic inductance reflects the kinetic energy of the superfluid carriers themselves. It becomes significant when the superconducting film is thin or when the superfluid density is low, since:

$$L_k = \frac{m^*}{n_s e^2 A} \tag{2.22}$$

increases as n_s or the cross-section area A decreases. This effect is especially pronounced in disordered or granular superconductors such as NbN, TiN, or WSi, and in ultrathin or low-dimensional materials where the London penetration depth is comparable to or exceeds the film thickness. The inductive response also depends on temperature through the superfluid density, increasing sharply near the critical temperature.

In this application, the resonators are made from a thin film of Aluminum with a thickness of around 10 nm or of thicker Niobium layers which is an high temperature superconductor. So, it is possible that the effects of kinetic inductance are not negligible, and they must be taken into account to accurately predict the resonator's performance.

By the Drude model of conductivity, the superconductors have a complex conductivity:

$$\sigma(\omega) = \sigma_1(\omega) - j\sigma_2(\omega) = \frac{ne^2\tau}{m^*(1 + j\omega\tau)} \tag{2.23}$$

it expresses the dependence on frequency of the conductivity, where τ is the scattering time of the charge carriers, n is the charge carrier density, and m^* is the effective mass of the charge carriers. The real part accounts for the resistive losses, while the imaginary part accounts for the inductive response. In the case of superconductors, the imaginary part is dominant and it takes into account for the kinetic inductance. We can take a closer look at the two components:

$$\sigma_1(\omega) = \frac{ne^2\tau}{m^*(1 + \omega^2\tau^2)} \tag{2.24}$$

$$\sigma_2(\omega) = \frac{ne^2\tau^2\omega}{m^*(1 + \omega^2\tau^2)} \tag{2.25}$$

In normal metals, the scattering time τ is very small, so for microwave frequencies $\omega \approx 10^{10}$ Hz the term $\omega\tau << 1$ and the conductivity is purely real $\sigma_2 \approx 0$. For superconductors, the situation is different. The scattering time τ can be much larger due to the formation of Cooper pairs, leading to a very large value $\omega\tau >> 1$ even at microwave frequencies. The situation becomes opposite and while the real part $\sigma_1 \approx 0$ becomes negligible, the imaginary part σ_2 reads:

$$\sigma_2(\omega) \approx \frac{ne^2}{m^*\omega} \tag{2.26}$$

This imaginary parts is basically accounting for the intertial response of the Cooper pairs, which are responsible for the kinetic inductance effect. Overall the geometrical impedance of a stripline reads:

$$Z = R + j\omega L_k = \frac{l}{wt\sigma} = \frac{l}{wt}\left(\frac{\sigma_1 + j\sigma_2}{(\sigma_1^2 + \sigma_2^2)t}\right) \tag{2.27}$$

where l, w and t are the length, width and thickness of the stripline. After some algebraic manipulation, and neglecting the term $\sigma_1 \approx 0$, we can express the kinetic inductance as:

$$L_k \approx \frac{1}{\omega\sigma_2}\frac{l}{wt} = \frac{m^*}{ne^2}\frac{l}{wt} \tag{2.28}$$

Evaluation of the kinetic inductance is not a simple task, as it depends on several parameters that are not easy to measure or estimate. In general it must be done folllowing Mattis-Bardeen theory [33], which describes the complex conductivity of superconductors in the framework of BCS theory. A much simpler approach is the one proposed by Zmuidzinas [34], which works in the approximation of very low temperatures $T << T_c$ which implies a superconducting gap of $\Delta = 1.76k_BT_c$ and frequencies much lower than the superconducting gap $\hbar\omega << \Delta$. In this case, the Mattis Bardeen integral can be simplified and the imaginary part of the conductivity reads:

$$\sigma_2(\omega) \approx \frac{K_bT_c}{0.18h\rho_n}\frac{1}{f} \tag{2.29}$$

where ρ_n is the normal state resistivity of the superconductor, k_B the Boltzmann constant, T_c is its critical temperature and $f = \dfrac{\omega}{2\pi}$ is the frequency in hertz.

This formula allows for a quick estimation of the kinetic inductance, which can be used to have an idea of its impact on the resonator's performance. It can be used directly for L_k evaluation in microstrip lines. But, in the case of more complex geometries, it is necessary to use the FEM analysis imposing the complex conductivity value to the domain of the superconductor material. Another approach

of some FEM simulators(e.g. Sonnet) is to impose a surface inductance L_k to the surface of the superconductor, which is defined as:

$$L_k = \frac{l}{wt}\frac{0.18h\rho_n}{K_b T_c}[nH/cm^2] \tag{2.30}$$

in any case this value is substitued in the formula for the complex conductivity, which is then used in the wave equation, similarly to other simulators.

2.4.3 Simulation setup with COMSOL Multiphysics

COMSOL Multiphysics is a powerful finite element analysis (FEA) and multiphysics simulation softwar used for modeling and solving engineering, physics, and scientific problems. It allows users to simulate coupled physical phenomena—such as heat transfer, fluid flow, structural mechanics, electromagnetics, acoustics, and chemical reactions—within a single, integrated environment. COMSOL is widely used in research, product design, and process optimization across industries including aerospace, energy, electronics, biomedical engineering, and materials science. The software's modular structure enables customization through add-on modules (e.g. RF analysis, AC/DC, Heat transfer, Structural Mechanics and so on) and seamless integration with tools like JAVA, MATLAB and CAD software.

During this thesis project it served as a FEM simulation software for:

- Eigenmodes study of the resonator structure
- Frequency sweep with s-parameters plot when coupled to a feedline
- Electrostatics simulation for capacitance matrix
- Magnetic stray fields for measurements in the dilution refrigerator

In this subsection we can take a look to the several steps needed to setup a simulation inside the COMSOL environment, by following the simulation performed to one of the devices. This simulation has to find the resonance frequency of the resonator and perform a frequency sweep through the ports connected to the feedline and visualize the s-parameters verifying the correct coupling and quality factor.

Geometry drawing

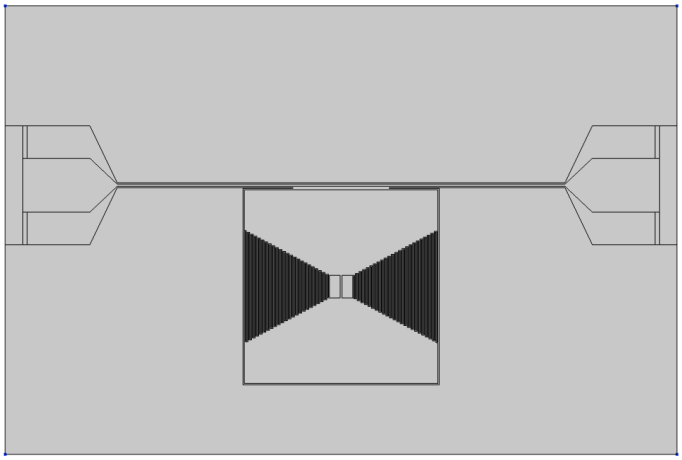

Figure 2.4: Drawing of the resonator structure in COMSOL.

In each types of simulation the starting point is the definition of the space occupation of the system. In particular when simulating electronic components, we must define a substrate, usually represented with a box with the dimensions of the full chip and the thickness of the substrate we are going to use. Then, the different layer corresponding to the different materials used in the fabrication process must be patterned, usually using a 2D drawing which is then extruded or cut into another domain. Finally the electronic components are then exposed to air or vacuum, so a bigger box will include the overall chip. When simulating superconducting circuits, they usually consist of monolayer structures, so once the cad 2D file of the structure is imported an extrusion can be performed to create the superconducting domain.

In section 2.3.1 we saw how the planar design object of Qiskit Metal is imported as a geometric drawing into COMSOL. By default SQDMetal draws a substrate of $t_{Si} = 750\,\text{um}$ and a vacuum box of $t_{vac} = 500\,\text{um}$ above the substrate.

Then, at this interface a planar drawing of the design is made and the different regions(metallic/substrate) are patterned. No extrusion is performed and no thickness is given to the metal, in fact when simulating superconductors, one can just use the boundary as a Perfect Electric Conductor(PEC). This type of simulation is not suited for kinetic inductance simulations, where the thickness of the metal is a relevant factor and a finite value of the conductance is given to the material.

So, an extrusion of the plane has been performed using a parametric thickness and thus creating new domains representing the superconducting material. Also the parts of the planar drawing corresponding to the substrate has been extruded, they will represent the vacuum layer between different parts of the metals.

Materials

In the material tab is possible to assign materials to the different domains defined in the geometry section. It is possible to use materials present in the COMSOL library or define brand new ones. What is actually important is that the relevant parameters for the type of simulation performed are assigned to a value with proper units of measurements. For the RF module it is necessary to assign only three parameters: relative dielectric coefficient ϵ_r, relative magnetic permeability μ_r and conductivity σ.

Three materials have been used in this simulations:

- Vacuum as the space in which the chip is inserted
- Intrinsic Silicon for the substrate
- Superconductor, with no distinctions between Niobium or Aluminum, but with a variable conductivity

As explained in section 2.4.2, to take into account the effects of kinetic inductance the conductivity of the material must be fully imaginary and depend on the frequency as in equation 2.29, where the constant terms are grouped into a parameter $\alpha = \dfrac{K_b T_c}{0.18 h \rho_n}$, while the frequency is taken by the physics module during simulation. The conductivity of the superoconductor is finally defined as:

$$\sigma = \frac{-j\alpha}{f} \tag{2.31}$$

Summarizing the parameters used for the materials:

Material	ϵ_r	μ_r	σ
Vacuum	1	0	0
Silicon	11.45	0	0
Superconductor	1	0	$\frac{-j\alpha}{f}$

Table 2.1: Parameters of the materials used to setup the simulation in COMSOL

Physics

To setup the simulation it is necessary to import the relevant equations modeling physics to be solved by the simulator. In COMSOL several different physics and equations can be imported at the same time by means of the so called physics modules: for example to solve frequency dependent Maxwell's equation it is necessary to import the RF module, while another module is used for electrostatics or for heat transfer and so on.

Basically great part of the work is automatically done when importing the module. All the outer boundaries are treated as Perfect Electric Conductors(PEC), in order to confine the study to the geometry of the chip. Also superconducting boundaries must be set as a PEC. And finally by default the Ampere's law is set for each domain of the geometry. Two lumped ports regions must also be defined, they serve as the place in which the frequency excitation is applied when the frequency sweep is performed. These domains are placed on the substrate regions adjacent to the launchpad with a default value of impedance of the ports set to $Z = 50\,\Omega$.

Mesh

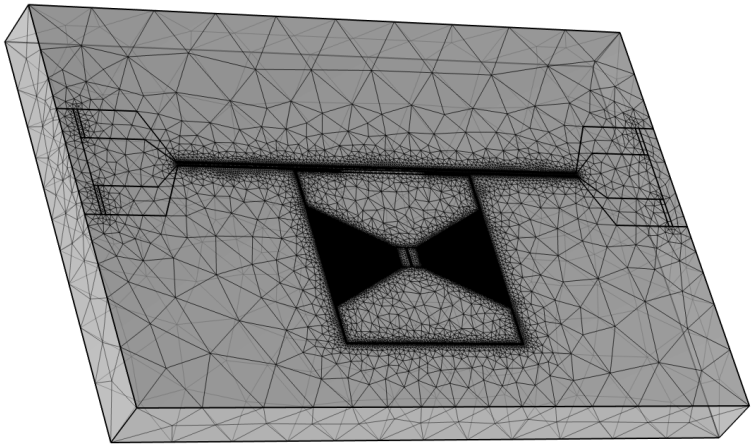

Figure 2.5: Mesh generation for the resonator structure in COMSOL.

The meshing process performs the discretization of the full geometry into smaller finite components. The equations are then solved with finite elements corresponding to those components that serve as approximation elements linearizing the solutions inside them. The refinement of the mesh is one of the most important step for the success of the simulation. As a general rule, having finer meshes makes the simulation much more precise and close to the real implementation of the simulated devices. But with too much discretized elements inside the domain, the required time to perform simulations can become very high. For this reason the mesh should be fine in tiny regions where particular attention must be taken, while it is better to maintain it wider in bulk regions where we expect that nothing important should happen.

Several algorithms exist in COMSOL to automatically perform meshing, which are also optimized for the specific physics being used. But also a high level of personalization is possible, with the possibility of defining the mesh sizes in specific

domains and also to sweep a mesh performed on a surface. Mesh parameters include:

- Minimum and maximum size of the single element
- Curvature factor: that expresses the rate at which the elements can grow when moving toward the region

In this case the different domains had very big differences in their dimensions. In fact, while the substrate and vacuum region had thicknesses of hundreads of micrometers, the superconducting material where from 180 nm for Niobium up to 10 nm for ultra thin Aluminum. These huge differences in the dimension did not allow the automatic mesh routine to find an acceptable solution. The mesh is then performed in a different way: at first the surface of the superconductor is meshed with triangles, here we wanted that the critical parts like the resonators were finely meshed, so we put very low maximum dimensions in order not to lose resolution. Then, the mesh is swept through the whole domain of the metal, with just one repetition, since the thickness is very low. And finally larger meshes are assigned to bulk regions of substrate and vacuum.

This method works better since the meshes on two adjacent domains must be compliant at their surface, and building a mesh from a pre-existing surface is easier and also allows for a finer control of the dimensions in different regions. Consider that for a full simulations on this devices, optimizing the mesh parameters, the solver needs at least 2 hours of run.

Studies

In the study section we define the type of parameter of the circuit we want to simulate. The study can be divided into different steps which can have different types: stationary studies, eigenmodes, frequency domain, parameters sweeps and others. In each step the relevant parameters for the study must be defined. Each solution steps gives also the possibility to choose for the solver algorithms to be used, and also gives the possibility to optimize the solver for the specific application if needed.

In the study for this resonators two steps are performed:

- Eigenmodes analysis: looks for the eigenmodes of the system which correspond to resonant frequencies of the components. A minimum value of frequency f_{min} and the number of eigenfrequencies must be assigned to the solver, in this way it will look for the first frequencies greater than f_{min}. Moreover, we are also using the frequency as a physical parameters in our materials, so we have

to guess where the eigenfrequency is, by assigning a linearization frequency f_{lin} in order to linearize the frequency values in that region and search for the resonance frequency f_{res} there. This step is iteratively repeated by slightly changing f_{lin} in order to approach the calculated f_{res}. When the two values are sufficiently near $|f_{res} - f_{lin}| < 200\,\text{MHz}$ we can take the final value f_{res} as a good approximation of the real frequency.

- Frequency sweep: once the resonance frequency value f_{res} is found, a sweep in frequency can be performed on the launchpads in order to retrieve the s-parameters in a specific frequency range of interest. In this case we set the range to be $f_{res} \pm 10\,\text{MHz}$, taking 600 points in frequency in total between the extremes.

Firstly, only the first step of the study was performed: in fact if the resonance frequency was not in the required range, the device design must be adjusted a priori. Then, when the value of f_{res} was acceptable, we could move on to the second step in order to evaluate the coupling and quality factor.

2.4.4 Results visualization and analysis

Vector fields

COMSOL stores the results in specific data structures, that for each saved value of the frequency have the full informations of disposition of vector fields and currents in the overall device.

For eigenmodes analysis, these values are saved only for the solution modes found, while for the frequency analysis they are stored for each point in frequency. It is possible to perform a single plane or a multiplane visualization of these fields, using heatmaps or arrows. This is particularly useful when we want to know how magnetic field places itself in the device. With them it is also possible to perform custom evaluation, for example by integrating on the electric field to find the current density traveling along a certain geometry.

For our spin based application, the visualization of the magnetic field can be very important, since we are interested in a better interaction with the ensemble.

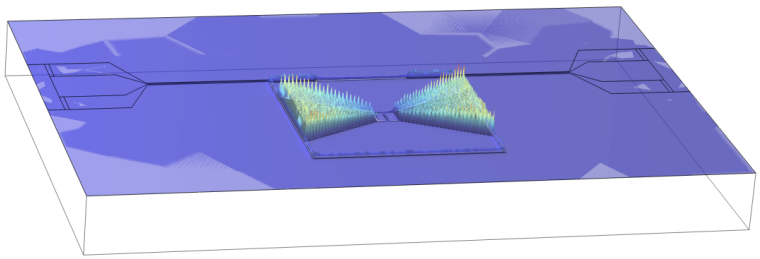

Figure 2.6: Electric field distribution in the CMSL device.

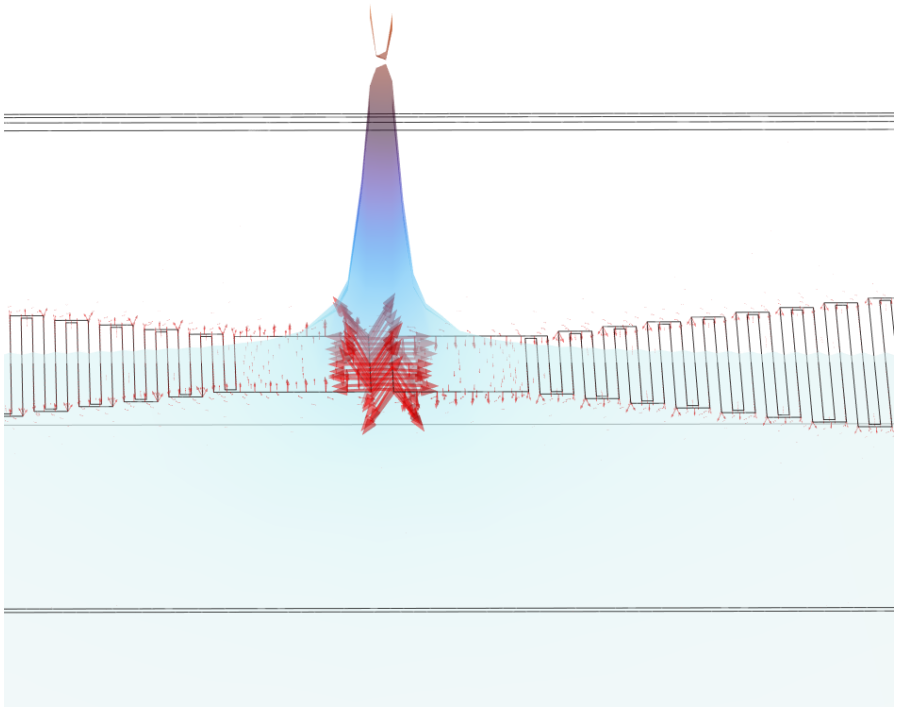

Figure 2.7: Magnetic field distribution in the CMSL device.

Scattering parameters

Scattering parameters, or S-parameters, describe how electrical signals behave in linear RF and microwave networks, especially under steady-state sinusoidal conditions. Instead of using voltages and currents directly, S-parameters express the relationship between incident and reflected power waves at each network port. Each element S_{ij} represents the ratio of the wave leaving port i to the wave incident on port j, with all other ports matched to their characteristic impedances. This formulation simplifies analysis of high-frequency systems where reflections, transmission, and impedance mismatches are significant. S-parameters are frequency-dependent and, in real measurements, are typically measured using a vector network analyzer (VNA). They provide insights into gain, loss, and reflection without requiring direct circuit access. In multiport systems, the complete S-matrix characterizes overall network behavior.

Starting from the geometric definition of the ports, the scattering parameters are directly calculated by integrating over the field distribution when a specific frequency is applied. These evaluations result in the usual scattering diagram and also the Smith chart, since we are using two ports one can choose what parameters to see, usually the evaluation has been performed with S_{11} and S_{21}. Internally the RF module is also able to evaluate the quality factor Q of the devices.

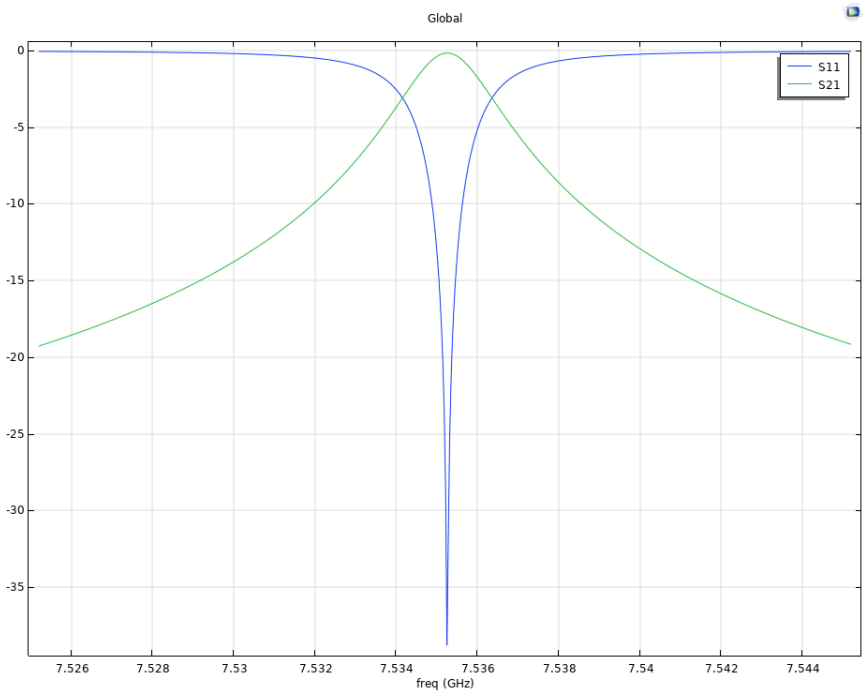

Figure 2.8: Scattering parameters for the CMSL device.

2.5 Final output

2.5.1 Final device layout

After several iterations of simulation and optimization, finally two different devices have been selected, for Phosphorus and Bismuth donors applications. Their characteristics are described by geometrical parameters which are taken as input to the Qiskit Metal custom QComponent class. In this way these devices can be redrawn in the same way each time the class is instantiated using those parameters. For simplicity the two designs have been named Phosphorus layout and Bismuth layout, their characteristics are reported in the following subsection.

Resulting layouts

For Phosphorous layout the target frequency was 5 GHz, a bit larger than the one used in Eichler's work, but this was to take into account some unwanted parasitic effects and the possible lowering of the resonance frequency due to the magnetic field.

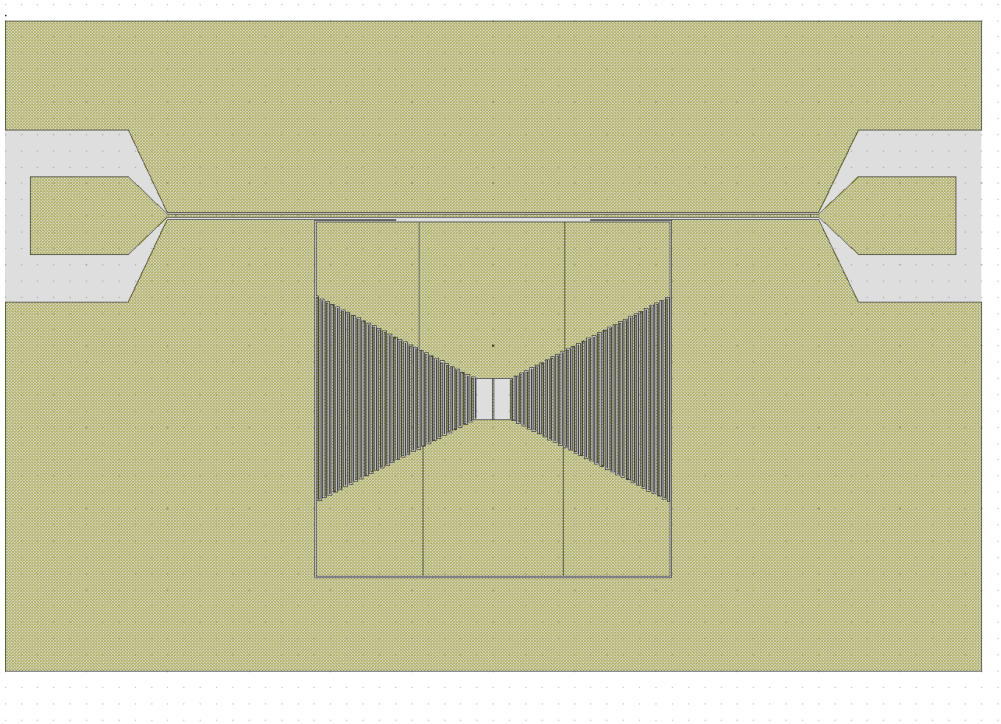

Figure 2.9: GDS 2D image of the Phosphorous device.

The simulated devices had the following relevant geometrical parameters:

- 60 fingers per side in the interdigitated capacitance
- 4 um of width of the fingers and 4 um of gap between them
- 125 um of inductor wire length
- 3 um of inductor wire width

Regarding Bismuth layout for the same reasons we targeted a frequency slightly higher with respect to the base hyperfine clock transition at around 7.5 GHz.

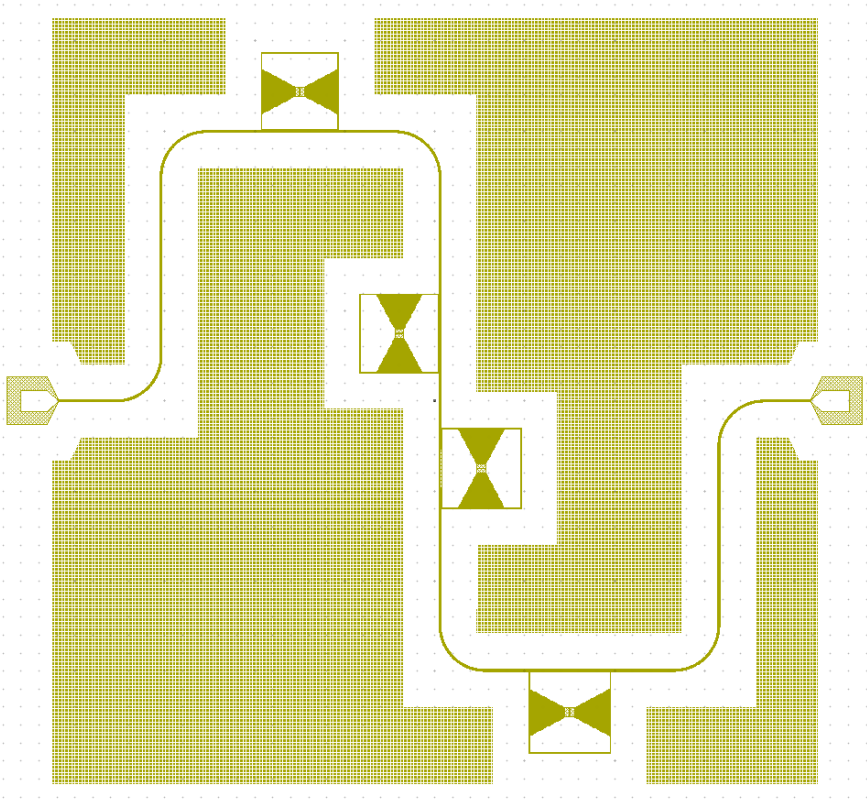

Figure 2.10: GDS 2D image of the Bismuth devices on the final full chip layout.

Similarly, the resulting geometrical parameters are reported:

- 47 fingers per side in the interdigitated capacitance
- 4 um of width of the fingers and 4 um of gap between them
- 100 um of inductor wire length
- 8 um of inductor wire width

These geometries has been simulated in frequency domain, but also in electrostatics, in order to derive the capacitance matrix and thus the impedance of the resonator. Here it's possible to find a summary of the parameters of these geometries:

Parameter	Phosphorous	Bismuth
$f_{res}[GHz]$	5.0708	7.4742
$C_{sim}[pF]$	6.3428	3.9517
$L_r[nH]$	0.155	0.115
$Z_0[\Omega]$	7.195	3.787

Table 2.2: Simulated resulting parameters for each type of resonator

With these satisfying results, it is possible to start preparing the lithography on full wafer.

Feedline coupling

After targeting the required resonance frequency, also the optimal coupling has been studied. Two different types of coupling have been taken into consideration: the first was a normal large gap between the resonator and the feedline, while the second has a thin layer of metal on the two sides. By simulating the two couplings using frequency sweep, it came out that the first solution was basically uncoupled, in fact it resulted in a big quality factor but basically absent absorption in the s-parameters. While the second one exhibited lower quality factors, in the order of 3000, but with a proper scattering profile.

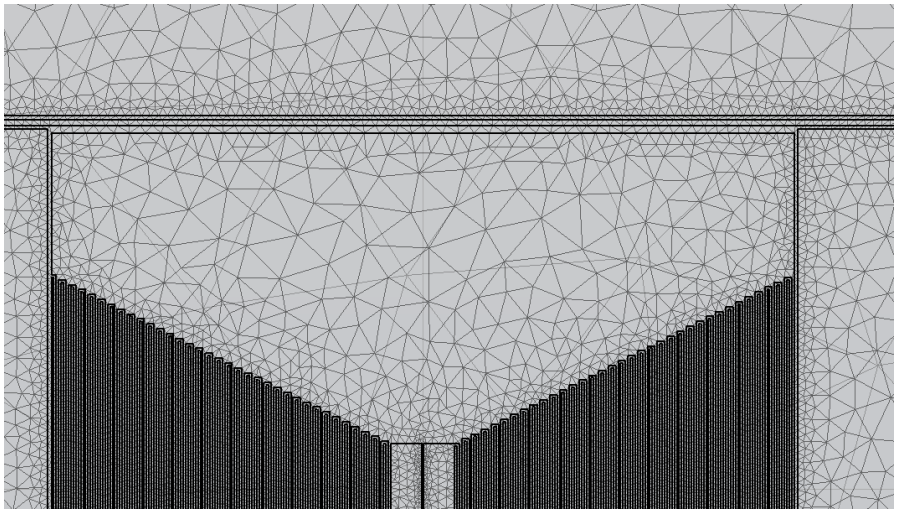

Figure 2.11: Image of the gap coupling.

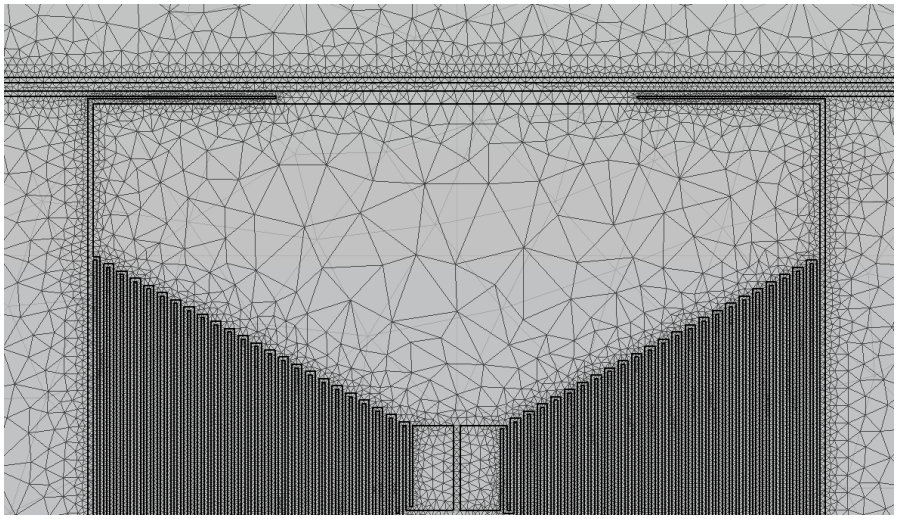

Figure 2.12: Image of the interleaved coupling.

2.5.2 Lithography preparation

Once the structure of the single resonators is defined, the next step is to prepare the full chips to be fabricated, and also the disposition of the chip onto the wafer available. Moreover, several different considerations must be taken into account, like: vortex pinners, dicing of single dies and the bonding process. This part of the design process will provide as output one or several drawings, under the form of GDS II files, which will be used during direct writing onto the photoresist.

Dies patterning

The footprint occupied by a single resonator is of about $1\,\mathrm{mm}^2$, while the overall dimension of the chip is of $1\,\mathrm{cm}^2$. There is plenty of room for inserting several resonators on the very same chip. The idea then, was that since we are able to accomodate 12 dies on the same wafer, we could provide 12 versions with different configurations and dispositions of the resonators. Since the first fabrication is for testing of the devices we allowed also mixed configurations, in which Phosphorous and Bismuth layouts are both present on the very same chip. The only requirements were that two resonators must be placed far from each other in order to avoid cross-talking, but also that the resonant frequencies should have been maintained far, to allow the distinction of resonances.

I decided to accomodate on a single chip maximum for per each type of resonator, this empirically looked like the maximum number for maintaining a satisfactory minimum distance. In order to have a certain spacing between resonant frequency,

I noted that by adding one finger per side in the capacitor, the frequency increased by about $\Delta f \approx 200\,\text{MHz}$. So, from the base resonators seen in section 2.5.1, I added one finger for each of the successive resonators in the design, spanning a range of around 600 MHz.

Vortex pinners

In superconducting circuits, vortex pinning is essential to maintain stable and lossless operation under the influence of external magnetic fields or transport currents. When a type-II superconductor is exposed to such conditions, quantized magnetic flux lines, known as vortices, can penetrate the material. The motion of these vortices under Lorentz forces generates dissipation, introducing unwanted noise and reducing the quality factor of superconducting devices. Vortex pinners—engineered defects or nanostructures that locally trap vortices—are introduced to immobilize these flux lines and suppress energy loss. Effective pinning ensures that vortices remain fixed even in high-current or varying-field environments, thus preserving the circuit's superconducting state. In applications such as superconducting qubits, resonators, and quantum interference devices, minimizing vortex motion is crucial for achieving high coherence and stability.

The most pinners are present, the better they can work to capture the vortices. On the other hand the surface of the ground plane should be as uniform as possible to allow a good electrical contact. Lowering the dimension of the pinners and taking them away from the devices is the best solution for both the problems. Unfortunately too low dimensions are very difficult to be fabricated, and the risk is that some pieces of overdeveloped resist detach and ruin the yield of the lithography. Moreover if the pinners are far away from the device they become useless as they are not protecting them from the vortices. All these factors must be taken into consideration when designing vortex pinners.

As vortex pinners we used an array of little square holes on the ground region with dimensions $5 \times 5\mu m^2$ and a gap of 9 µm between them. A space of 400 µm is left near the components of the circuit to allow the ground to be electrically uniform.

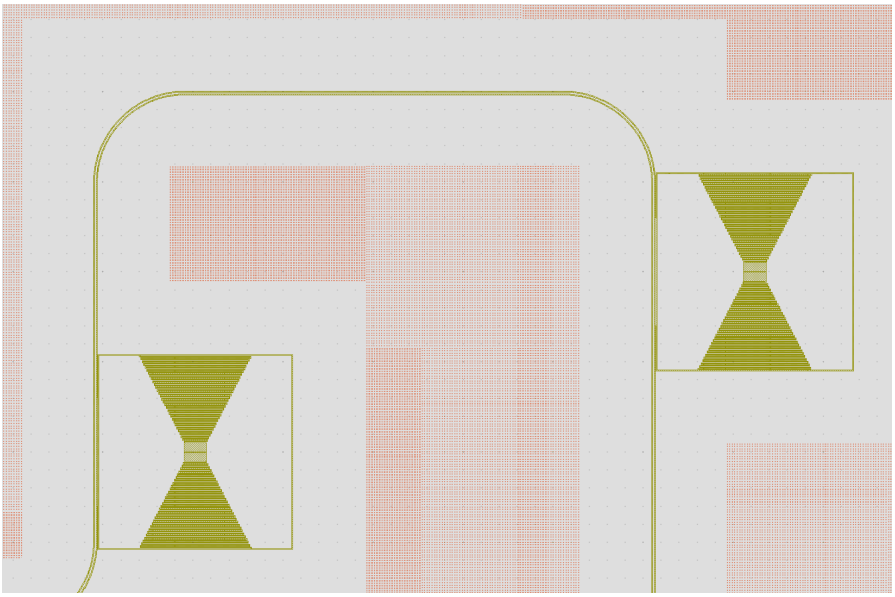

Figure 2.13: Image of the vortex pinners(the little dots in red) around the main structure.

Bonding pads

As a last adjustment we had to consider the fact that we were going to design an ultrathin film of Aluminum. The very small thickness $t_{Al} \approx 10\,\text{nm}$ makes it very fragile when touched, and it must be treated with particular attention. But, unavoidably the film has to be bonded to the circuit before measurements, and this process can risk to detach the ultrathin film and basically break the device.

To solve this issue the idea was to interpose a pattern of circles on the edges of the dies. This circles are to be made with depositions of Titanium and Gold, this should allow to guarantee the electrical contacts and the adhesion of the film during the bonding process. These pattern has been drawed and inserted as the first lithographic step to be performed before the actual deposition of Aluminum.

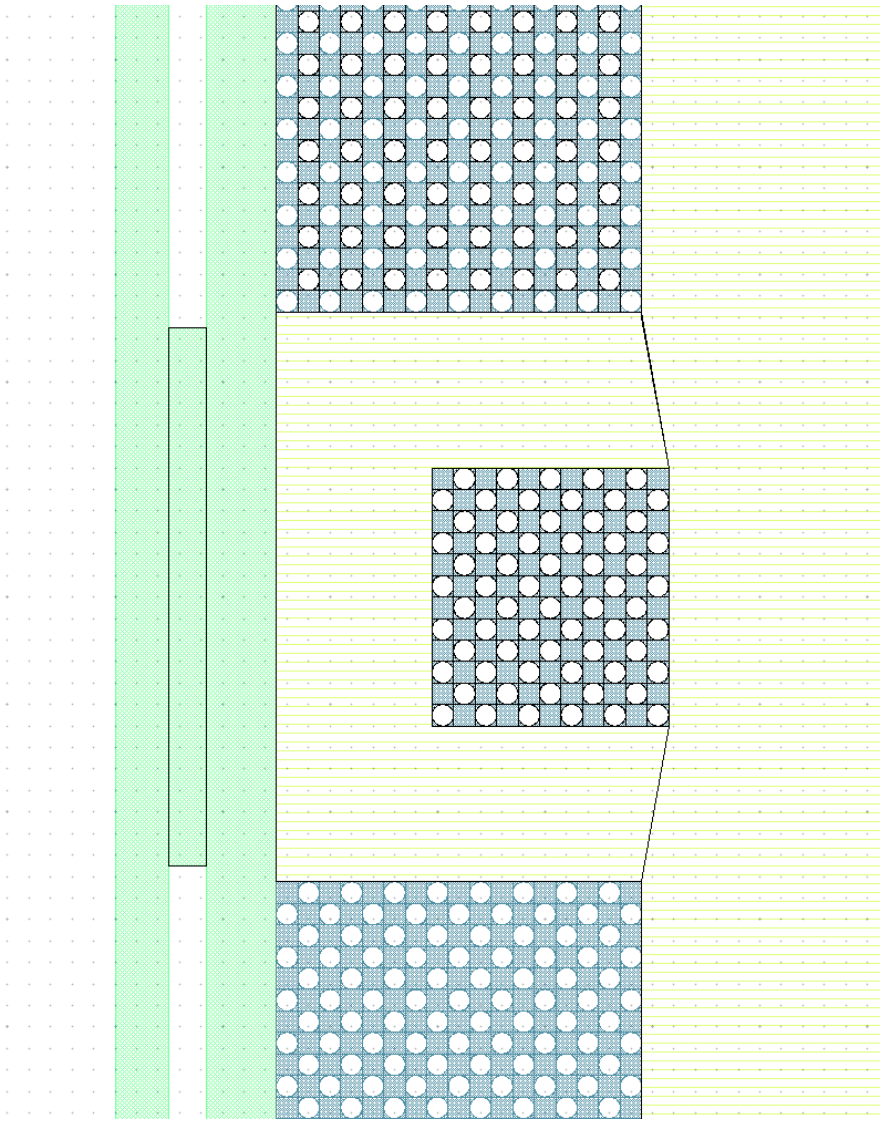

Figure 2.14: Image of the bonding pads: the little circles array patterned in white. Present on the whole contour of the dies.

Chapter 3

Fabrication

The designed devices have been fabricated in the PiQuET cleanroom facility, inside the INRiM campus. This chapter contains all the fabrication principles used in this part of the work, the available instrumentation and its theoretical background is explained and the fabrication recipe is reported for completeness. Finally, characterization of the fabricated device has been performed in order to evaluate the possibility of using them for measurements in the dilution refrigerator.

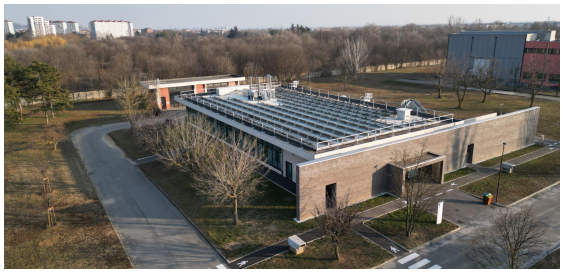

Figure 3.1: Image of the PiQuET cleanroom facility.

Fabrication processes are based mostly on the expertise of the personnel and on availability of instrumentation and materials. Some processes might result dangerous, too expensive or simply not optimized, and thus bringing an high level of uncertainty in the process itself. This fabrication process lasted more than two weeks because of some imperfection in the resist which unexpectedly degradated very quickly.

Overall this fabrication process is simple, since the types of devices considered does not have very low critical dimensions, narrow patterns or particular features. Moreover, the project involves only two lithographic processes, that can be reduced

to one in case of a superconductor with higher thickness.

After lithography patterning and development the metals were deposited using an e-beam evaporator. To allow for lift-off we needed the sidewalls of resist to be negative, so the main idea behind the fabrication process is to use the image-reversal techniques in both lithographic steps.

3.1 Methods

This section exposes the materials and methods used for the fabrication of the devices. And the precise description of the fabrication recipe is reported for complete replication of the work.

3.1.1 Materials

With materials we refer to all the chemicals and substrates used in the fabrication process. Except for substrates they mainly consist on organic polymers and their various solvents for the different photolithographic steps, the deposited metals are not discussed here.

Substrate

The substrate is the starting base on which the devices are fabricated. They usually consist of a wafer of a certain material, with a certain orientation and thickness. They are used as mechanical support for the devices and can also have an active role in the device operation due to their electrical and thermal properties. The characteristics of the substrate are crucial for the fabrication process, since they can affect the adhesion of the resist and the metals, the uniformity of the coating and the final quality of the devices. Important parameters listed in the description of the substrate are:

- Material/s of the wafer (e.g. Si, GaAs, Sapphire, SiO2 on Si etc.)
- Crystallographic orientation of the lattice (e.g. for Si (100), (110), (111), etc.)
- Doping type of the wafer (e.g. n-type, p-type, intrinsic) and dopant (e.g. Phosphorus, Boron, etc.)
- Diameter (e.g. 2 inch, 4 inch, 6 inch, etc.)
- Thickness (e.g. 500 µm, 1 mm, etc.)
- Substrate resistivity (e.g. low, medium, high)

- Method of production (e.g. Czochralski, Float Zone)
- Surface finish (e.g. single or double side polished, etched, etc.)

Generally speaking the most used substrate is Silicon [35], due to its low cost, availability and good thermal and electrical properties. In superconducting quantum electronics the type of substrate is crucial, as it introduces the most part of the losses in the systems. A very pure substrate is needed with the absence of external two-level systems (TLS) that can interact with the qubits and resonators, absorbing energy. For this reason high resistivity intrinsic silicon is usually preferred [36], with a resistivity higher than $10\,\mathrm{k}\Omega \times \mathrm{cm}$. It is also unusual, unless required by a specific application, to make use of substrates with Silicon oxide layers or with heavy doping, as they, again, introduce defects and TLS.

In our final application the substrate is covering a fundamental role. In fact, the Silicon lattice is hosting the implanted Phosphorus or Bismuth donors that create the spin ensemble. The implantation does not take place in normal Silicon grown with usual crystallographic techniques, because it is needed to remove the most part of ^{29}Si present.

^{28}Si is spinless (I = 0), whereas ^{29}Si has nuclear spin I = 1/2. In spin ensembles, ^{29}Si nuclei create a hyperfine-coupled bath that generates quasi-static Overhauser fields and nuclear flip-flops [37], leading to inhomogeneous broadening (shorter T2*) and spectral diffusion (limiting T2). Isotopically enriched ^{28}Si suppresses this bath, producing much narrower ESR linewidths and significantly longer coherence; residual decoherence is then set by impurities, electron-electron dipolar interactions, strain, and charge noise. For collective coupling, the reduced inhomogeneous width in ^{28}Si increases the mutually resonant spin fraction, enhancing ensemble cooperativity and access to strong-coupling regimes. ^{29}Si is advantageous mainly when the nuclear spins themselves are the intended resource, at the cost of broader lines and shorter coherence.

So, in conclusion it is necessary to use isotopically enriched ^{28}Si substrates, with a residual concentration of ^{29}Si lower than $\approx 1{,}000\,\mathrm{ppm}$. The available substrates with these characteristics are built with an epitaxial layer of enriched ^{28}Si on top of a classical intrinsic Si wafer [38]. Into this epitaxial layers we can implant the donors at a certain depth and anneal to activate them.

The work performed in this thesis is reporting the devices used for testing before building the final quantum memories. For this reason, and for the high cost of the enriched substrates, we did not use the very same substrates that will be employed in the final devices. The substrates used are intrinsic high resistivity ($\rangle 10\,\mathrm{k}\Omega\mathrm{cm}$)

Si $< 100 >$ 2 inch wafers, with a thickness of 500 um and double side polished. To achieve such high resistivity the wafers are grown with the Float Zone technique [39], that allows to reach very low impurity levels. This types of substrates should not introduce high losses in the resonators, they are not mimicking the exact conditions of the final devices, but they are good enough for testing purposes.

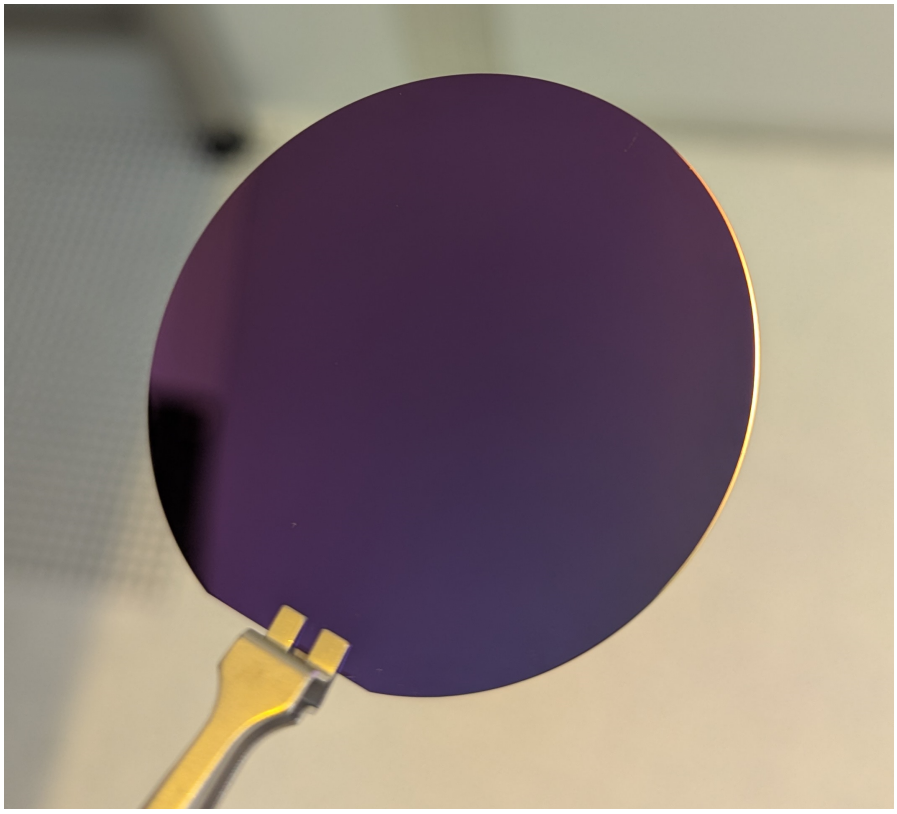

Figure 3.2: Image of the intrinsic Si wafers used for fabrication.

Photoresist: AZ5214E

Photolithography is the most used technique in microfabrication for patterning micro and nano structures on a substrate [40]. It is based on the use of a photosensitive polymer, called photoresist [41], that changes its solubility in a certain solvent when exposed to electromagnetic radiation of a certain wavelength.

To perform the lithographic process the photoresist is spin-coated on the substrate, creating a thin and uniform layer of some micrometers in thickness performing adhesion to the substrate. Once the coating is performed the patterning takes place by means of EM light exposure at a certain wavelength. In industrial processes

the exposure is performed by means of a photomask, that is a transparent plate with an opaque pattern, usually made of Chromium, on it. The photomask is interposed between the light source and the resist, so that only the exposed areas receive the radiation and undergo a chemical change that changes their solubility in the developer solution.

In this work, due to the possible changes in the design of the devices, we used a maskless lithography system, that directly exposes the resist by scanning a laser beam on it. This technique is more flexible and faster for prototyping, but it has a lower throughput compared to mask lithography. In particular we made use of a UV laser writer [42], explained more in detail in the instrumentation section 3.1.2.

Photoresists are characterized by several parameters to be taken into account when selecting them for the fabrication process:

- Positive, negative or image-reversal resists: determines if the exposed areas become more soluble (positive), less soluble (negative) or if a further baking step is needed to invert the solubility (image-reversal).
- Wavelength of exposure: determines the sensitivity of the resist to a certain wavelength
- Chemical amplification: determines if the resist undergoes a chemical reaction that amplifies the effect of the exposure, allowing for lower doses, higher resolution and different effects in the process.

The final choice for this work fell on AZ5214E [43], a positive resist that can be used as an image-reversal one [44]. The chemical composition of AZ5214E is based on a novolak resin, that is a phenol-formaldehyde polymer, mixed with a diazonaphthoquinone (DNQ) photoactive compound (PAC). The presence of DNQ decreases the development rate the polymer [45], but when exposed to UV light it undergoes photolisis and its anti-oxidation effects disappear.

Image reversal effects are activated by a baking step, which makes the activate the cross-linking agents in the exposed areas, making them very unsoluble on specific developers. The whole photoresist is then exposed again to UV light to make the unexposed areas soluble with the same mechanism of normal exposure. Now the solubility in the developer is inverted, and the resist can be developed.

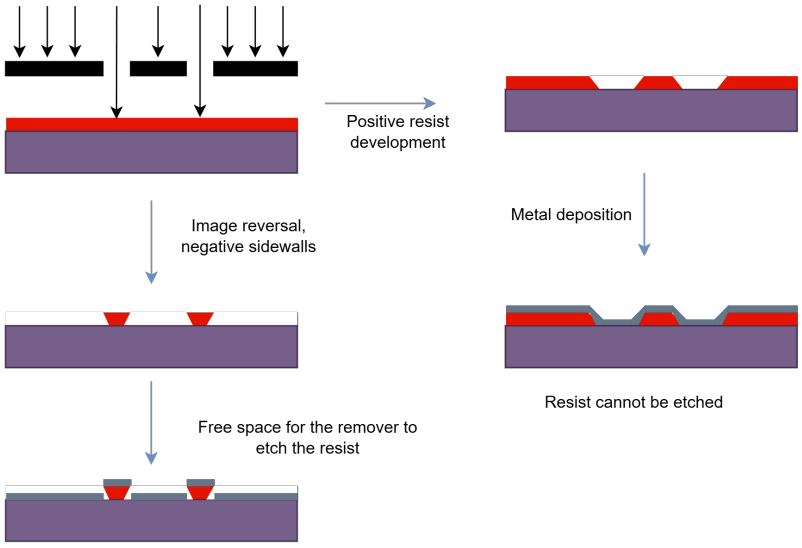

Figure 3.3: Schematic of the image-reversal process.

The two main reasons for this choice are the compatibility with the laser writing systems and the possibility to use it as an image-reversal resist. This last feature is crucial for the fabrication process, since it allows to create negative sidewalls in the resist, that are needed for a successful lift-off. Positive resists in fact, tends to create an overcut in the sidewalls of the unexposed resist, if metals are deposited on them they create a continuous film that cannot be lifted-off. By performing image-reversal process after exposure, the unexposed polymer becomes more soluble than the exposed one, and the sidewalls of the resist become negative, allowing for a clean lift-off.

Developer: AZ 351B 1:4

The developer is the chemical solution used to dissolve the more soluble areas of the resist after exposure. For a specific photoresist a specific developer is needed, since the chemical composition of the resist determines its solubility in different solvents. And thus some calibrated processes can be performed.

AZ 351B is a commercial developer for AZ series photoresists, compatible with most of the AZ resists. It is able to deliver high contrast and optimal walls profiles, making it suitable for this types of applications. It is an inorganic, aqueous, alkaline solution typically sold as a concentrate to be diluted with DI water, with a 1:4

proportion in this case.

Remover

In order to remove the resist after the fabrication process a specific remover is needed. The remover is a chemical solution able to dissolve the resist without damaging the substrate or the deposited metals. The choice of the remover depends on several factors like: substrate compatibility, resist type, metals deposited, process temperature and safety.

The indicated remover for this resist is AZ 100 remover, a commercial product dedicated to the removal of AZ series resists. Although this indication we found out that at least for this specific process regular acetone was more effective and efficient. Removing processes may also be performed heating up the solution or in an ultrasonic bath, to improve the efficiency of the process.

Coating: PMMA 950K A9

The coating is a protective layer deposited on the devices after fabrication, to protect them from mechanical damage and contamination. When the process is completed dicing is performed to separate the wafer in single dies, that can be mounted on a chip carrier for measurements. Dicing is a mechanical process that can introduce cracks and damages on the devices, so a protective layer is needed to avoid this. Coating is performed by means of a polymeric layer, that can be removed before using the devices or can be left on them if it does not interfere with their operation.

In this work we used PMMA 950K A9, a commercial polymethyl methacrylate (PMMA) solution in anisole, with a molecular weight of 950K and a dilution of 9%. It is a very common resist, usually employed in electron beam lithography, which is highly resistant to mechanical stress and can be easily removed with acetone if needed.

3.1.2 Instrumentation

This section describes the main instrumentation available in the PiQuET facility used in the fabrication process. The quality of the fabricated devices strongly depends on the quality and calibration of the instruments, so it is important to understand their working principles and limitations. Differences in calibration lead to different results, so it is important to report the exact instruments used for the fabrication process.

Spinner

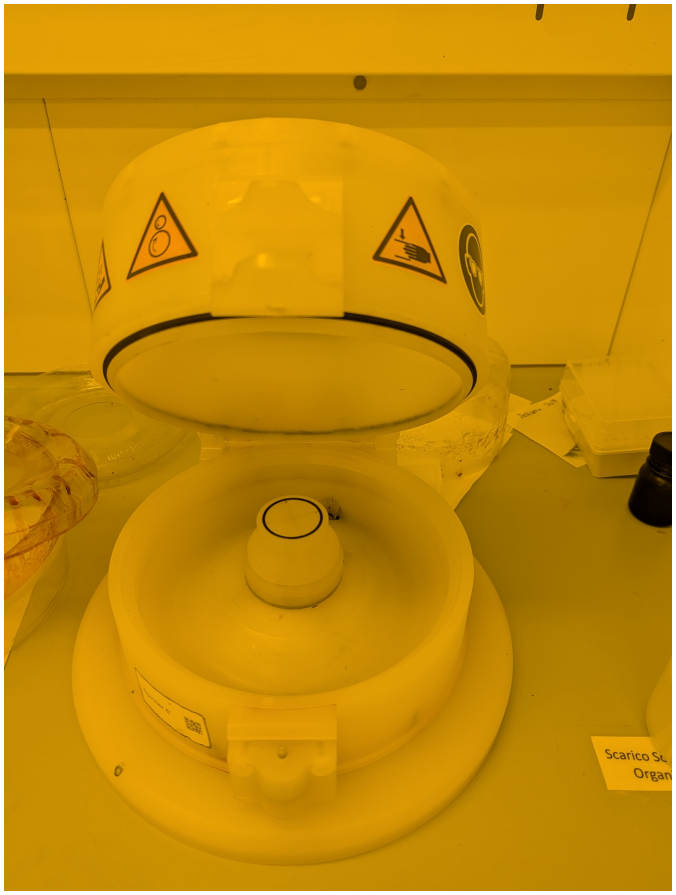

Figure 3.4: Image of the Polos Spin 150i spinner.

Spin coating is the most used technique to deposit thin and uniform layers of photoresist on a flat surface. It is extensively used in microfabrication for its quality, simplicity, low cost and high throughput. The main application for microelectronics is the deposition of photoresist on wafers for lithographic processes, but it can be used for other applications like coating of polymers, sol-gels, nanoparticles and biological samples.

It is based on the centrifugal force generated by a rotating substrate, that spreads the resist on the surface and creates a thin film. A specific amount of resist is deposited on the center of the substrate, that is then rotated at high speed (from few hundreds to several thousands of rpm) for a specific time. The centrifugal forces allow the resist to have a uniform and precise thickness on the whole surface, allowing the repeatibility of the process. The final thickness of the resist depends

on several parameters: spin speed, acceleration, spin time, resist viscosity and solvent evaporation rate.

The spinner available in the PiQuET facility is a Polos Spin 150i, that comes with a vacuum chuck of different sizes to hold the wafer in place during the spinning. Once the wafer is placed in the center of the chuck, vacuum is applied to hold it in place and the resist is deposited on the center of the wafer. The spinner is then started with a specific recipe that sets the acceleration, spin speed and time. The recipe is customly calibrated by the user and saved for future use. It is possible to personalize it for different types of wafers and resists. It usually consists of a first step at low speed (e.g. 500 rpm) for few seconds (e.g. 5 s) to spread the resist on the whole surface, followed by a second step at high speed (e.g. 4000 rpm) for a longer time (e.g. 30 s) to achieve the desired thickness and remove the edgebeads that tend to create during the first spin.

Laser writer

The lithographic process is performed by means of a Heidelberg µpg laser writer, that is a maskless lithography system able to expose the resist by scanning a laser beam on it. The laser is focused with high precision on the resist, allowing for high resolution patterning. If needed it is also possible to choose the amount of energy delivered to the resist, the so called dose, by changing the power of the laser and the speed of the scan.

Once the wafer is loaded into the system, the pattern to be exposed is sent from a computer connected to the laser writer. The pattern is usually designed with a CAD software and then converted in a format compatible with the instrument. The system is then calibrated by the user, which delivers the center, orientation and dimensions of the wafer, to focus the laser on the resist and the exposure is started.

These types of processes are usually slow, since the laser has to scan the whole surface of the wafer. The time required to expose a 2" wafer with the design patterned by us requires around 7 hours, which basically means that this process is performed overnight.

UV exposure system

In order to perform the image-reversal process a flood UV exposure system is needed. These systems are able to expose the whole surface of the wafer at once, allowing for a fast and uniform exposure. They are usually based on a mercury or LED lamp emitting at a certain wavelength, with a collimated beam that uniformly

exposes the surface. They are very useful for high throughput lithographic processes and for processes like image-reversal or dices detachment from dicing tapes.

The UV-EXPR150R is a commercial flood UV exposure system available in the PiQuET facility. It basically consists of a box with a UV lamp inside, and a proctective lid that can be opened to insert the wafer. The controller allows to set the exposure or dose, and the lamp can be turned on for a certain time to deliver the desired dose. The lamp consists of an high power diode that emits at a wavelength of 365 nm, combined with homogenization optics to deliver a uniform illumination on the whole surface.

E-beam evaporator

Physical vapor deposition (PVD) is a technique used to deposit thin films of materials on a substrate by means of physical processes like evaporation or sputtering. The vapor sticks physically to the substrate creating a thin film with a thickness that can be controlled by the user. A commonly used PVD technique is e-beam evaporation, that consists in the use of an electron beam to heat up a target material until it evaporates.

In a vacuum chamber a filament is heated up to let it emit electrons by thermionic emission. Using a magnetic field, the electrons are accellerated toward the target material, placed inside a crucible. By hitting the target, electrons dissipate their kinetic energy heating it up until it starts to evaporate. The evaporated material ballistically travels towards the substrate, placed upside down above the target, and condensates on it creating a thin film. The high vacuum in the chamber is important to avoid contaminations of the material reacting with air.

For the deposition of the metals needed for our devices we used a Temescal FC-2000 e-gun evaporator. It is available in the PiQuET facility and it is able to deposit a wide range of materials with high purity and good control of the thickness. The system is equipped with a quartz crystal microbalance (QCM) that allows to monitor the thickness of the deposited film in real time [46], allowing for a precise control of the process. The system is also equipped with a rotating sample holder, that allows to deposit the material uniformly on the whole surface of the wafer. The main feature of it is the presence of a cryogenic pump, by means of liquid nitrogen it creates a cold trap that allows to reach very high vacuum levels (up to 10^{-8} mbar) in a short time, allowing for high purity depositions. The machine was used both for the deposition of the bonding pads (Ti/Au) and for the superconductor (Al). As we will see in the characterization section 3.2.2, the control of the Al thickness was quite precise but to be calibrated since at that high

rate it tends to overshoot the desired thickness.

3.1.3 Fabrication recipe

The fabrication recipe is reported here for completeness and to allow for replication of the process. Overall the process consists of 2 lithographic steps, of metal deposition and lift-off.

Resist coating

Instruments:

- Photoresist: AZ5214E
- Hot plate
- Wafer: i-Si, 2", 275um thick, <100> oriented, high resistivity, double polished
- Spinner: Spin polos 150i

Process:

- An outbake is performed on the wafer at 180°C for 5 min to remove moisture from the surface
- The wafer is placed on the spinner chuck and vacuum is applied to hold it in place
- 1.5 mL of AZ5214E are dispensed using a proper syringe on the center of the wafer
- The specific spinning recipe is started: 500 rpm for 5 s, followed by 4,000 rpm for 30 s.
- The wafer is then baked on a hot plate at 110 °C for 60 s to remove the solvent and harden the resist, this process is called soft bake.

1st Lithography

The only instrument needed for this step is the Heidelberg µpg laser writer, described in section 3.1.2. Process:

- The wafer is physically loaded into the laser writer
- The pattern to be exposed is sent from a computer connected to the laser writer

- The system is calibrated by the user, which delivers the center, orientation and dimensions of the wafer, to focus the laser on the resist
- The exposure is started

Overall this process takes around 7 hours to be completed.

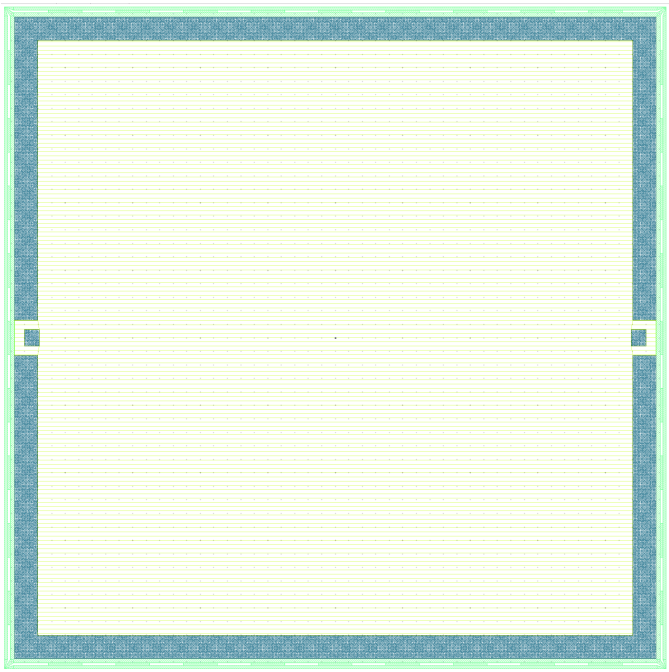

Figure 3.5: Image of the mask used in the 1st lithography step, the only unexposed areas is the pattern of little dots all around the die, in the blue area.

Image reversal

Instruments:

- UV exposure system: UV-EXPR150R
- Hot plate

Process:

- The wafer is baked on a hot plate at 120 °C for 2 min to activate the image-reversal process
- The wafer is exposed to UV light in the flood exposure system for 10 s, at wavelength 365 nm to deliver a dose of 200 mJ cm^{-2} with an irradiance of 20 mW cm^{-2}

1st Development

The development process is very delicate and few seconds of difference in immersion time can compromise the whole process. We tried to not exceed with time, in this way we could recover from underdevelopment, that is usually less critical than overdevelopment. Since it is possible to submerge again the wafer in the developer in that case. Also stirring is very important to have a uniform development on the whole surface. But, the difference types of stirring techniques (magnetic, manual, ultrasonic) can lead to sensibly different development timings.

Instruments:

- Developer: AZ 726 MIF
- De-Ionized water
- Beaker with magnetic stirrer
- Nitrogen gun
- Timer

Process:

- A good amount of developer is poured in a beaker and stirred with a magnetic stirrer
- The wafer is submerged in the developer for $\approx 3\,\text{min}$, until the unexposed looks are completely removed
- The wafer is very quickly rinsed with DI water to stop the development process in a different beaker
- The wafer is dried with a nitrogen gun
- An inspection is performed with an optical microscope, explained in section 3.2.1, to check the quality of the development
- If underdevelopment is noticed the wafer can be submerged again in the developer for few seconds

Ti/Au deposition

Instruments:

- E-beam evaporator: Temescal FC-2000

- Tape for wafer handling

The temescal evaporator described in the instrumentation section 3.1.2, is a very user friendly machine used for industrial processes. It is possible to load a recipe with the desired parameters: thickness, deposition rate and start the deposition. Since it has a rotating sample holder for 4" wafer, its necessary to use one of them as support for our 2" wafer, which is taken in place with a proper cleanroom tape.

Process:

- The wafer is loaded into the evaporator, with a proper tape to hold it in place
- The chamber is pumped down for a whole weekend up to a pressure of $\approx 10^{-8} mbar$
- Once the desired vacuum is reached the deposition is started by starting the proper recipe with the needed parameters
- The recipe consists in the deposition of 5 nm of Ti and 50 nm of Au
- Once the deposition is completed the chamber is vented with dry nitrogen and the wafer is unloaded

1st liftoff

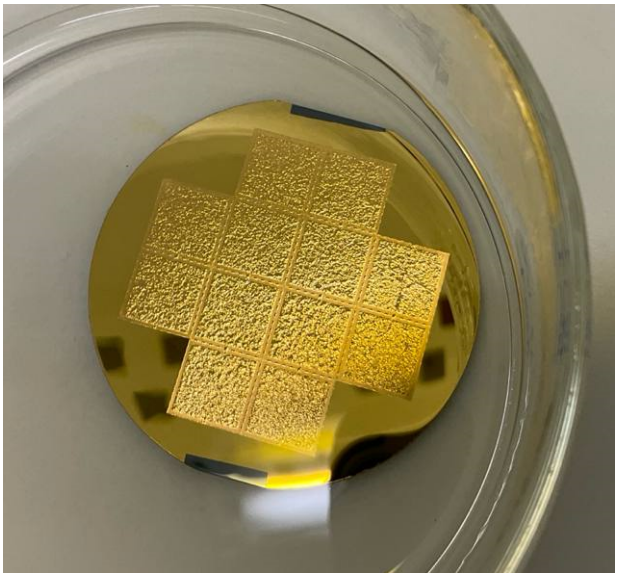

Figure 3.6: Image of the lift off step ongoing.

Instruments:

- Remover: AZ100 and/or Acetone
- Isopropanol (IPA)
- Hot plate

A complete lift-off process has an high variability of timings, since it depends on several factors: resist thickness, metals deposited, and mostly the geometrical composition of the patterned layer. In general, to enhance the efficiency of the process, it is possible to heat up the remover and/or to use an ultrasonic bath. The main important thing is to avoid the drying of the remover on the wafer, since detached pieces of metal can then attach directly to the substrate and become difficult to remove. So, particular attention is needed in the rinsing and drying steps.

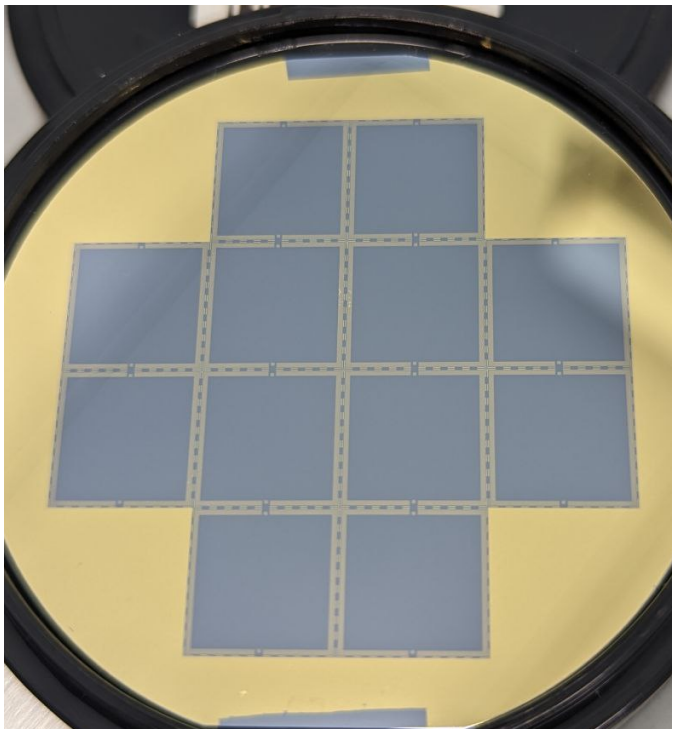

Figure 3.7: Image of the whole wafer after the liftoff of the 1st lithography step.

Process:

- The wafer is submerged in a beaker with remover for $\approx 30\,\text{min}$ and heated up to $\approx 60\,^{\circ}\text{C}$

- If the resist does not come off easily, the wafer can be placed in an ultrasonic bath for few minutes with high power
- Once the resist is removed the wafer is rinsed with IPA and dried with nitrogen
- An inspection is performed with an optical microscope to check the quality of the lift-off
- If some metals are still present the wafer can be submerged again in the remover for few minutes and further ultrasonic baths can be performed

2nd lithography

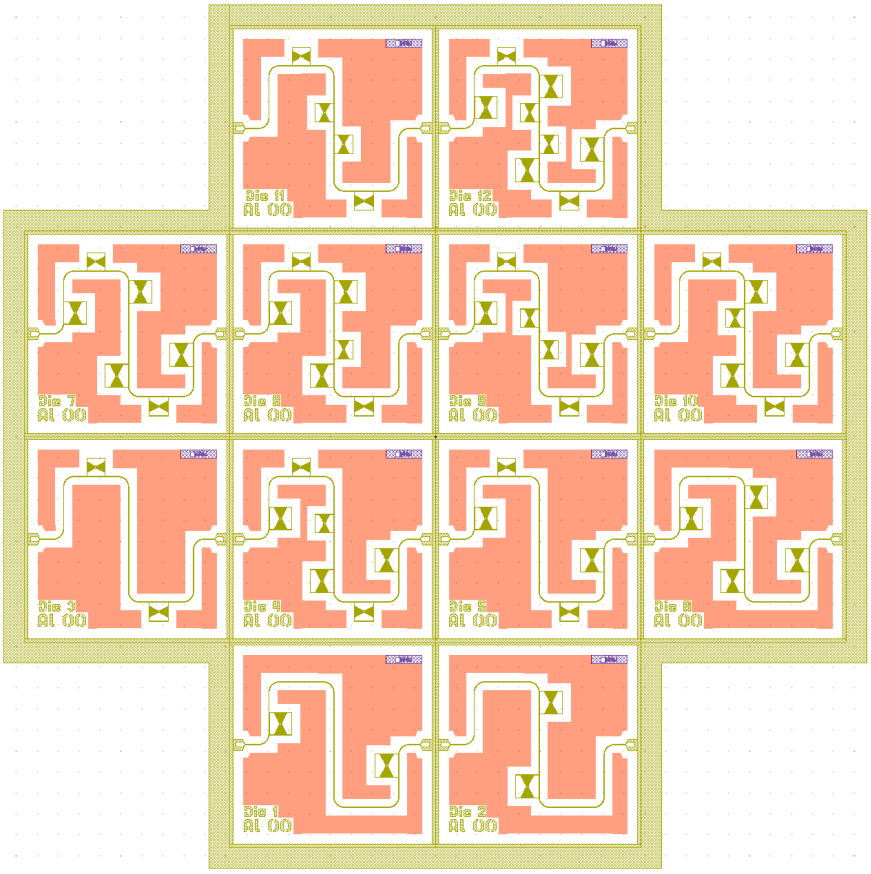

Figure 3.8: Image of the mask used in the 2nd lithography step.

This lithographic step is identical to the first one, except for the pattern to be exposed. The very same equipments and parameters are used. Few differences are present: the initial bake in the coating step is not needed, since the wafer has

already been baked in the first lithographic step. Since the pattern is yet present on the wafer it is necessary to align the new pattern to the previous one during the laser writing step. All the rest of the process is identical to the first lithographic step.

This step is a bit more difficult with respect to the first one, as smaller features are present, thus the development becomes more critical. I would like to give particular attention to the deposition step since the thickness of Al is crucial for the operation of the resonators.

Al deposition

Al is deposited on the wafer using the same Temescal evaporator. The thickness of the Al layer is critical for the operation of the resonators, thus it is important to carefully control the deposition parameters. To built an electrically continuous film it is necessary to deposit at a very high rate, in this case we set it at $5\,\text{Å}\,\text{s}^{-1}$. This high rate makes the control of the thickness a bit difficult, since the QCM tends to overshoot the desired thickness. For this reason, to achieve a final thickness of 10 nm, we set the deposition to 8 nm. In the characterization section 3.2.2 we will see that the final thickness resulted to be $\approx 10\,\text{nm}$.

Protective coating and dicing

In this step, a protective coating is applied to the wafer to prevent damage during the dicing process. The coating is typically a polymer material that can be easily removed after dicing. Once the coating is applied, the wafer is diced into individual dies using a diamond saw controlled by a proper machine. Single dies are then placed into a die carrier and the protective coating can be removed with 30 min immersion in acetone.

3.2 Dies characterization and results

After the fabrication process, the dies are characterized to evaluate the quality of the fabricated devices. The main parameters we considered for this characterization are:

- Thickness of the Al layer
- Integrity of launchpads and feedline
- Integrity of the resonators and their couplings
- Surface roughness of the Al layer

- Compliance of the dimensions with the design
- Presence of defects or contaminants on the surface
- Presence of the vortex pinner patterns

To perform this characterization we used different instruments available in the PiQuET facility, that are described in the following section.

3.2.1 Instrumentation

In this work we used different instruments to characterize the fabricated dies. The main instruments used are an optical microscope to verify the geometry of the patterns and an atomic force microscope (AFM) which provides informations about roughness and thickness of deposited metals. Both instruments are present in the PiQuET facility, and they required a proper training to be used.

Optical microscope

Figure 3.9: Image of the mounted optical microscope DSX1000.

The optical microscope is a fundamental instrument in microfabrication, used to inspect the quality of the fabricated devices. It allows to visualize the patterns on the wafer with high magnification, enabling the detection of defects, contaminants and other issues that can affect the performance of the devices.

The optical microscope available is the Olympus DSX1000, that allowed us to quickly assess the success of the development and lift-off processes. It is a digital microscope that allows to take high resolution images of the samples. It is equipped with different objectives that allow to change the magnification, and it has a motorized stage that allows to move the sample in the x-y directions and manually in the z-direction. It is also possible to change the illumination conditions, by changing the angle and intensity of the light source. And it is also possible to realize real-time measurements of distances on the sample, to verify the compliance of the dimensions with the design.

Atomic force microscope

The atomic force microscope (AFM) is a powerful instrument used to characterize the surface of materials at the nanoscale [47]. It allows to measure the topography, roughness and other properties of the surface with high resolution. The AFM works by scanning a sharp tip over the surface of the sample, measuring the interactions between the tip and the surface.

The AFM available in the PiQuET facility is a NX10 from Park Systems. It is equipped with a high precision piezoelectric scanner that allows to move the tip in the x-y-z directions with sub-nanometer resolution. The tip is mounted on a cantilever that is deflected by the interactions with the surface, and the deflection is measured by a laser beam reflected on a photodiode. The AFM can operate in different modes, but the default mode we used is the non-contact mode, where the tip does not touch the surface, but it is kept at a constant distance by means of a feedback loop. This mode is less invasive and allows to measure delicate surfaces without damaging them.

For this work we used the AFM to measure the thickness of the Al layer and its surface roughness. The thickness is measured by scanning the tip over a step created by the edge of the Al layer, and measuring the height difference between the Al and the substrate. The roughness is measured by scanning the tip over a flat area of the Al layer, and calculating the root mean square (RMS) of the height variations. This parameter is important to evaluate the quality of the Al layer, since a high roughness can suggest poor film quality or the presence of defects and oxidation.

3.2.2 Results

After the fabrication process, the dies were characterized using the instruments described in the previous section. The optical microscope was used to inspect the geometry of the patterns, verifying the integrity of the launchpads, feedline, resonators and vortex pinning patterns.

Out of 12 dies fabricated on the single wafer, 4 resulted too much damaged and unusable, probably due to issues during the lift-off process, that left some unwanted metal patterns, which would short the resonators or the feedlines. This 4 dies were the ones located in the center of the wafer, suggesting that this is probably due to non-uniformities in the resist coating or in the development process. The other 8 dies did not show particular macroscopical issues in the geometries and were better inspected with the optical microscope.

Geometries

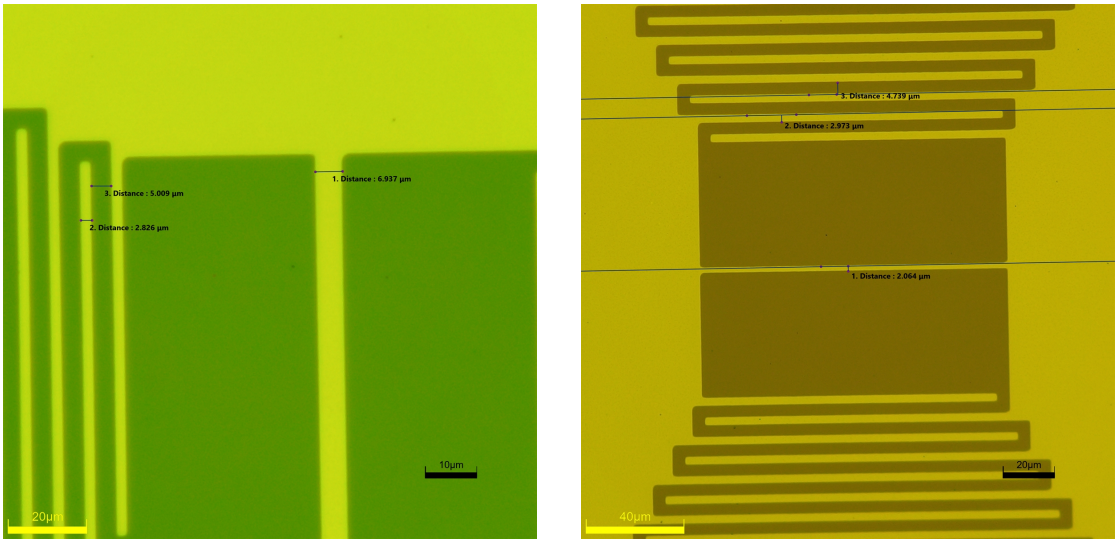

Figure 3.10: Images of the features of the fabricated resonators performed on die 5, for the Bi resonator(a) and P resonator(b).

For the resonator geometries, measurements on die 5 showed some underdevelopment issues, that led to slightly different dimensions with respect to the design. In general the fingers and inductor's width resulted to decrease of $\approx 1\,\mu m$ with respect to the design, while the gaps between fingers increased as expected of $\approx 1\,\mu m$. This leads as stated to a decrease of the capacitance of the resonators, which will reflect

in a higher resonance frequency with respect to the design.

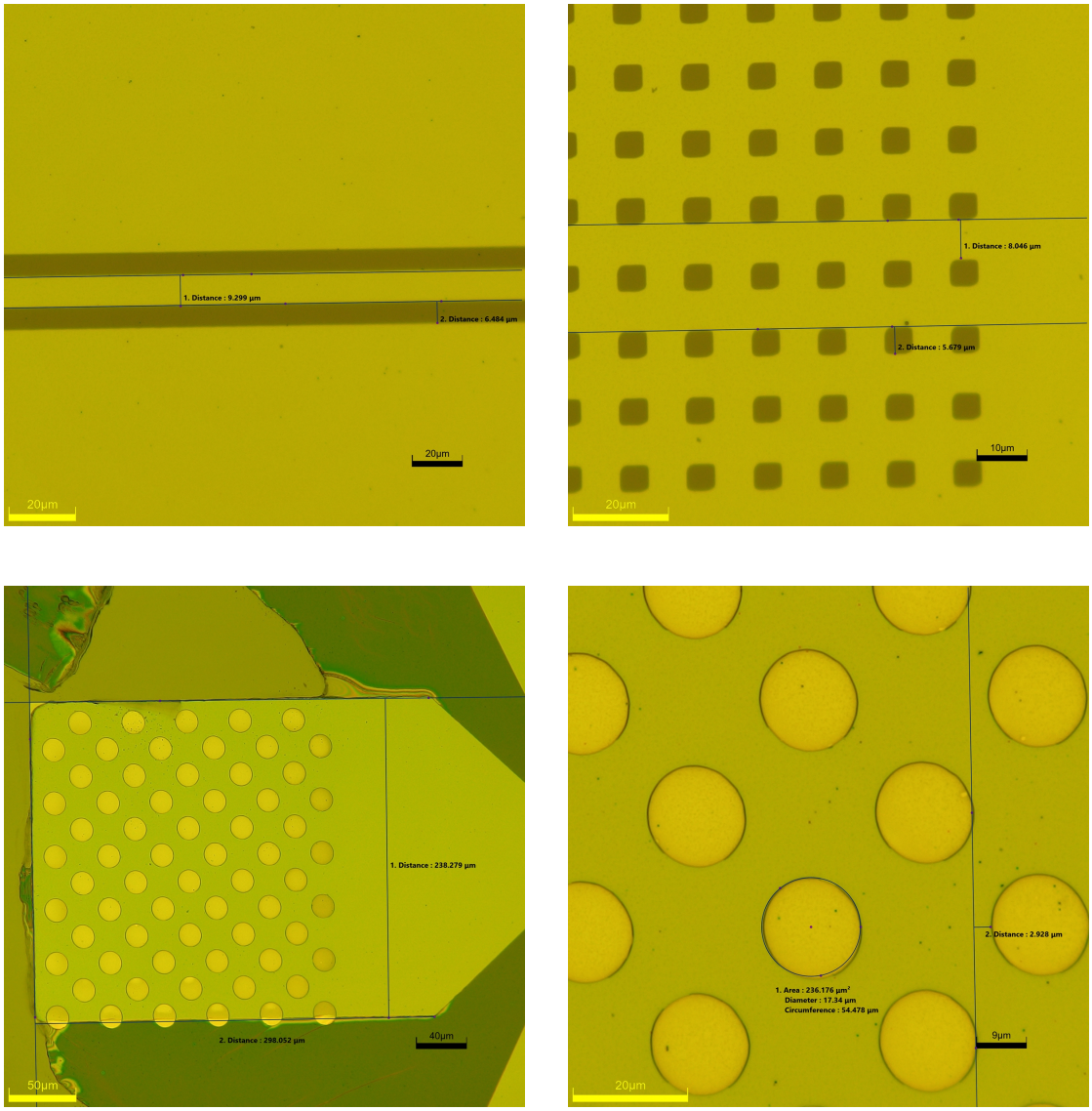

Figure 3.11: Images of the features of the fabricated devices performed on die 5, includes feedline(a), pinners(b), launchpads(c) and Ti/Au pads(d).

For completeness, images of other features of the devices are reported in figure 3.11. Also here some slight deviations from the design are present, but they do not affect the operation of the devices. And do not give any concern about the quality of the fabrication process.

Deposited thickness

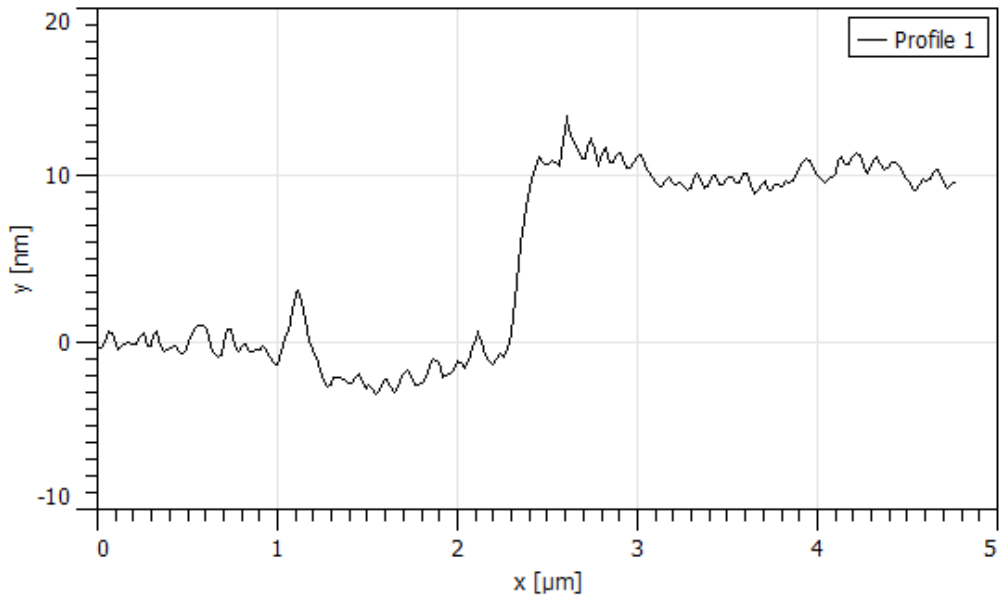

Figure 3.12: Line graph of the AFM scan used to measure the thickness of the Al layer.

The thickness of the Al layer was measured using the AFM, by scanning the tip over a step created by the edge of the Al layer. The main reason to test it was to verify the calibration of the deposition process, since at high deposition rates the QCM of the PVD system tends to overshoot the desired thickness. The measured thickness resulted to be $\approx 10\,\text{nm}$, which is in line with the desired thickness for the operation of the resonators.

Chapter 4

Measurements setup

4.1 Dilution refrigerators

4.1.1 Working principles

A dilution refrigerator is a device used to reach extremely low temperatures, often below 10 millikelvin, where conventional cooling methods no longer work. It operates using a mixture of two helium isotopes: helium-3 and helium-4. At temperatures below about 0.87 K, these two isotopes separate into two phases — a concentrated phase rich in helium-3 and a dilute phase where helium-3 is dissolved in helium-4. Cooling occurs when helium-3 atoms cross from the concentrated phase into the dilute phase, absorbing heat in the process. This continuous transfer of helium-3 provides steady cooling power. The system requires pumps to circulate the helium-3 and maintain the phase boundary. The process is based on quantum mechanical effects related to Fermi and Bose statistics of the isotopes. Dilution refrigerators are essential in experimental physics, especially in quantum computing and low-temperature condensed matter research. Despite their complexity, they offer reliable and stable operation at millikelvin temperatures.

Dilution refrigerators are essential for superconducting quantum electronics because they provide the ultra-low temperatures required for superconductivity to occur. At these temperatures, thermal noise is drastically reduced, allowing, for example, qubits to maintain coherence for longer times. Superconducting circuits can then exhibit quantum behavior without energy losses. The stability and continuous operation of dilution refrigerators make them ideal for sustaining delicate quantum states. Without such extreme cooling, the quantum properties of superconducting devices would quickly vanish.

In this work the use of dilution refrigerators is crucial for performing experiments

on the devices, as they provide the necessary low temperatures for Aluminum to become superconductive. Moreover, the low temperatures help to minimize thermal noise, which is essential for achieving high-fidelity measurements and maintaining the coherence of quantum states in the devices under study. Niobium devices could also be measured in a ^3He cryostat, which can reach temperatures down to about few Kelvin, at these temperatures though, the critical magnetic field may become too low for operativity.

Leiden cryogenics CS-110

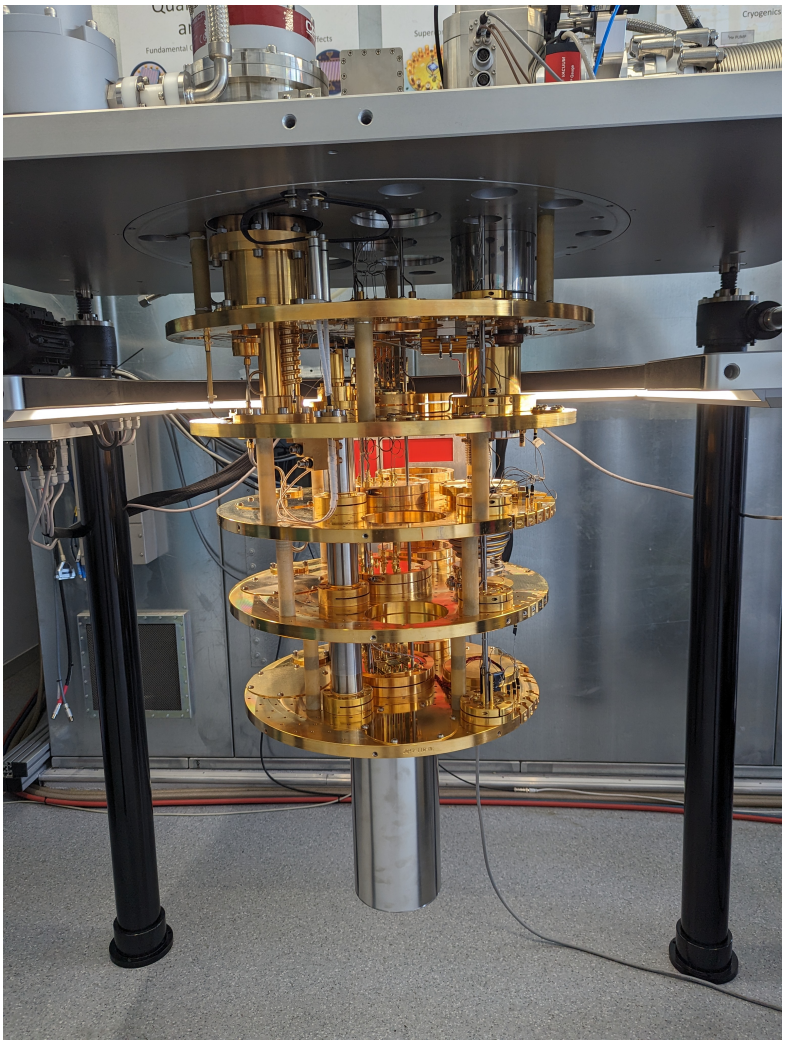

Figure 4.1: Image of the Leiden Cryogenics CF-CS110 dilution refrigerator mounted at Quantum Circuits for Metrology Lab at INRiM.

The Leiden Cryogenics CF-CS110 used in our setup is a cryogen-free dilution refrigerator equipped with a single pulse-tube cooler and a superconducting magnet capable of reaching magnetic fields up to 9 T. It operates at base temperatures below 10 mK and provides a cooling power on the order of hundreds of microwatts at 100 mK. Our configuration includes an insertable probe, which allows rapid sample exchange and cooldown from room temperature to base temperature within a few hours. The system's large experimental space accommodates complex wiring and magnet integration while maintaining excellent temperature stability. Its low-vibration and fully cryogen-free design make it ideally suited for experiments in superconducting quantum electronics and other ultra-low-temperature applications.

Of course, this dilution refrigerator is equipped with the possibility of interfacing with electrical measurement equipment at room temperature. This is done through a series of coaxial cables and DC lines that are thermalized at different temperature stages within the refrigerator. These cables are designed to minimize thermal conduction while maintaining signal integrity, ensuring accurate measurements at millikelvin temperatures. The wiring setup includes low-noise amplifiers, filters, and attenuators to optimize signal quality and reduce noise. In the next section we will discuss in detail the electronics setup used for measurements and the specific devices used for signal transport in the refrigerator.

4.2 Electronics setup

4.2.1 VNA measurements

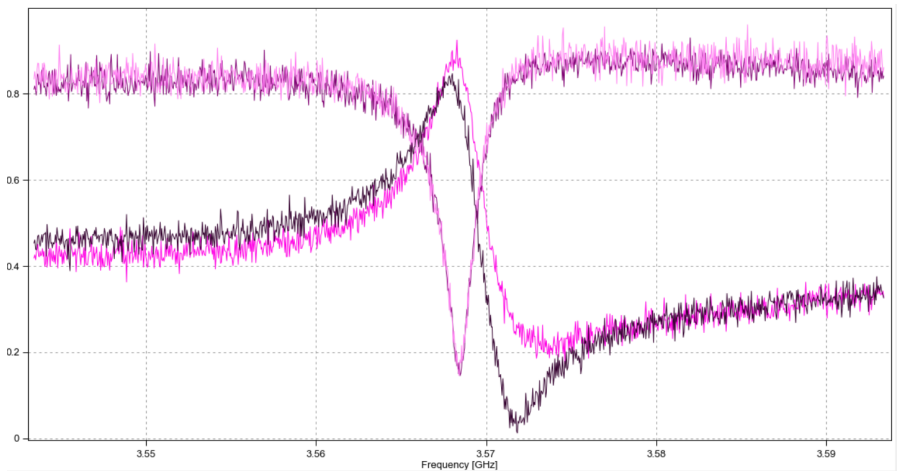

Figure 4.2: Image of the S-parameter measurement using a two-port Vector Network Analyzer (VNA).

A Vector Network Analyzer (VNA) is an instrument used to measure the electrical response of high-frequency components and networks. It operates by generating a known signal and measuring both its magnitude and phase after interaction with the device under test (DUT). The VNA characterizes the DUT through the so-called scattering parameters, or *S-parameters*, which describe how incident and reflected waves relate at each port. Each parameter S_{ij} represents the ratio between the wave exciting port i and the wave entering port j. For example, S_{11} corresponds to the reflection coefficient, while S_{21} represents the transmission coefficient. By measuring these complex quantities, the VNA provides complete information on both amplitude and phase behavior over frequency. This makes it a fundamental tool for RF and microwave engineering. In particular, it is widely used to study resonators, since their resonance frequency, quality factor, and losses can be directly extracted from the S-parameter response. Typical measurements include observing the magnitude and phase of S_{21} or S_{11} around the resonance. Hence, the VNA enables precise characterization of resonance phenomena and coupling mechanisms in microwave devices.

Keysight PNA-X

The Keysight PNA-X is a high-performance VNA designed for advanced RF and microwave measurements. It features multiple test ports, extremely wide frequency coverage, and high dynamic range for precise S-parameter characterization. Its advanced calibration and measurement capabilities allow accurate extraction of device parameters, including low-loss and high-Q resonators. The PNA-X supports automated measurements, time-domain analysis, and multi-port network analysis, making it suitable for complex DUTs. Its user-friendly software interface and integration with external instruments streamline measurement workflows in research and industry applications.

4.2.2 Sample heater

The sample heater is a crucial component for controlling the temperature of the device under test (DUT) within the dilution refrigerator. It allows for precise temperature tuning and stabilization, which is essential for accurate measurements and experiments. The heater is typically located close to the sample and is designed to minimize thermal resistance, ensuring efficient heat transfer. Temperature control is achieved through a feedback loop that monitors the sample temperature and adjusts the heater power accordingly. This setup enables rapid temperature changes and fine-tuning, which are particularly important for studying temperature-dependent phenomena in superconducting materials.

Lakeshore 355

The Lakeshore 355 is a precision temperature controller designed for cryogenic applications. It provides accurate temperature regulation through a combination of PID control and advanced measurement techniques. The controller supports multiple sensor types, including resistance thermometers and thermocouples, allowing for versatile temperature monitoring. With its high-resolution output and user-friendly interface, the Lakeshore 355 is well-suited for demanding cryogenic applications.

4.3 Magnetic field

For measurements requiring an external magnetic field, our setup includes a superconducting magnet integrated into the dilution refrigerator. This magnet can generate fields up to 9 Tesla, providing a controlled environment for studying the magnetic properties of superconducting devices. Magnets for dilution refrigerator usually come with a proper stage and are thermally anchored to the still plate. In fact the cooling power needed to cool down the magnet coils during operation is quite high, and the still stage is the one that can provide it without affecting the base temperature of the mixing chamber. The magnet is powered by a dedicated power supply that allows for precise control of the magnetic field strength.

In the quantum circuits for metrology lab, we did not have a probe compatible with the use of the magnet due to the presence of magnetizable components. So, to allow measurements in low fields (up to about 1 T), we needed to design a custom cold finger to be inserted in the magnet and attached to the mixing chamber plate. And a dedicated magnetic shield made of Pb, which becomes superconducting at low temperatures, was also designed to protect the upper parts of the probe from unwanted magnetic flux.

4.3.1 Cold finger design

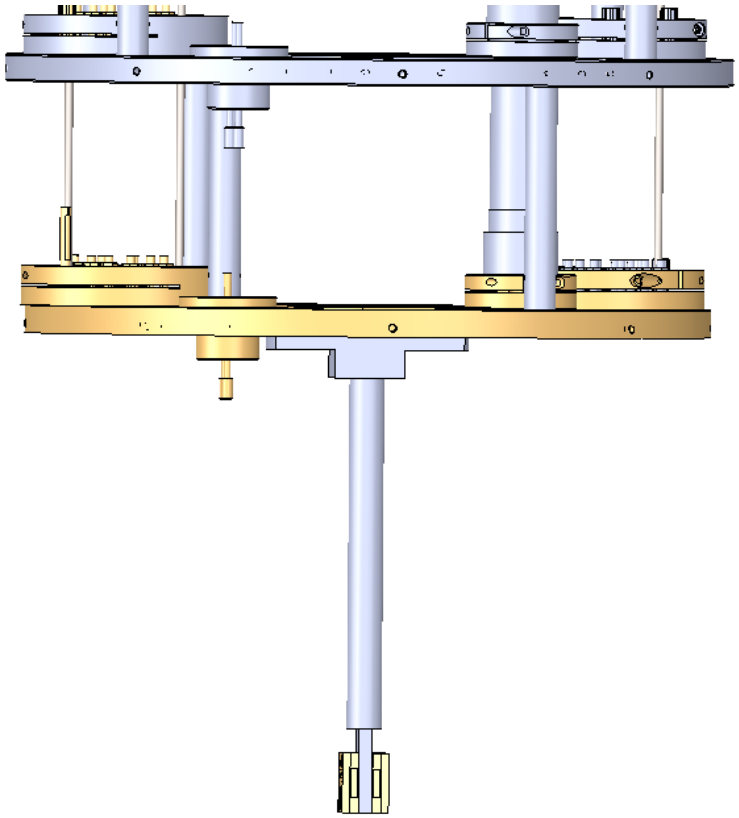

Figure 4.3: Solid model of the fully assembled custom cold finger mounted in the dilution refrigerator magnet bore.

Designing a custom cold finger for insertion into the superconducting magnet required careful consideration of several mechanical and thermal factors. The cold finger needed to be compact enough to fit within the magnet's bore while providing sufficient thermal contact with the mixing chamber plate of the dilution refrigerator. Copper is typically used for its excellent thermal conductivity, ensuring efficient cooling to the device under test (DUT) from the mixing chamber. To allow for satisfactory thermalization the finger should have a large contact area with the mixing chamber plate and the device carriers, avoiding dangling contacts, moreover it has to have the largest possible section area to avoid thermal resistances. At the same time thermalizaing very large masses is not feasible due to the limited cooling power of the mixing chamber, so a compromise had to be found between these two aspects.

The final solution involved the design of two components:

- An attachment plate that connects the cold finger to the mixing chamber. It has mounting holes for secure attachment by screws and a conical insert for increased contact area for the cold finger.
- The cold finger itself, which extends downward into the magnet bore. It consists of a thick copper rod with a flat end for mounting the DUT. The rod is designed to maximize thermal conduction while fitting within the spatial constraints of the magnet.

The entire assembly was designed using CAD software to ensure precise dimensions and fitment. And the components were fabricated using high-purity oxygen free copper to optimize thermal performance and finally gold plated to avoid absorption of radiation.

Magnetic shield design

The magnetic shield was designed to protect the upper parts of the probe from unwanted magnetic flux when operating the superconducting magnet. We designed a superconducting shield made of lead (Pb), which effectively expells magnetic fields through the Meissner effect. The shield was designed as a very thin disk that could be attached to the mixing chamber plate, with a central hole to allow the cold finger to pass through. The disk shape was chosen to provide maximum coverage while minimizing material usage and weight. For superconducting shields in fact, it is not necessary to have thick walls, since the magnetic field is expelled from the interior of the superconductor. The shield structure was simulated using a finite element analysis software (COMSOL) to ensure it would provide adequate shielding effectiveness at the desired magnetic field strengths.

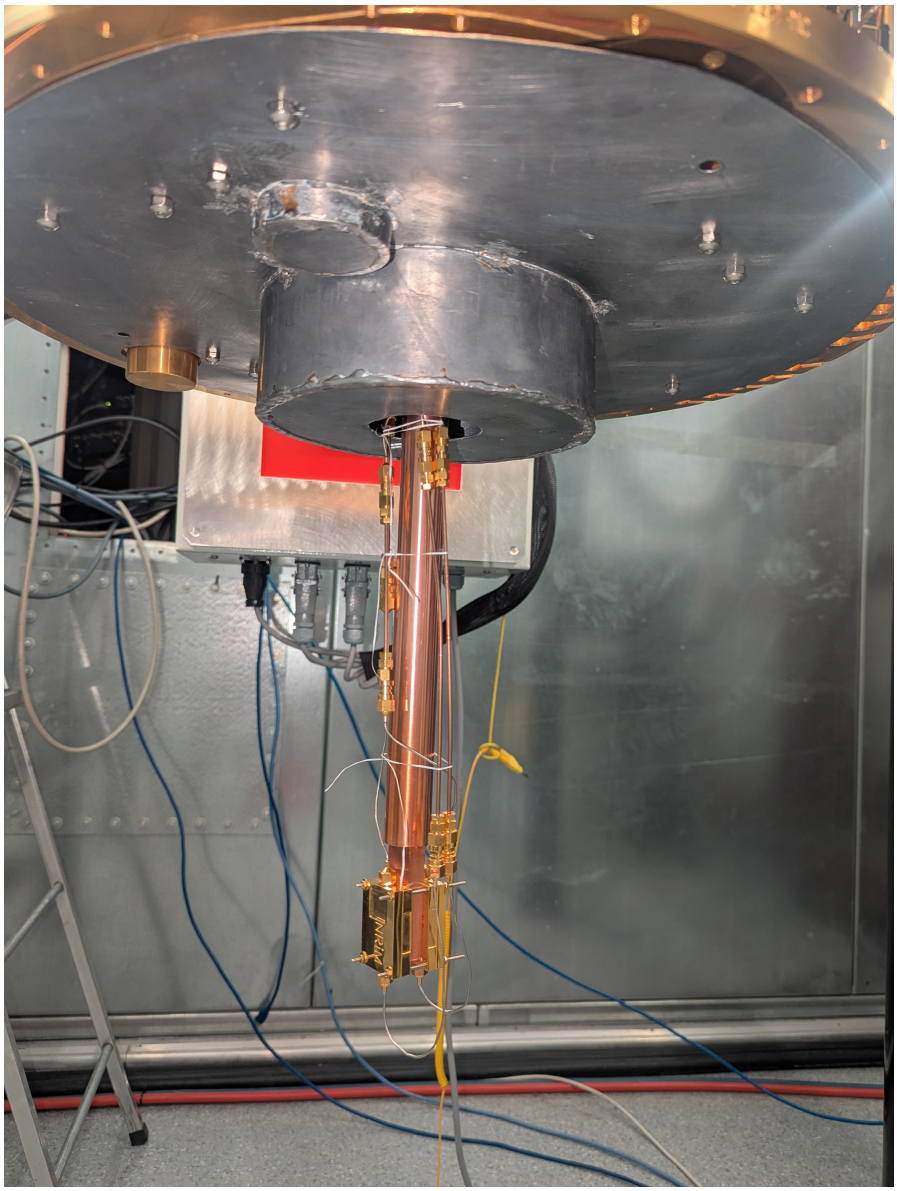

Figure 4.4: Photo of the superconducting magnetic shield and copper cold finger designed for compatibility with the mixing chamber structure.

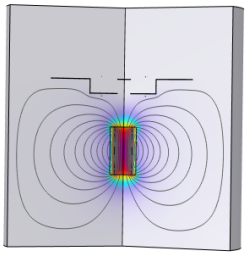

(a) Representation of the magnet and shielding geometry inside COMSOL Multiphysics.

(b) 2D heatmap of magnetic field right above the shield. Dark regions arrive up to $\approx 2\,\mathrm{mT}$.

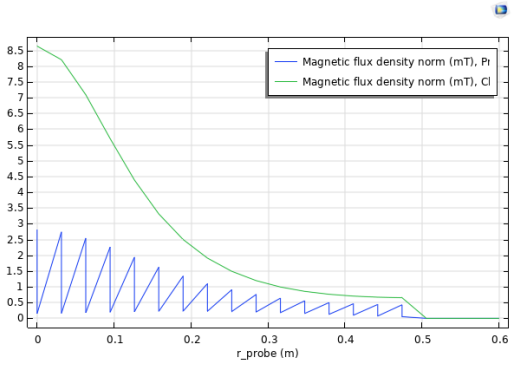

(c) Graph representing the magnetic field above and below the shield when no shielding is applied.

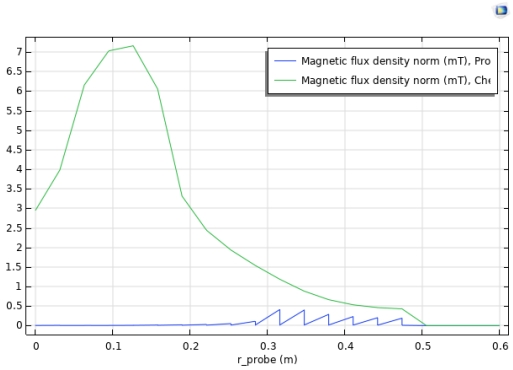

(d) It is possible to see the effect of the shielding on the magnetic field distribution as the probed field above the shield drops to μT values.

Figure 4.5: Overview of the magnetic field simulation performed with COMSOL Multiphysics to validate the shielding design.

Chapter 5

Results

In this chapter, I am presenting the results obtained from the measurements of the fabricated superconducting resonators. Their resonance frequencies have been analyzed, quality factors, impedance characteristics, and their behavior under varying power levels and temperatures. Additionally, the presence of two-level systems (TLS) and the interaction of the resonators with external magnetic fields. Finally, we compare the performance of thin Aluminum resonators with that of other standard Niobium resonators.

Measured device

The device measured consists of a chip with 8 resonators, each with different geometrical parameters. The resonators are capacitively coupled to a common feedline, allowing for simultaneous measurement of all resonators. Out of the 8 resonators, we expect to find 7 resonance frequencies within the measurement, as one of them had visible defects from fabrication phase. Three of the resonators are designed for frequencies around 5 GHz, while the remaining four are designed for frequencies around 7.5 GHz.

5.1 Resonance frequencies and quality factors

The proper resonances s-parameters of the resonators have been measured using a Vector Network Analyzer (VNA) connected to the feedline. These measurements have been performed at a base temperature of $\approx 80\,\mathrm{mK}$.

We expect to find the resonance frequencies at the target frequencies with a Full Width Half Maximum (FWHM) of around 1 MHz, the shape of the parameters should be a deep in the transmission and a peak in reflectance.

Finally only 4 resonances have been found, 2 around 3.5 GHz and 2 around 6 GHz. Each resonance has been fitted with a complex Lorentzian function to extract the resonance frequency f_r and the quality factors Q_i and Q_c. The results of the fitting procedure are summarized better in the next section, where quality factor is analyzed in detail in relationship with power and temperature. An example of a fit is left here, to show that the quality factor is of the order of 10^3 which is consistent with our expectations.

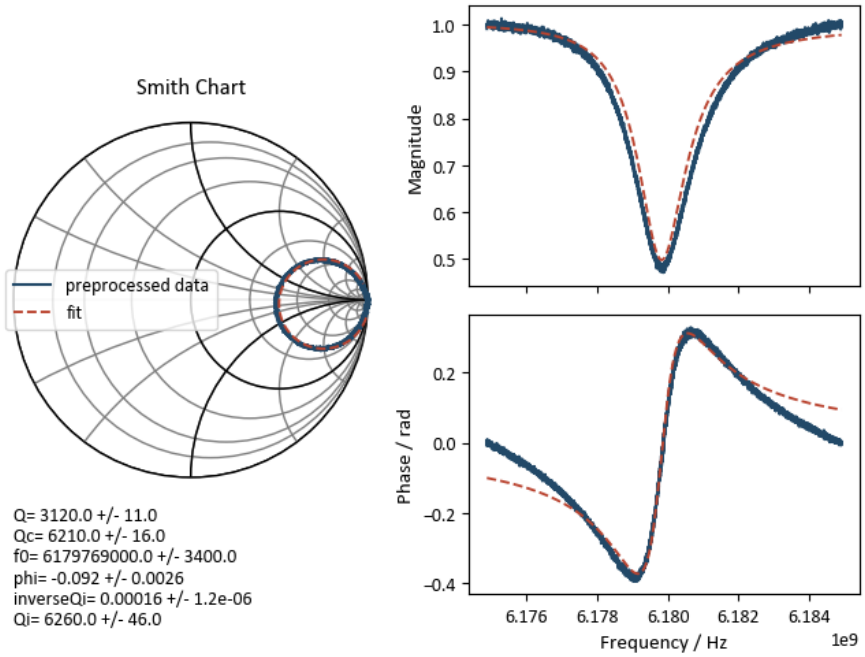

Figure 5.1: Example of a Lorentzian fit to the resonance peak, allowing for the extraction of f_r and Q factors.

5.2 Dependence on power and temperature

The fitting parameters have been extracted for different input power levels and temperatures. Allowing to analyze results for contribution to losses from TLS and quasiparticles mechanisms.

Power dependence

The VNA input power has been varied from −80 dBm to 0 dBm, in steps of 5 dBm. It must be considered that to allow cryogenic operation, a total of ≈ 55 dB of

attenuation is applied up to the DUT.

As expected the resonance frequencies in each and every resonator start to shift towards lower frequencies when high power is applied. This is due to the saturation of TLS at high power levels, which causes a decrease in the dielectric constant and thus a decrease in the resonance frequency. At very low power $\langle -75\,\mathrm{dBm}$ instead, we are below the noise level of the VNA, so it is not possible to see any resonance shape.

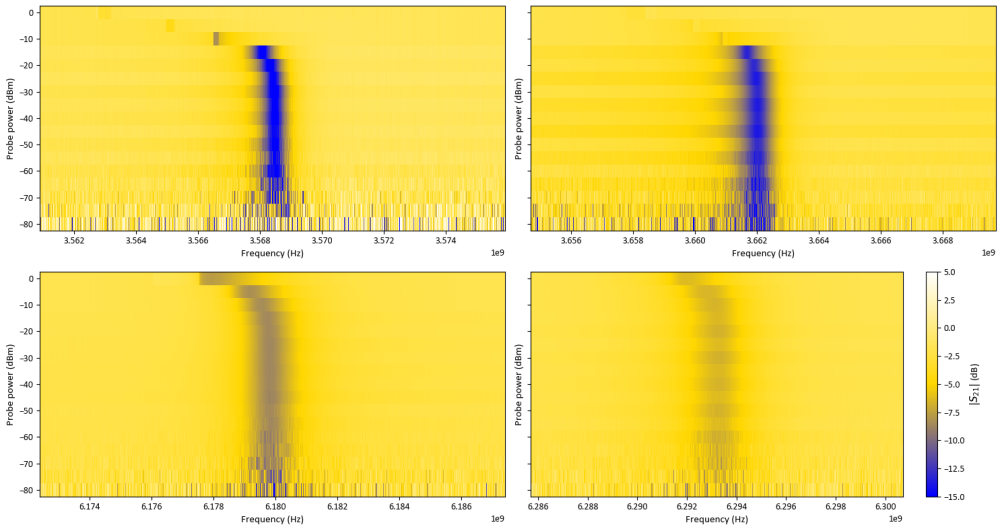

Figure 5.2: S_{21} parameters as a function of input power, showing the resonance frequency shift in each of the four resonators.

Also quality factors are affected by the input power.

An interesting plot is the one showing the internal quality factor Q_i as a function of the average number of photons in the resonator $\langle n_{ph} \rangle$. This is calculated using the formula:

$$\langle n_{ph} \rangle = \frac{2Q_l^2}{Q_c} \frac{P_{in}}{\hbar \omega_r^2} \tag{5.1}$$

Where Q_l is the loaded quality factor, P_{in} is the power at the resonator input, and $\omega_r = 2\pi f_r$ is the angular resonance frequency.

Temperature dependence

Increasing the temperature of the sample is a common way to characterize the loss mechanism in superconducting resonators. With temperature the different contributions to losses change differently, allowing to identify the dominant mechanism.

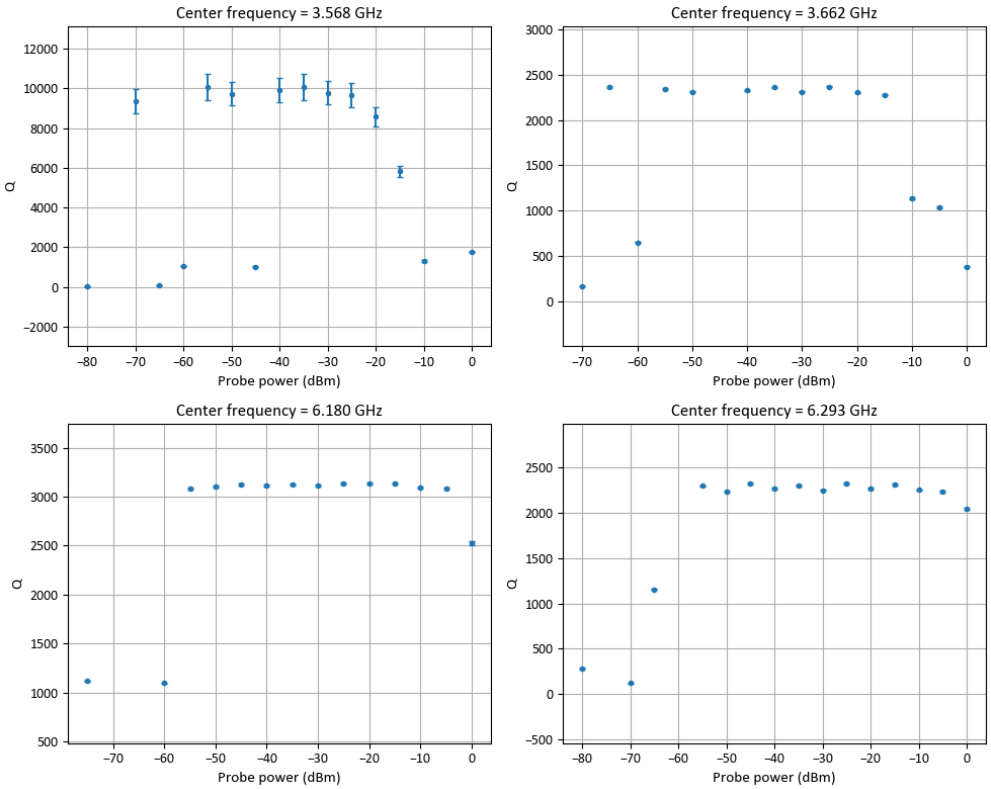

Figure 5.3: Total quality factor Q on each resonator as a function of input power.

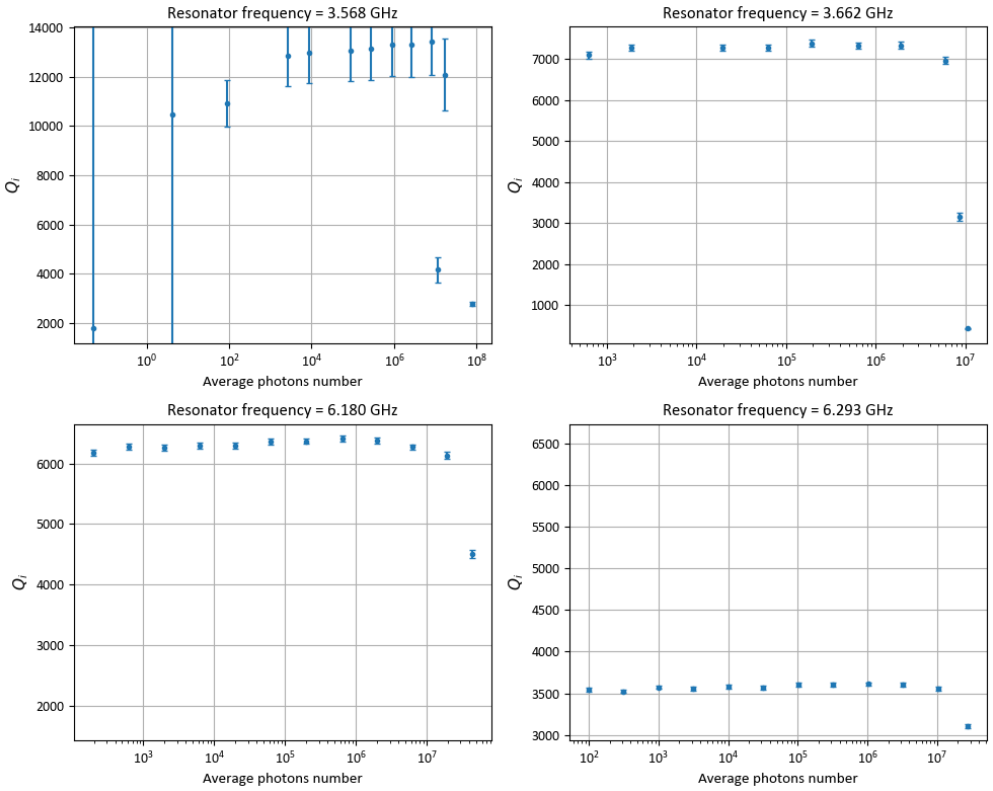

Figure 5.4: Internal quality factor Q_i on each resonator as a function of the average number of photons $\langle n_{ph} \rangle$.

In the QCM lab setup there is a limited possibility to change the temperature of the mixing chamber, so the measurements have been performed from base temperature $\approx 80\,\text{mK}$ up to 600 mK. The heating up mechanism is performed by means of a resistive heater placed on the mixing chamber plate, using the Lakeshore PID controller. It was thus possible to set a target temperature and wait for the system to stabilize before performing the measurement. Unfortunately it is not possible to raise the temperature above 600 mK due to possible damages to the dilution refrigerator when requiring excessive cooling power. To perform the anlisys we needed to reach temperatures up to $\approx \frac{T_c}{2}$, Aluminum is then compatible with this limit, having a critical temperature of $\approx 1.2\,\text{K}$ in bulk, while for Niobium it was not possible to perform this analisys as a comparison.

As expected, increasing the temperature causes a shift of the resonance frequency towards lower frequencies, due to the increase in kinetic inductance as the number of quasiparticles increases.

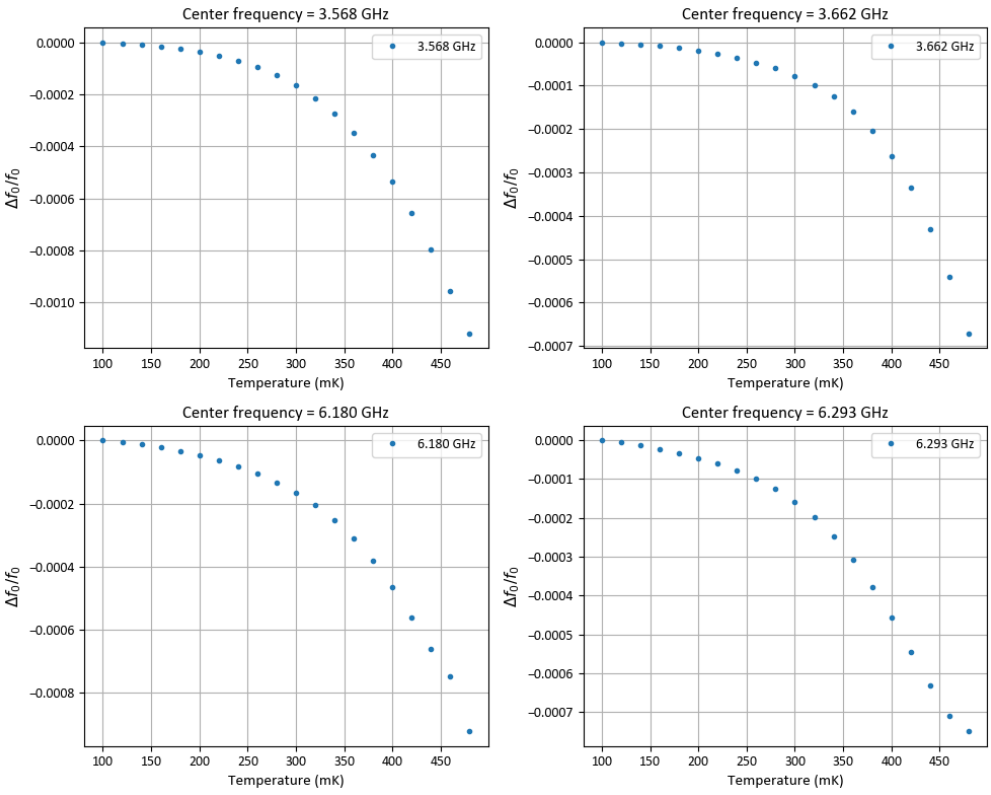

Figure 5.5: Normalized resonance frequency shift in each of the four resonators.

Since the quasiparticles tends to absorb energy from the resonator, the total

quality factor Q decreases with temperature as well. With important effects that can be seen also in loaded quality factor Q_i, which is also used for analisys in the next section.

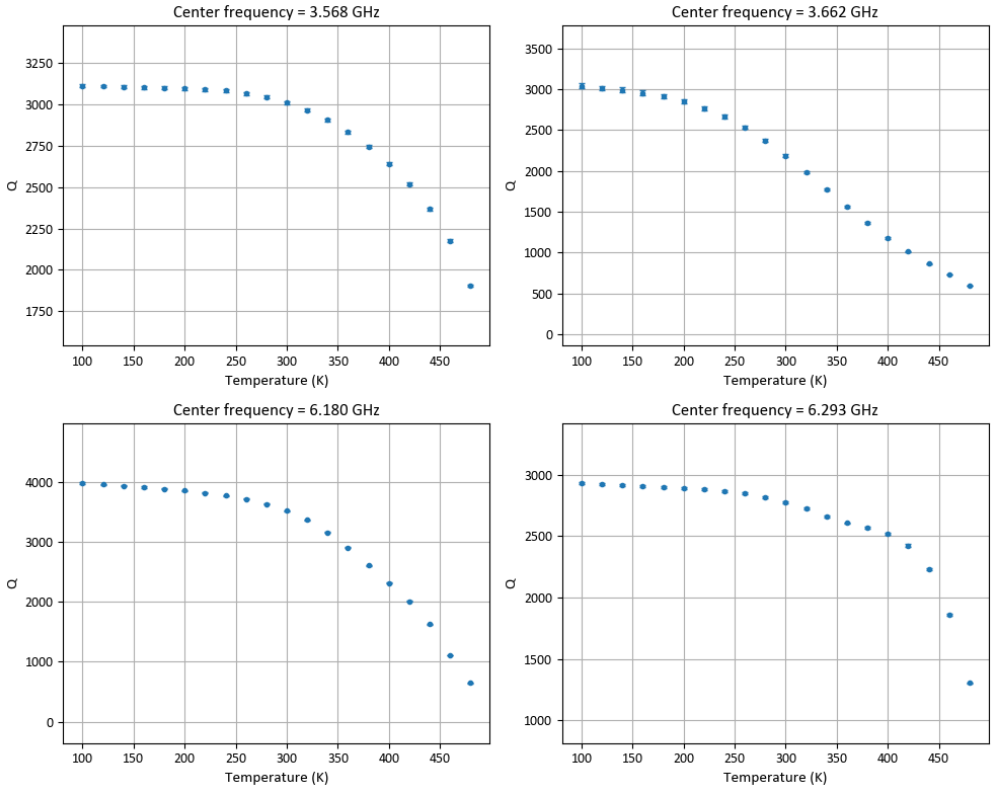

Figure 5.6: Total quality factor Q on each resonator as a function of temperature.

5.3 Critical Temperature characterization

Measures of absorption of energies at resonance frequencies with varying temperature are used to estimate several parameters of the superconducting film. In particular by applying the Mattis-Bardeen theory[48] it is possible to extract the critical temperature T_c of the film, contribution of the kinetic inductance to total inductance $\frac{L_k}{L_{tot}}$ and finally the participation ratio to losses of TLS and quasiparticles $\delta_i = \delta_{TLS} + \delta_{qp}$.

Complex conductivity $\sigma(T) = \sigma_1(T) - j\sigma_2(T)$ of the superconductor is modeled as a function of temperature, and then used to calculate the resonance frequency

shift and quality factor variation with temperature, fitting with T_c and $\alpha = \frac{L_k}{L_{tot}}$ as free parameters. Directly from MB theory it is possible to state that [49]:

$$Q_{MB} = \frac{2}{\alpha}\frac{\sigma_2(\omega, T)}{\sigma_1(\omega, T)} \tag{5.2}$$

Where Q_{MB} is the theoretical contribution to quality factor predicted by MB theory, and ω is the angular resonance frequency. When temperatures are too low there is a deviation from the MB theory due to the presence of TLS, so the total internal quality factor is modeled as:

$$\frac{1}{Q_i(T)} = \frac{1}{Q_{MB}(T)} + \frac{1}{Q_s} \tag{5.3}$$

With Q_s being a constant fitting parameter representing a saturation quality factor that can be seen at low temperatures.

First thing to be done is to express the complex conductivity terms as a function of critical temperature T_c, we can use an approximation of the Mattis-Bardeen theory valid for $\hbar\omega \ll \Delta_0$ and $k_B T \ll \Delta_0$ [50, 51, 52]:

$$\frac{\sigma_1}{\sigma_n} = \frac{4\Delta_0}{\hbar\omega} \exp\left(-\frac{\Delta_0}{k_B T}\right) \sinh\left(\frac{\hbar\omega}{2k_B T}\right) K_0\left(\frac{\hbar\omega}{2k_B T}\right) \tag{5.4}$$

$$\frac{\sigma_2}{\sigma_n} = \frac{4\Delta_0}{\hbar\omega}\left[1 - \sqrt{\frac{2\pi k_B T}{\Delta_0}} - 2\exp\left(-\frac{\Delta_0}{k_B T}\right) \exp\left(-\frac{\hbar\omega}{2k_B T}\right) I_0\left(\frac{\hbar\omega}{2k_B T}\right)\right] \tag{5.5}$$

Where σ_n is the normal state conductivity, $\Delta_0 = 1.76 k_B T_c$ is the superconducting energy gap at zero temperature, k_B is the Boltzman constant and K_0 and I_0 are the modified Bessel functions of the second and first kind, respectively.

If we have fixed temperatures and frequencies, we can fit the measured $Q_i(T)$ with the model to extract T_c, by substituting the energy gap, and α.

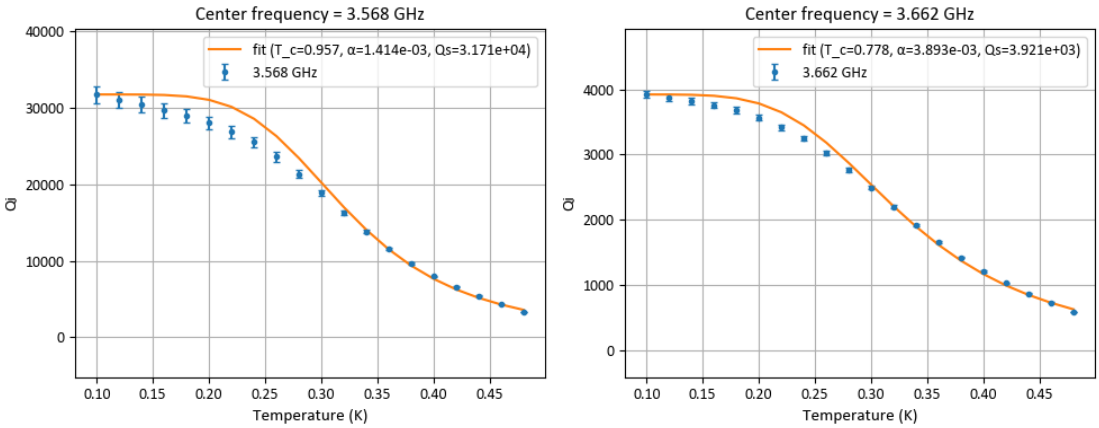

Figure 5.7: Internal quality factors of two resonators fitted with the Mattis-Bardeen theory to extract critical temperature and kinetic inductance fraction accordingly to equation 5.3.

For the higher frequencies resonators the fit resulted in poor success, probably due to the limited temperature range available. With the data available from the lower frequency resonators it was possible to extract a critical temperature of $T_c = 778 - 957mK$ and a kinetic inductance fraction different for the two resonators of $\alpha_1 = 1.4 \cdot 10^{-3}$ and $\alpha_2 = 3.9 \cdot 10^{-3}$. To validate this approach, the resonance frequency shift has been fitted as well with the same parameters.

The resonance frequency shift as a function of temperature is modeled by varying with the variation in kinetic inductance and thus imaginary part of complex conductivity σ_2 with respect to the reference value at base temperature $\sigma_{20} = \sigma_2(T = 100mK)$:

$$\frac{\delta f_r(T)}{f_r} = \frac{\alpha}{2} \frac{\sigma_2(T) - \sigma_{20}(T)}{\sigma_{20}(T)} \tag{5.6}$$

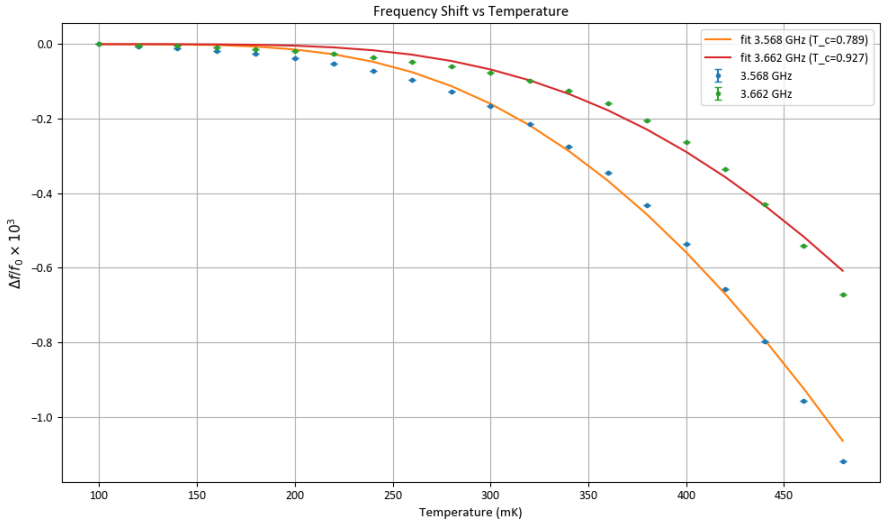

Figure 5.8: Resonance frequency shift of two resonators fitted with the Mattis-Bardeen theory to extract critical temperature and kinetic inductance fraction.

The fit of the resonance frequency shift resulted in a very similar range for the critical temperature $T_c = 789 - 927mK$, validating the approach.

5.4 Impedance characterization

Impedance is one of the most important factors for the resonator in order to improve its coupling to the spins. To understand if the designed resonator has a satisfactory impedance within the requirements ($< 10\Omega$), we can employ a technique proposed

in the supplementary materials of [21].

As stated in section 2.2.1, it is possible to calculate with a good precision the inductance of a meandered wire by knowing its geometrical shape. By working a bit on the equation for the resonance frequency we can find the relation:

$$\frac{1}{\omega_{res}^2} = (L + L_p)C \tag{5.7}$$

Two resonators with identical capacitive geometrical structure will have the same capacitance C and parasitic inductance L_p value. If we have then two different resonators with the same structure but different meandered inductors, it is possible to fit the measured resonant period squared $\frac{1}{\omega_{res}^2}$ with Equation 5.7, depending on the calculated L. And acquire L_p and C as fitting parameters, and pushing them back on the impedance equation:

$$Z = \sqrt{\frac{L + L_p}{C}} \tag{5.8}$$

we can acquire the impedance, and also some curves plotting the resonance frequency and the corresponding impedance for that capacitive structure depending on the length, or width of the meandered inductor.

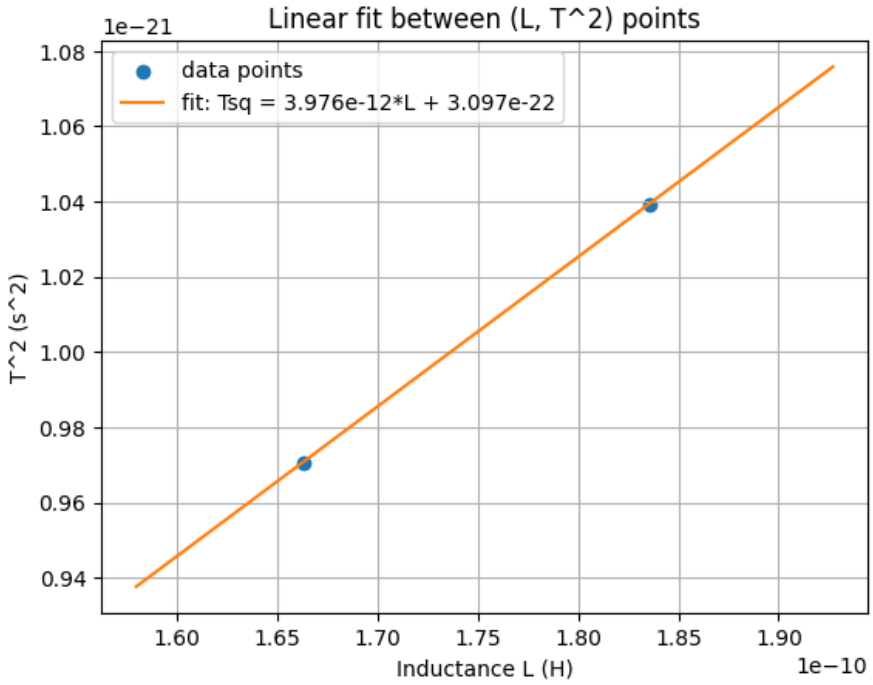

Figure 5.9: Fitted period squared of two resonators resonance frequencies inverse squared, acquired with simulation in COMSOL. Versus calculated inductance of the meandered wire.

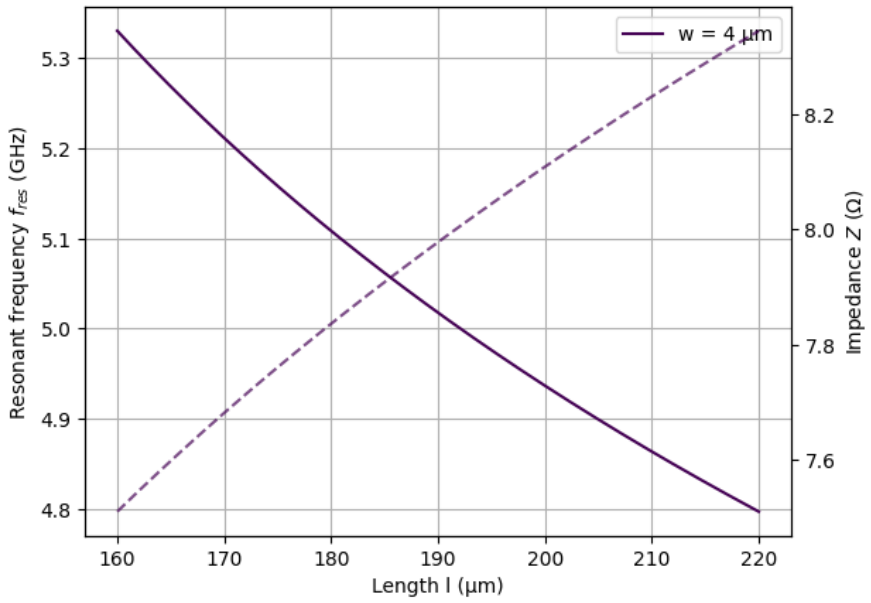

Figure 5.10: Derived relations of resonance frequency (continuous line) and impedance (dashed line) for a given width, by varying length of the inductor.

5.5 Comparison with Niobium resonators

Measurements of standard Niobium resonators fabricated in CNR facility have been performed as well, to compare the performance of our Aluminum resonators with a more standard choice. These resonators showed a higher quality factor at low power and temperature, reaching very high values of quality factors, also higher with respect to Eichler's work.

The tested chip consisted of 6 resonators: 2 with frequencies around 7.5 GHz and 4 at above 5 GHz. This time the measurements showed a broader agreement with simulations, with 5 resonances found out of 6 in the right positions. The s-parameters data has been measured in reflection configuration due to a defect in the bonding process of port 1. Their shape is exactly the same with respect to the Al resonators, but the coupling is much weaker, showing a shallower dip in transmission. This is particularly true for the first resonator at ≈ 5.2 GHz, which shows a very high quality factor, the only resonator found at high frequency is instead the less qualitative. When plotting the loaded quality factor Q_i as a function of average number of photons it is possible to notice the increase of it at higher powers, denoting the saturation of TLS.

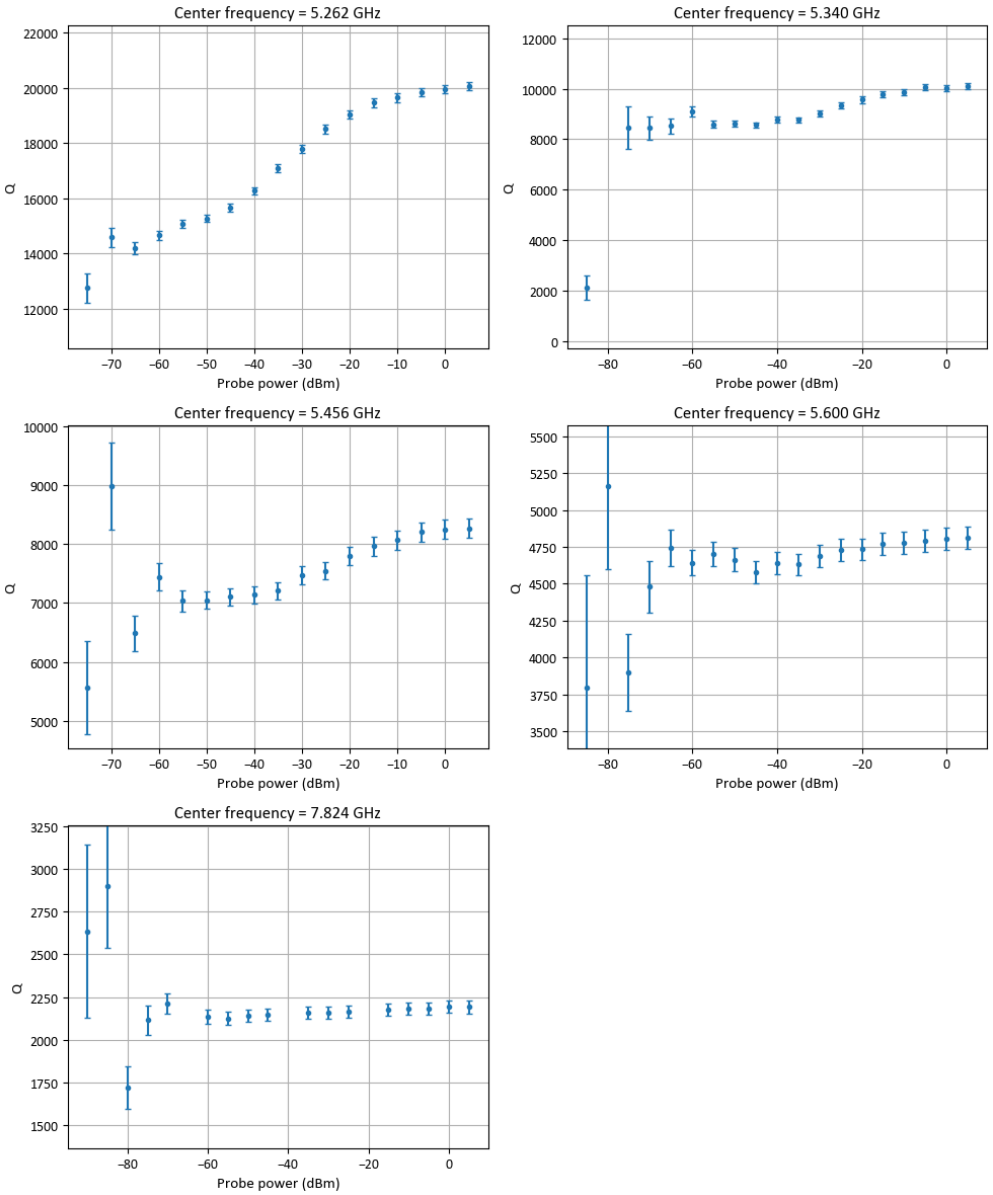

Figure 5.11: Total quality factor Q of the Niobium resonators as a function of input power.

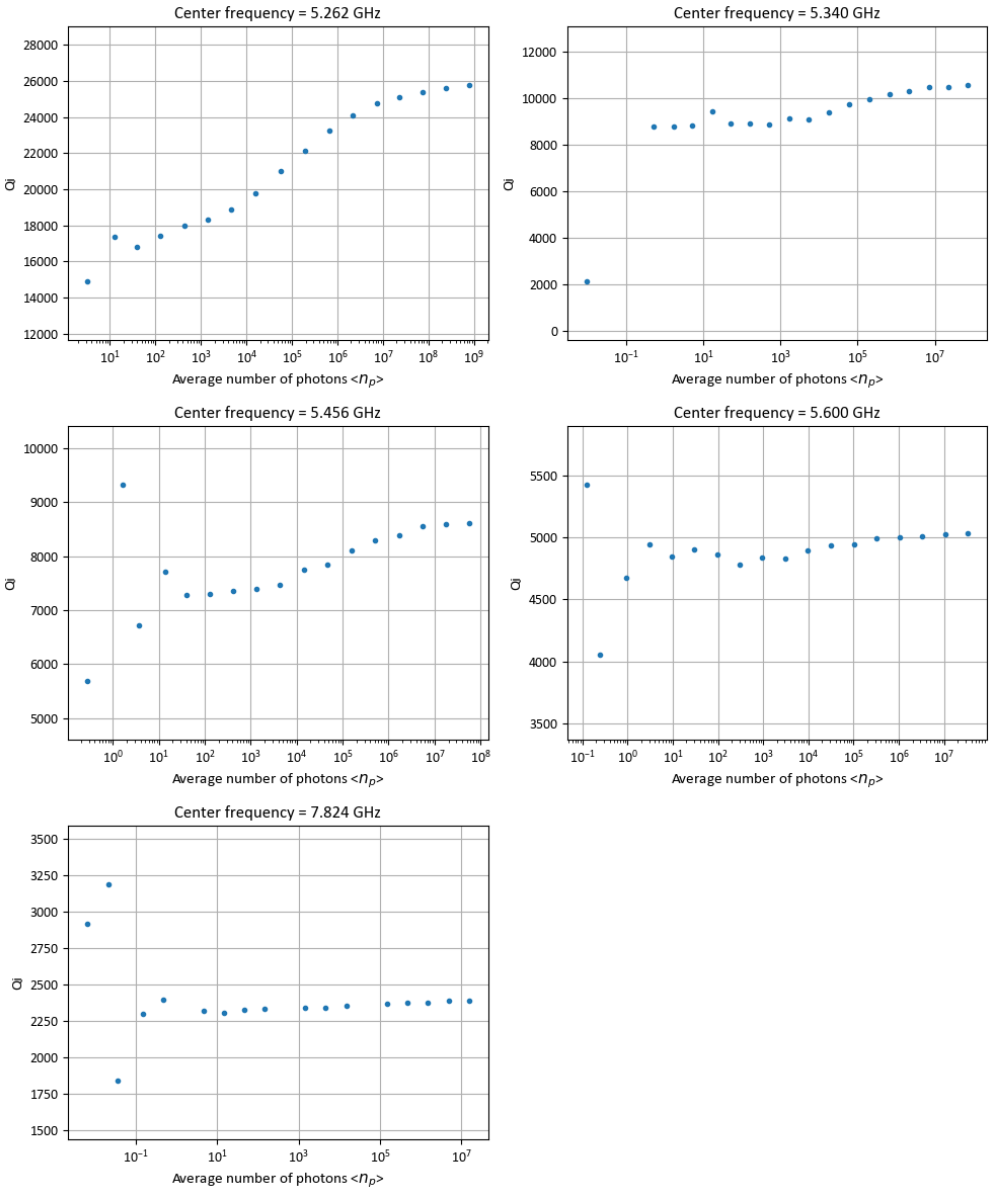

Figure 5.12: Total quality factor Q_i of the Niobium resonators as a function of average number of photons inside the resonator.

5.5.1 TLS characterization

Two level systems are one of the main sources of losses in superconducting resonators at low temperatures and powers. These defects are usually located in the dielectric materials surrounding the resonator, such as the substrate or the surface oxides. They can absorb energy from the resonator, causing a decrease in quality factor and a shift in resonance frequency.

To characterize the TLS contribution to losses, we can use the temperature and power dependence of the resonance frequency and quality factor. Generally speaking, TLS losses dominate at low temperatures and powers, while quasiparticle losses become more significant at higher temperatures. Total losses thus, are expressed in terms of internal quality factor Q_i as:

$$\frac{1}{Q_i} = \delta_{TLS} + \delta_{qp} + \delta_{other} \tag{5.9}$$

For low temperatures the quasiparticle contribution δ_{qp} is negligible, and other losses δ_{other} are assumed to be constant. By fitting the measured data with the standard TLS model, we can extract the TLS loss tangent δ_{TLS}, using [53]:

$$\delta_{TLS} = F \tan\delta_0 \frac{tan(\frac{\hbar\omega}{2k_BT})}{\sqrt{1+\frac{\langle n_{ph}\rangle}{\langle n_c\rangle}}} \tag{5.10}$$

Where F is the filling factor, $\tan\delta_0$ is the intrinsic loss tangent of the TLS, and $\langle n_c\rangle$ is the critical photon number at which TLS start to saturate. By fitting the power dependence of Q_i at low temperatures, we can extract the parameters $F\tan\delta_0$ and $\langle n_c\rangle$ using equation 5.10.

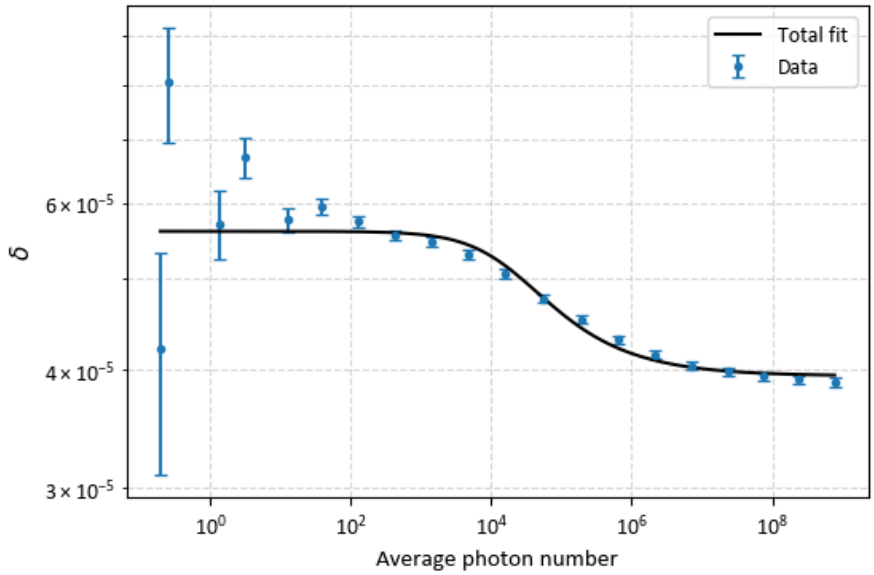

Figure 5.13: Internal quality factor Q_i of the Niobium resonators as a function of average number of photons inside the resonator, fitted with the TLS model to extract TLS loss tangent and critical photon number.

The fit results in a TLS loss tangent of $F \tan \delta_0 = 1.664 \times 10^{-5} \pm 3.8 \times 10^{-7}$ and a critical photon number $\langle n_c \rangle \approx 10^4$ for the resonator with best fitting parameters.

5.6 Interaction with magnetic field

The setup for measurements in the magnetic field allowed to perform measurements with an applied in-plane B field up to $\approx 300\,\mathrm{mT}$.

When applying the magnetic field, a shift in resonance frequency is observed, due to the increase in kinetic inductance as the number of quasiparticles increases. This shift is reversible when removing the magnetic field, indicating that no permanent damage is done to the resonators. It is also expected that the quality factor decreases with increasing magnetic field, due to the increase in losses from quasiparticles. However, the amount of thisn shift should be limited so few MHz, and the quality factor should not decrease too much.

Niobium

In Niobium resonators, the effect of the magnetic field is limited as expected, with a small shift in resonance frequency and a slight decrease in quality factor.

This is due to the higher critical field of Niobium, which allows it to maintain its superconducting properties even in the presence of a moderate magnetic field.

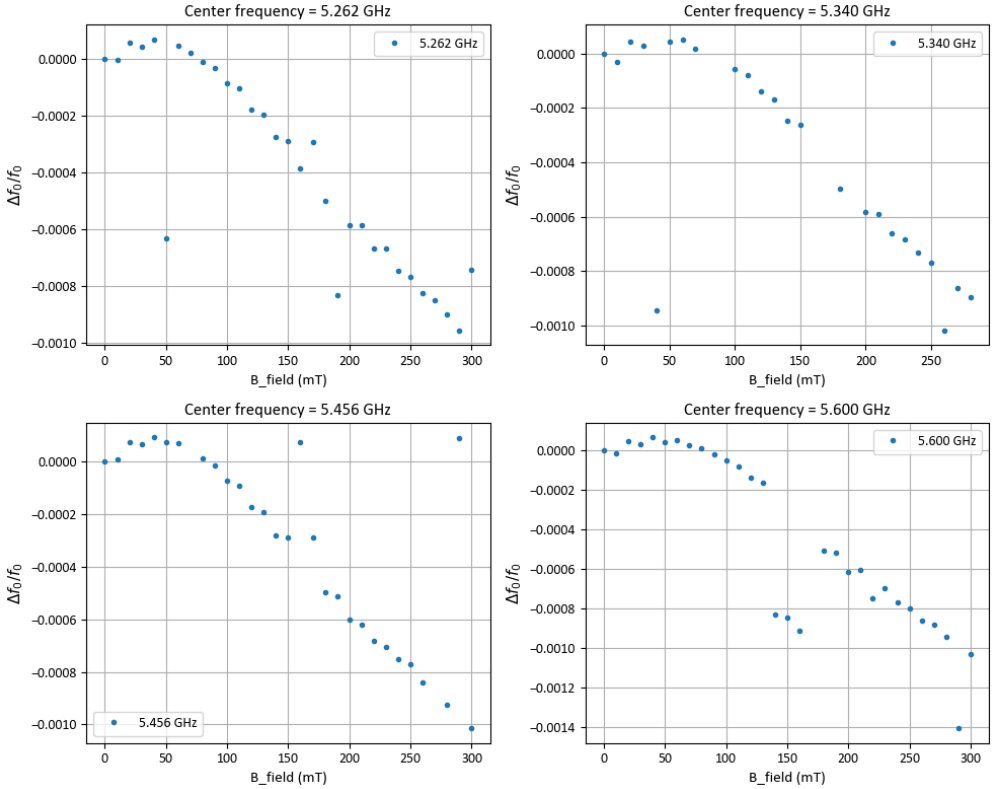

Figure 5.14: Resonance frequency shift of a Niobium resonator as a function of applied magnetic field.

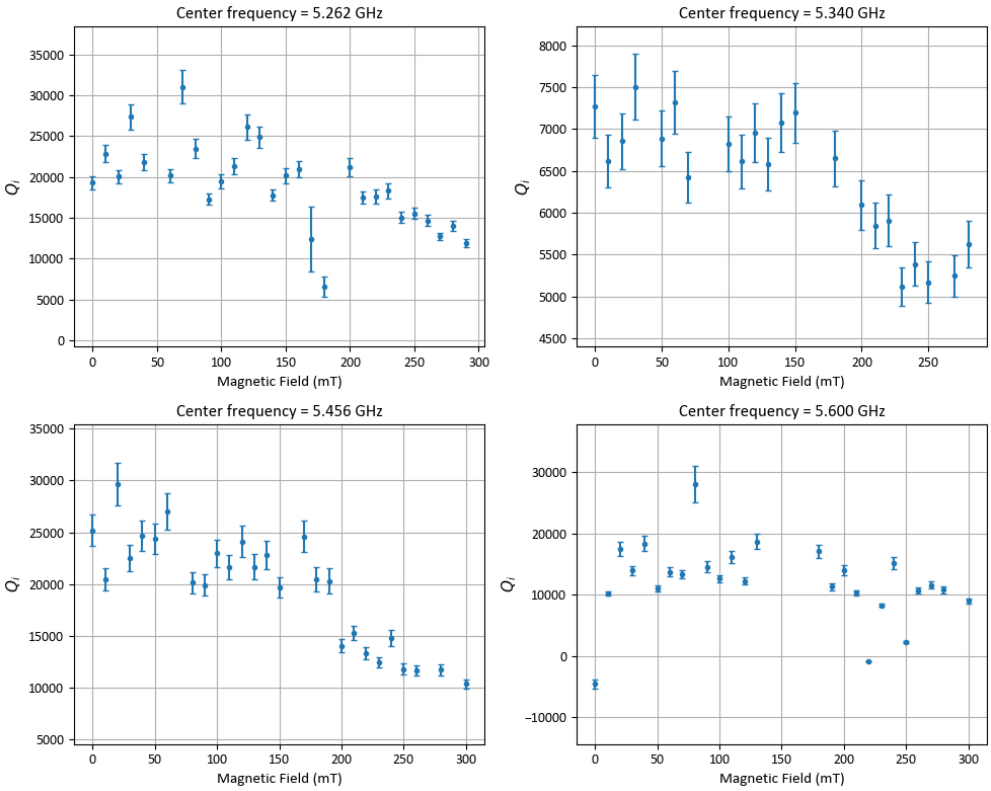

Figure 5.15: Quality factor of a Niobium resonator as a function of applied magnetic field.

What is peculiar is the increase in resonance frequency at low fields, which is not expected and should be investigated more in depth. In the meanwhile the quality factor defcreases almost linearly with the applied field, as expected.

Aluminum

Aluminum resonators show a more pronounced effect of the magnetic field, with a larger shift in resonance frequency and a more significant decrease in quality factor. This is due to the lower critical field of Aluminum, which makes it more susceptible to the effects of the magnetic field.

The resonance basically disappears at fields above $\approx 55\,\mathrm{mT}$, indicating that the superconducting properties of Aluminum are significantly affected by the magnetic field. In the meanwhile the material does not show to transitate to the normal state, as it remains conductive. Recovery time after removing the field is quite long, in the order of few minutes, indicating that some vortices might be trapped in the film.

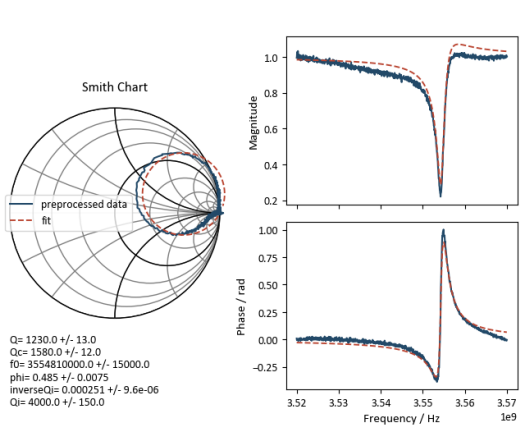

(a) Fit for a resonance at zero magnetic field.

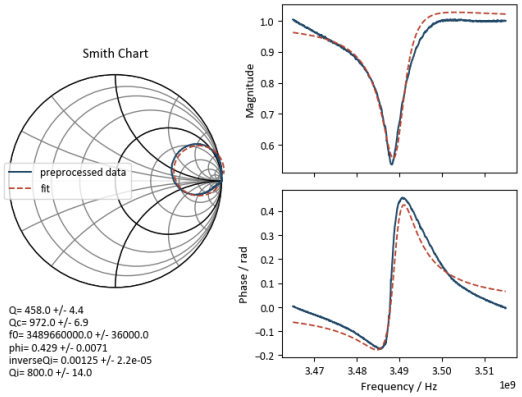

(b) Fit for a resonance at $\approx 50\,\mathrm{mT}$ magnetic field.

Figure 5.16: Overview of the magnetic field simulation performed with COMSOL Multiphysics to validate the shielding design.

Chapter 6

Conclusions and future work

In this chapter an emphasys is given to the description of the achievements of this thesis both from a scientific and technical perspective. The discussion, as well as the possible improvements, is divided in the three main section of this work.

6.1 Discussion

Design

A full design pipeline has been developed for lumped element resonators, with a fully automated cycle of input of geometrical parameters and output of resonance frequencies. This has been achieved using a python code to interface with Qiskit Metal for the laout design and using COMSOL APIs to automatically setup and run the simulation. By mixing this approach with analytical calculation of the inductive and capacitance parameters, and with impedance extraction by using the fit performed in Section 5.4.

Kinetic inductance simulations have been performed using the measures on the devices as a feedback. They are performed according to the kinetic inductance theory, describing the superconductor as a complex conductivity system, and by modeling this complex conductivity with the material parameters it is possible to simulate the behaviour of the circuits quite precisely, when the material is not very thick and not very high in kinetic inductance.

Fabrication

Fabrication techniques allowed a good definition of the designed geometrical patterns, as well as a satisfactory deposition of ultrathin Aluminum films. The standard growth rate of this metal as a superconductor, which is 0.5 nm/s, showed to generate

an electrically continuous film, allowing several types of applications.

A quite standard and low resources demanding fabrication recipe for these devices has been proposed and tested, and consists mainly on two lithographic steps. Reproducibility of this process can thus be easily assessed, in order to replicate the study or make use of the devices.

Measurements

Experiments at $T = 80\,\mathrm{mK}$ inside the dilution refrigerator showed a satisfactory working condition, both for the Al and Nb devices. Different behaviour of the same devices on the two materials have been found, and a possible explanation can be found in the kinetic inductance behavior, depending also on the thickness of the substrate.

An available setup for measurements in a static magnetic field has been: designed, simulated, fabricated and mounted on the dilution refrigerator. They showed satisfactory working conditions and compatibility for Niobium devices, while further tests are needed for the Aluminum resonators. These types of measurements showed some peculiar behaviors, which are valuable to be further investigated in future works.

6.2 Possible improvements and future work

Design

The main challenges of the design part are related to the kinetic inductance simulation. Improvements can be made by implementing a more accurate model for the complex conductivity of the superconductor, taking into account also the effects of thin films and disorder. The problem with thin Aluminum films mainly arises from the fact that the standard Mattis-Bardeen may not be able to describe the behavior of the superconductors when the thickness is reduced below a certain threshold, which is material dependent. The kinetic inductance value should be evalueated using the actual measurements performed on the films, and then used as an input for the simulation.

Fabrication

The fabrication recipe is quite standard, but some improvements can be made in order to increase the quality of the devices.

Most importantly, the deposition of the Aluminum film can be optimized to reduce the amount of disorder and impurities, which can affect the superconducting properties. Using more hours of pumping before the deposition, as well as a optimizing the growth rate, can help in this direction.

The geometrical definition of the patterns can be improved by using higher resolution lithography techniques, such as electron beam lithography, in order to reduce the edge roughness and increase the reproducibility of the devices. There is a slight mismatch between the designed and the fabricated geometries, which can be reduced by using more precise lithography methods, or optimization of the development and lift-off techniques implemented.

Measurements

The main improvement that can be made in the measurement part is to perform experiments in magnetic field, in order to study the behavior of the devices under these conditions. More data are required to fully understand the interaction between the magnetic field and the kinetic inductance of the resonators, mostly for Aluminum. Testing different orientations of the magnetic field with respect to the plane of the resonators can help in understanding the underlying physics and completely address the possibility of implementing quantum memories with ultrathin Aluminum.

Furthermore, a more detailed study of the temperature dependence of the resonance frequencies and quality factors can be performed, in order to better understand the superconducting properties of the materials used. This can help in optimizing the design and fabrication of the devices for specific applications. The influence of different substrates on the kinetic inductance and overall performance of the resonators can also be investigated in future work. Understanding the superconducting properties of ultrathin Aluminum can allow for the implementation of this material in more complex superconducting quantum devices that make use of the kinetic inductance properties.

To demonstrate that it is possible to use these resonators for a quantum memory application, experiments with spin donors implanted, inside a magnetic field should be performed, in order to show that the Zeeman splitting can be achieved and matched to the resonance frequencies.

Final devices

With the results in this thesis, it is possible to fabricate quantum memory devices based on lumped element resonators with high kinetic inductance. These devices

can be used to store quantum information for long times, and can be integrated with other superconducting quantum circuits. The next step would be to design and fabricate such quantum memory devices, and to test their performance in terms of coherence times and fidelity.

Moreover, the development of tunable resonators using kinetic inductance can be pursued, allowing for dynamic control of the resonance frequency and coupling to other quantum systems. The integration of these resonators with superconducting qubits can also be explored, in order to create hybrid quantum systems that can take advantage of the properties of both components.

List of Figures

Bibliography

[1] Michael A. Nielsen and Isaac L. Chuang. *Quantum Computation and Quantum Information: 10th Anniversary Edition*. Cambridge University Press, 2010 (cit. on pp. 2, 6).

[2] Khabat Heshami, Duncan G. England, Peter C. Humphreys, Philip J. Bustard, Victor M. Acosta, Joshua Nunn, and Benjamin J. Sussman. «Quantum memories: emerging applications and recent advances». In: *Journal of Modern Optics* 63.20 (Mar. 2016), pp. 2005–2028. ISSN: 1362-3044. DOI: 10.1080/09500340.2016.1148212. URL: http://dx.doi.org/10.1080/09500340.2016.1148212 (cit. on pp. 5, 8).

[3] Rohit Singh and Roshan M. Bodile. *A Quick Guide to Quantum Communication*. 2024. arXiv: 2402.15707 [eess.SP]. URL: https://arxiv.org/abs/2402.15707 (cit. on p. 6).

[4] Xiao-Min Hu, Yu Guo, Bi-Heng Liu, Chuan-Feng Li, and Guang-Can Guo. «Progress in quantum teleportation». In: *Nature Reviews Physics* 5.6 (2023), pp. 339–353 (cit. on p. 6).

[5] Lijun Ma, Xiao Tang, and Oliver Slattery. *Optical quantum memory and its applications in quantum communication systems*. en. 2020-01-16 2020. DOI: https://doi.org/10.6028/jres.125.002 (cit. on p. 7).

[6] Sergei Slussarenko and Geoff J Pryde. «Photonic quantum information processing: A concise review». In: *Applied physics reviews* 6.4 (2019) (cit. on p. 7).

[7] Koustubh Phalak, Avimita Chatterjee, and Swaroop Ghosh. *Quantum Random Access Memory For Dummies*. 2023. arXiv: 2305.01178 [quant-ph]. URL: https://arxiv.org/abs/2305.01178 (cit. on p. 8).

[8] Cécile Grèzes. *Towards a Spin-Ensemble Quantum Memory for Superconducting Qubits: Design and Implementation of the Write, Read and Reset Steps*. Springer Theses. Cham, Switzerland: Springer, 2016. ISBN: 978-3-319-37070-5. DOI: 10.1007/978-3-319-37070-5. URL: https://link.springer.com/book/10.1007/978-3-319-37070-5 (cit. on p. 9).

[9] V. Ranjan et al. «Multimode Storage of Quantum Microwave Fields in Electron Spins over 100 ms». In: *Phys. Rev. Lett.* 125 (21 Nov. 2020), p. 210505. DOI: 10.1103/PhysRevLett.125.210505. URL: https://link.aps.org/doi/10.1103/PhysRevLett.125.210505 (cit. on pp. 10, 17).

[10] He-Liang Huang, Dachao Wu, Daojin Fan, and Xiaobo Zhu. «Superconducting quantum computing: a review». In: *Science China Information Sciences* 63.8 (July 2020). ISSN: 1869-1919. DOI: 10.1007/s11432-020-2881-9. URL: http://dx.doi.org/10.1007/s11432-020-2881-9 (cit. on p. 10).

[11] Joel Howard et al. «Implementing two-qubit gates at the quantum speed limit». In: *Phys. Rev. Res.* 5 (4 Dec. 2023), p. 043194. DOI: 10.1103/PhysRevResearch.5.043194. URL: https://link.aps.org/doi/10.1103/PhysRevResearch.5.043194 (cit. on p. 11).

[12] Julian Huber, Ana Maria Rey, and Peter Rabl. «Realistic simulations of spin squeezing and cooperative coupling effects in large ensembles of interacting two-level systems». en. In: 105 (2022-01-24 05:01:00 2022). DOI: https://doi.org/10.1103/PhysRevA.105.013716. URL: https://tsapps.nist.gov/publication/get_pdf.cfm?pub_id=932524 (cit. on p. 11).

[13] M.W. Wu, J.H. Jiang, and M.Q. Weng. «Spin dynamics in semiconductors». In: *Physics Reports* 493.2 (2010), pp. 61–236. ISSN: 0370-1573. DOI: https://doi.org/10.1016/j.physrep.2010.04.002. URL: https://www.sciencedirect.com/science/article/pii/S0370157310000955 (cit. on p. 11).

[14] A. Tyryshkin, SA Lyon, AV Astashkin, and Arnold Raitsimring. «Electron Spin-Relaxation Times of Phosphorus Donors in Silicon». In: *Physical Review B* 68 (Mar. 2003). DOI: 10.1103/PhysRevB.68.193207 (cit. on p. 12).

[15] P. A. Mortemousque, S. Berger, T. Sekiguchi, C. Culan, R. G. Elliman, and K. M. Itoh. «Hyperfine clock transitions of bismuth donors in silicon detected by spin-dependent recombination». In: *Physical Review B* 89.15 (Apr. 2014). ISSN: 1550-235X. DOI: 10.1103/physrevb.89.155202. URL: http://dx.doi.org/10.1103/PhysRevB.89.155202 (cit. on p. 12).

[16] Alexandre Blais, Ren-Shou Huang, Andreas Wallraff, S. M. Girvin, and R. J. Schoelkopf. «Cavity quantum electrodynamics for superconducting electrical circuits: An architecture for quantum computation». In: *Phys. Rev. A* 69 (6 June 2004), p. 062320. DOI: 10.1103/PhysRevA.69.062320. URL: https://link.aps.org/doi/10.1103/PhysRevA.69.062320 (cit. on p. 13).

[17] COMSOL RF Module. *CPW Resonator for Circuit Quantum Electrodynamics*. URL: https://doc.comsol.com/6.1/doc/com.comsol.help.models.rf.cpw_resonator/cpw_resonator.html (cit. on p. 14).

[18] M. Göppl et al. «Coplanar waveguide resonators for circuit quantum electrodynamics». In: *Journal of Applied Physics* 104.11 (Dec. 2008), p. 113904. ISSN: 0021-8979. DOI: 10.1063/1.3010859. eprint: https://pubs.aip.org/aip/jap/article-pdf/doi/10.1063/1.3010859/14109820/113904_1_online.pdf. URL: https://doi.org/10.1063/1.3010859 (cit. on p. 14).

[19] Zuyeon Kim et al. «Thin-film superconducting resonator tunable to the ground-state hyperfine splitting of ^{87}Rb». In: *AIP Advances* 1 (Oct. 2011). DOI: 10.1063/1.3651466 (cit. on p. 15).

[20] B. Ferdinand, D. Bothner, R. Kleiner, and D. Koelle. «Tunable Superconducting Two-Chip Lumped-Element Resonator». In: *Physical Review Applied* 11.3 (Mar. 2019). ISSN: 2331-7019. DOI: 10.1103/physrevapplied.11.034050. URL: http://dx.doi.org/10.1103/PhysRevApplied.11.034050 (cit. on p. 16).

[21] C. Eichler, A. J. Sigillito, S. A. Lyon, and J. R. Petta. «Electron Spin Resonance at the Level of 10^4 Spins Using Low Impedance Superconducting Resonators». In: *Phys. Rev. Lett.* 118 (3 Jan. 2017), p. 037701. DOI: 10.1103/PhysRevLett.118.037701. URL: https://link.aps.org/doi/10.1103/PhysRevLett.118.037701 (cit. on pp. 16, 17, 21, 26, 96).

[22] T. Chang, I. Holzman, S. Q. Lim, D. Holmes, B. C. Johnson, D. N. Jamieson, and M. Stern. *Strong coupling of a superconducting flux qubit to single bismuth donors*. 2024. arXiv: 2411.02852 [cond-mat.mes-hall]. URL: https://arxiv.org/abs/2411.02852 (cit. on p. 18).

[23] NR Butler, P Fisher, and AK Ramdas. «Excitation spectrum of bismuth donors in silicon». In: *Physical Review B* 12.8 (1975), p. 3200 (cit. on p. 22).

[24] Luca Callegaro. *Electrical impedance: principles, measurement, and applications*. CRC Press, 2012 (cit. on p. 22).

[25] John Bardeen. «Critical fields and currents in superconductors». In: *Reviews of modern physics* 34.4 (1962), p. 667 (cit. on p. 23).

[26] K. Borisov et al. «Superconducting granular aluminum resonators resilient to magnetic fields up to 1 Tesla». In: *Applied Physics Letters* 117.12 (Sept. 2020). ISSN: 1077-3118. DOI: 10.1063/5.0018012. URL: http://dx.doi.org/10.1063/5.0018012 (cit. on p. 24).

[27] J. Krause, C. Dickel, E. Vaal, M. Vielmetter, J. Feng, R. Bounds, G. Catelani, J. M. Fink, and Yoichi Ando. «Magnetic Field Resilience of Three-Dimensional Transmons with Thin-Film Al/AlO_x/Al Josephson Junctions Approaching 1 T». In: *Phys. Rev. Appl.* 17 (3 Mar. 2022), p. 034032. DOI: 10.1103/PhysRevApplied.17.034032. URL: https://link.aps.org/doi/10.1103/PhysRevApplied.17.034032 (cit. on p. 24).

[28] Francesco Grilli, Svetlomir Stavrev, Yann Le Floch, Marta Costa-Bouzo, Emmanuel Vinot, Iszabela Klutsch, Gérard Meunier, Pascal Tixador, and Bertrand Dutoit. «Finite-element method modeling of superconductors: From 2-D to 3-D». In: *IEEE Transactions on Applied Superconductivity* 15.1 (2005), pp. 17–25 (cit. on p. 26).

[29] L. McKenzie-Sell, J. Xie, C.-M. Lee, J. W. A. Robinson, C. Ciccarelli, and J. A. Haigh. «Low-impedance superconducting microwave resonators for strong coupling to small magnetic mode volumes». In: *Phys. Rev. B* 99 (14 Apr. 2019), p. 140414. DOI: 10.1103/PhysRevB.99.140414. URL: https://link.aps.org/doi/10.1103/PhysRevB.99.140414 (cit. on pp. 27, 29).

[30] Rui Igreja and C.J. Dias. «Analytical evaluation of the interdigital electrodes capacitance for a multi-layered structure». In: *Sensors and Actuators A: Physical* 112.2 (2004), pp. 291–301. ISSN: 0924-4247. DOI: https://doi.org/10.1016/j.sna.2004.01.040. URL: https://www.sciencedirect.com/science/article/pii/S0924424704000779 (cit. on p. 28).

[31] Zlatko K Minev et al. *Qiskit Metal: An Open-Source Framework for Quantum Device Design & Analysis*. 2021. DOI: 10.5281/zenodo.4618153. URL: https://doi.org/10.5281/zenodo.4618153 (cit. on p. 29).

[32] SQDLab University of Queensland. *SQD Metal: Tools to aid in simulating and fabricating superconducting quantum devices.* 2023. URL: https://github.com/sqdlab/SQDMetal (cit. on p. 32).

[33] Daniel C Mattis and John Bardeen. «Theory of the anomalous skin effect in normal and superconducting metals». In: *Physical Review* 111.2 (1958), p. 412 (cit. on p. 37).

[34] Jonas Zmuidzinas. «Superconducting Microresonators: Physics and Applications». In: *Annual Review of Condensed Matter Physics* 3.Volume 3, 2012 (2012), pp. 169–214. ISSN: 1947-5462. DOI: https://doi.org/10.1146/annurev-conmatphys-020911-125022. URL: https://www.annualreviews.org/content/journals/10.1146/annurev-conmatphys-020911-125022 (cit. on p. 37).

[35] Adolfo Canuto Reyes, Samir M El-Ghazaly, Steve Dorn, Michael Dydyk, and Dieter K Schroder. «Silicon as a microwave substrate». In: *1994 IEEE MTT-S International Microwave Symposium Digest (Cat. No. 94CH3389-4)*. IEEE. 1994, pp. 1759–1762 (cit. on p. 57).

[36] J. Buechler, E. Kasper, P. Russer, and K.M. Strohm. «Silicon High-Resistivity-Substrate Millimeter-Wave Technology». In: *IEEE Transactions on Microwave Theory and Techniques* 34.12 (1986), pp. 1516–1521. DOI: 10.1109/TMTT.1986.1133572 (cit. on p. 57).

[37] V Dyakonov and G Denninger. «Overhauser-shift measurements on Si: P near the metal-insulator transition». In: *Physical Review B* 46.8 (1992), p. 5008 (cit. on p. 57).

[38] Nobuteru Tsubouchi Nobuteru Tsubouchi, Akiyoshi Chayahara Akiyoshi Chayahara, Yoshiaki Mokuno Yoshiaki Mokuno, Atsushi Kinomura Atsushi Kinomura, and Yuji Horino Yuji Horino. «Epitaxial Growth of Pure 28Si Thin Films Using Isotopically Purified Ion Beams». In: *Japanese Journal of Applied Physics* 40.12A (2001), p. L1283 (cit. on p. 57).

[39] Naoki Kikugawa. «Recent Progress of Floating-Zone Techniques for Bulk Single-Crystal Growth». In: *Crystals* 14.6 (2024), p. 552 (cit. on p. 58).

[40] Georgia Tech Henderson group. «Introduction to microlithography». In: (), pp. 24, 27, 32. URL: https://henderson.chbe.gatech.edu/Introductions/microlithography%20intro.html (cit. on p. 58).

[41] SA Ekhorutomwen and Samuel P Sawan. «Critical review on photoresists». In: *Polymers in Optics: Physics, Chemistry, and Applications: A Critical Review* 10285 (1996), pp. 212–236 (cit. on p. 58).

[42] Katsumi Yamaguchi and Takeshi Nakamoto. «Micro fabrication by UV laser photopolymerization». In: *Nagoya University, School of Engineering, Memoirs* 50.1 (1998), pp. 33–82 (cit. on p. 59).

[43] MicroChemical. *AZ Resists datasheet. Technical Datasheet.* 2025 (cit. on p. 59).

[44] ME Reuhman-Huisken and FA Vollenbroek. «An optimized image reversal process for half-micron lithography». In: *Microelectronic engineering* 11.1-4 (1990), pp. 575–580 (cit. on p. 59).

[45] A. Reiser, J.P. Huang, X. He, T.F. Yeh, S. Jha, H.Y. Shih, M.S. Kim, Y.K. Han, and K. Yan. «The molecular mechanism of novolak-diazonaphthoquinone resists». In: *European Polymer Journal* 38.4 (2002), pp. 619–629. ISSN: 0014-3057. URL: https://www.sciencedirect.com/science/article/pii/S0014305701002300 (cit. on p. 59).

[46] CK O'sullivan and GG Guilbault. «Commercial quartz crystal microbalances–theory and applications». In: *Biosensors and bioelectronics* 14.8-9 (1999), pp. 663–670 (cit. on p. 64).

[47] Peter Eaton and Paul West. *Atomic force microscopy*. Oxford university press, 2010 (cit. on p. 73).

[48] D. C. Mattis and J. Bardeen. «Theory of the Anomalous Skin Effect in Normal and Superconducting Metals». In: *Phys. Rev.* 111 (2 July 1958), pp. 412–417. DOI: 10.1103/PhysRev.111.412. URL: https://link.aps.org/doi/10.1103/PhysRev.111.412 (cit. on p. 92).

[49] Barends Rami. «Photon-detecting superconducting resonators». PhD thesis. Delft University of Technology, Delft, NL, 2009. URL: https://resolver.tudelft.nl/uuid:e32a9526-fa31-4639-ad98-7493e26063f9 (cit. on p. 93).

[50] Jiansong Gao. «The physics of superconducting microwave resonators». In: 2008. URL: https://api.semanticscholar.org/CorpusID:108743487 (cit. on p. 93).

[51] Ashish Alexander. «Measuring and Trapping Quasiparticles in Superconducting Coplanar Waveguide Resonators». PhD thesis. University of Maryland, College Park, 2021 (cit. on p. 93).

[52] Paniz Foshat et al. *Quasiparticle Dynamics in NbN Superconducting Microwave Resonators at Single Photon Regime*. 2025. arXiv: 2506.17816 [quant-ph]. URL: https://arxiv.org/abs/2506.17816 (cit. on p. 93).

[53] «Materials loss measurements using superconducting microwave resonators». In: *Review of Scientific Instruments* 91.9 (2020) (cit. on p. 101).

Acknowledgements

Contributors of this work are from different institutions:

- **Politecnico di Torino:** Prof. Matteo Cocuzza
- **INRiM:** Dr. Emanuele Enrico, Dr. Luca Fasolo, Dr. Martina Marzano. PhD students: Alessandro Alocco, Andrea Celotto, Bernardo Galvano, Emanuele Palumbo. Technicians Vincenzo Butera and Danilo Serazio.
- **University of Torino:** Prof. Marco Fanciulli
- **CNR:** Dr. Carmine Granata

MC for academical supervision and guidance on writing the thesis. EE, LF and MF for the idea behind the project. LF, VB and CG for fabrication of the devices. EE, LF, AA, AC, BG and EP for the help in setting up the experiments and performing the measurements. EE, LF, MM and DS for the development and fabrication of the magnetic field setup. EE, LF, AA, BG, EP, VB and MF for discussions about several aspects of the project. EE and MF for providing funding.

***

Un ringraziamento speciale va a una serie incredibile di persone che mi ha accompagnato in tutto questo. In questa tesi, a cui tengo particolarmente, e in tutta la mia avventura universitaria c'è il culmine di un percorso veramente collettivo. Provo a listarli tutti qui.

A Mamma e Papà che non hanno mai messo in dubbio nulla, di qualsiasi scelta io abbia fatto. Una fiducia incondizionata e tantissimi sacrifici che cominciano quasi un quarto di secolo fa.

A Matti e Lollo che hanno fatto la mia stessa scelta universitaria, arriverete dove volete, lo so. Vi voglio bene.

Alla grandissima famiglia famigliosa: Nonni, Zii e Cugini. Siamo tanti e ognuno speciale a modo suo. Siete il motivo per cui so di avere un posto che chiamo casa.

A Zio Antonello, Nonno Angiolino e Nonna Natalina. Siete una parte di me che custodisco sempre nel cuore.

Al gruppo dei Lanciani allargato. Sopportarmi per 5 anni è oggettivamente un'impresa, l'avete fatto nella maniera più sana e divertente possibile. Questa città non sarebbe stata così tanto speciale senza di voi.

Al gruppo degli Alpolizzati. Siamo sempre stati tanti e diversi, le strade in alcuni casi si sono separate, ed è normalissimo. Ma so che tutti prima o poi ripenserete a dove eravate quando abbiamo vinto gli europei, alle cene del Secret Santa, alle lauree e soprattutto Al Gioco...

Agli amici di Quantum. Affrontare come pionieri questo percorso poteva essere difficile. E lo è stato. Ma ci ha reso anche più uniti, e ci ha fatto diventare veri amici con una passione in comune, alla quale stiamo dedicando tanto.

Agli amici del liceo. Mi avete insegnato che non esistono gli addii. Perchè ci si ritrova sempre, in un modo o nell'altro. Basta volerlo.

Agli amici di ASP. Che tutto sommato è stata una festa, nonostante qualche piccolo spauracchio. Voi l'avete resa molto divertente. Ci incontreremo per il mondo, a fare cose incredibili.

Clara, vederti mi scalda il cuore, sempre, è come se ti conoscessi fin da piccolo. Sono fiero di te, dei tuoi traguardi e della persona fantastica che hai sempre dimostrato di essere.

Alessia, ci siamo confidati gioie e dolori, e continueremo a farlo. Sei un'ispirazione, mi hai insegnato tantissimo, e ha un valore incommensurabile.

Luca, il coinquilino migliore che si possa desiderare. Sicuramente è stato difficile sopportarmi in casa, grazie per non avermi mai fatto sentire in difetto.

Sabia, sei la più matta di tutti, e sai che è un complimento. Tutte le avventure vissute insieme e le tante altre che verranno sono un dono, che sono felice di condividere con te.

Pietro e Giuss, dopo 13 anni di amicizia(semicit.), sarebbe sbagliato separarvi. Voi sapete tutto di me, e non è facile. Questo la dice lunga su quanto siamo legati. Vi amo.

Federica, che condivide con me questa festa. Sono sinceramente felice per te tanto quanto lo sono per me. C'è tanto di tuo in tutto questo.

Antonio, compagno di serate riflessive alla ricerca delle giuste domande. La possibilità di aprirmi che ho con te non ha eguali. Grazie.

A questa città, con la speranza che sia un arrivederci.

E a quella manica di fisici, che 100 anni fa, quasi per gioco, si inventarono i quanti.